Using high-resolution climate models to predict increases in atmospheric turbulence

Author:

Isabel H. Smith

Supervisor:

Prof. Paul Williams

Prof. Reinhard Schiemann

A thesis submitted in fulfillment of the requirements for the degree of Doctor of Philosophy

January, 2025

Declaration of Authorship

I, Isabel H. Smith, declare that this thesis titled, “Using high-resolution climate models to predict increases in atmospheric turbulence” and the work presented in it are my own. I confirm that:

- This work was done wholly or mainly while in candidature for a research degree at this University.
- Where I have quoted from the work of others, the source is always given. With the exception of such quotations, this thesis is entirely my own work.
- Where the thesis is based on work done by myself jointly with others, I have made clear exactly what was done by others and what I have contributed myself.

Signed:

Abstract

Clear Air Turbulence (CAT) and Mountain Wave Turbulence (MWT) are two types of upper-level atmospheric turbulence that have a dangerous impact on aircraft. Understanding how these types of turbulence are changing with global tropospheric warming is important for the future of the aviation sector. Using high resolution global climate models, this thesis initially focuses on how moderate CAT could vary in a high-end warming scenario over the transatlantic basin. Across simulated projected data from the year 1950 to 2050, moderate CAT on average increased in frequency by +14%, +9%, +9%, and +14% over Northern Hemisphere autumn, winter, spring and summer per degree of global near-surface warming.

Furthermore, the increase in CAT frequency is decomposed into patch size and number. The region of interest was expanded to the mid to high latitudes over the Northern and Southern Hemispheres. For winter, both hemispheres experienced an increase in the average area and number of patches. This combined effect led to large increase in moderate winter-time CAT, with the total area increasing on average by +360 km^2 and +474 km^2 per year, for the Northern and Southern Hemispheres respectively.

Projected trends in global MWT were the final area of research discussed. A projected increase in moderate or greater MWT was found to develop over Greenland, the Antarctic and regions in Asia. However, a decrease was found over the Alps, Atlas and northern and central Andes. A link between MWT trends and projected median surface wind was found and explained several reductions in MWT. A decrease in MWT developed over the Rocky Mountain range in all seasons except Northern Hemisphere winter with an increase of +60.6%.

This thesis projects future variations in CAT and MWT, with implications for a more turbulent future for the aviation sector.

Acknowledgements

Firstly, I would to thank my two great supervisors, Paul Williams and Reinhard Schiemann, for their support and encouragement over the last four years. I really appreciate all the time, ideas and insight they both gave and the exciting, friendly environment that lead to such a great PhD experience. I would also like to thank Tom Frame and Christopher Merchant for reviewing and aiding my work with every monitoring committee meeting. I am very grateful for their great feedback and encouragement which helped move me forward in the PhD.

I would like to thank my lovely family for being a fantastic support network. My wonderful parents have always supported and encouraged me. I would not be where I am today without them. I would like to thank my kind and wonderful brothers for both offering to read this thesis, but neither doing so. I would also like to thank my sister for sending daily videos of my two adorable nieces.

The Meteorology Department has also become my second family, and I would

like to thank everyone for the great memories and constant support. In particular, the fun and chaotic PhD community, with special thanks to my Cohort; Hannah, Brian, Charlie, Harriet, Natalie, Alanna, Helen and Blair. A particularly break free moment in the PhD was when a number of us in the cohort organised, acted and filmed the Meteorology Christmas Pantomime. A big thank you to Brian and Hannah for encouraging me to join Met runners and giving me a great PhD outlet.

I would also like to thank my great office mates from the 5th floor Lyle and Meteorology building (2U08); Sophie, Lauren, Devon, Jake, Akshay, Meg, Beth, Harriet, Flynn, Karine, Ieuan, Rhiannon, Niamh and Nathan. A particular thank you to Meg, Lauren, Sophie, Beth and Harriet for being very distracting, but also being there for me with constant coffee breaks.

Lastly, I am very grateful for the kindness and support I have from a number of friends outside of this department, who encourage me daily. I am very lucky to have you; Hannah, Eleanor, Rebecca S, Caroline, Melba, Catherine, Marina, Rebecca C. and Emily.

Declaration of Papers

This thesis is written and submitted through a collection of manuscripts. The first chapter of results is an unchanged published paper referenced below. The remaining two result chapters have been written as papers, with the purpose of submitting for review imminent.

- Smith I.H, Williams P.D., Schiemann R., 2023; **Clear-air turbulence trends over the North Atlantic in high-resolution climate models**. *Climate Dynamics*. Available at: https://doi.org/10.1007/s00382-023-06694-x
- Smith I.H, Williams P.D., Schiemann R., 2025; **Evaluation of clear air turbulence patches in high-resolution global climate models**.
- Smith I.H, Williams P.D., Schiemann R., 2025; **Global change in mountain wave turbulence within high resolution climate models**.

The contributions from the PhD Candidate, Isabel H. Smith (IHS) and Supervisors, Paul D. Williams (PDW) and Reinhard Schiemann (RS), are given below for all manuscripts.

IHS: Conceptualization, formal analysis, investigation, project administration, software, visualization, writing original draft, writing—review and editing.

PDW: Conceptualization, funding acquisition, methodology, project administration, supervision, writing review and editing.

RS: Conceptualization, funding acquisition, methodology, project administration, supervision, writing review and editing.

"With very best wishes for a great career!"

- Robert Sharman

Contents

List of Figures

List of Tables

Chapter 1

Introduction and literature review

1.1 Atmospheric turbulence

Characterising turbulence is one of literature's chief outstanding difficulties (Lamb, 1945). Its nature is non-linear, multi-dimensional, chaotic and occurs in both the atmosphere, from boundary layer to stratosphere, and oceans. Understanding the mechanisms that generate atmospheric turbulence is of key importance for many areas of research and forecasting, with its inclusion in numerical weather predictions (NWP) and global circulation models (Wolff and Sharman, 2008). Upper-level atmospheric turbulence is also a critical mechanism for the global energy budget, as it vertically mixes gases such as ozone and water vapour, across the tropopause into the free atmosphere (Qin et al., 2022). Ozone and water vapour have an important role within the thermal structure of the atmosphere (greenhouse gases), with strong radiative impacts within the troposphere (Ramaswamy et al.,2001). Upper-level atmospheric turbulence is a fundamental phenomenon critical for the mixing of gases, but is also extremely dangerous if encountered by aircraft, which typically cruise at or around the tropopause. At these heights, passengers are more likely to have seat belts unbuckled (Kim et al, 2018), leading to incidences of passengers and crew members vigorously thrown around the aircraft, depending on the severity of the encounter.

The United States of America's (USA) Federal Aviation Administration (FAA) tracks reports of serious turbulence injuries. Over USA airspace, between 2009 and 2022, 163 reports of such serious injuries were documented. The FAA classify a serious injury as an individual hospitalised for 48 hours or more (FAA, 2024). Individually, the likelihood of encountering severe turbulence is very small, considering that the FAA recorded 917 million passengers travelling in the year 2022 alone (FAA; Air Traffic by numbers, 2023). However, encountering light turbulence is common, with atmospheric turbulence linked with 71% of all weather-related in-flight injuries (Eick, 2014). The remaining 29% within such injuries are linked to other dangerous meteorological phenomena such as icing impacting lift, adverse winds, freezing rain/sleet, heavy precipitation and fog (Eick, 2014) . The USA's aviation sector is estimated to spend 200 million US dollars annually related to injuries and damages, with turbulence impacting both the interior and exterior of the aircraft (Williams et al., 2014). Tens of millions of this cost is linked to medical and insurance claims from passengers and crew (Golding, 2002). Increased workload on air traffic control staff is also a cost for the aviation sector, with pilots seeking diverted flight paths to avoid turbulence. These routes are often longer, convoluted, and burn more fuel. In 2017, the aviation industry contributed 859 million tonnes of the man-made CO_2 (Atrill et al., 2021), this is an increase of 47% from the global aviation sector compared to records before the year 2000 (EASA, 2022).

The severity of a turbulent event depends on the size of the aircraft, with atmospheric eddies ranging in sizes, but impacting aviation at 1km to 100m, or even smaller for non-commercial airlines (Storer et al., 2017, Sharman and Pearson , 2017, Ellrod et al., 2015). An eddy is a movement of air flow, often rotating, that deviates from the general atmospheric background flow. The impact of turbulent eddies on an aircraft is quantitatively defined by the cube root of the energy (eddy) dissipation rate (EDR) (MacCready, 1964). Physically EDR represents the cubed root of the rate of change from kinetic energy to heat by the smallest eddies (Sharman and Lane, 2016). $EDR^{1/3}$ has a proportional relationship to the root mean square vertical acceleration of an aircraft (Sharman and Lane, 2016).

EDR$^{1/3}$'s impact on passengers and crew are dependent on integral factors including aircraft type, altitude, weight, and airspeed (Kim et al, 2018; Sharman and Lane, 2016). For example, EDR$^{1/3}$ values of 0.1-0.2 m$^{2/3}s^{-1}$, on a medium category transport plane, are known to be associated with a slight erratic change in altitude for the aircraft and somewhat rhythmic bumpiness. This would be considered a light turbulence encounter (Sharman and Lane, 2016). Moderate encounters are more intense, with greater shifts in altitude and rapid jolts, but control over the aircraft is maintained by the crew. A loss in control, normally for a very short period, is linked to severe turbulence. On a medium sized aircraft, severe and extreme turbulence, which are interchangeable in some texts, are linked to EDR$^{1/3}$ values greater than 0.5 $^{2/3}s^{-1}$ (Williams and Joshi, 2013). As discussed, these encounters are very rare, with assumptions made that less than 0.1% of the atmosphere contains severe turbulence. Aircraft encountering patches of turbulence often move upwards in height to remove themselves from these zones. This shift in altitude comes from a patch of turbulence typically horizontally wide but vertically thin. Over a 10-year climatology, Sharman et al. (2014) determined that a patch of turbulence on average was 60-70km wide and 1km in thickness. In this paper, a turbulence patch is defined as a series of EDR$^{1/3}$ values greater than 0.1 m$^{2/3}s^{-1}$, that lasts at minimum for 5 minutes, with at least one EDR$^{1/3}$ peak of 0.2 m$^{2/3}s^{-1}$.

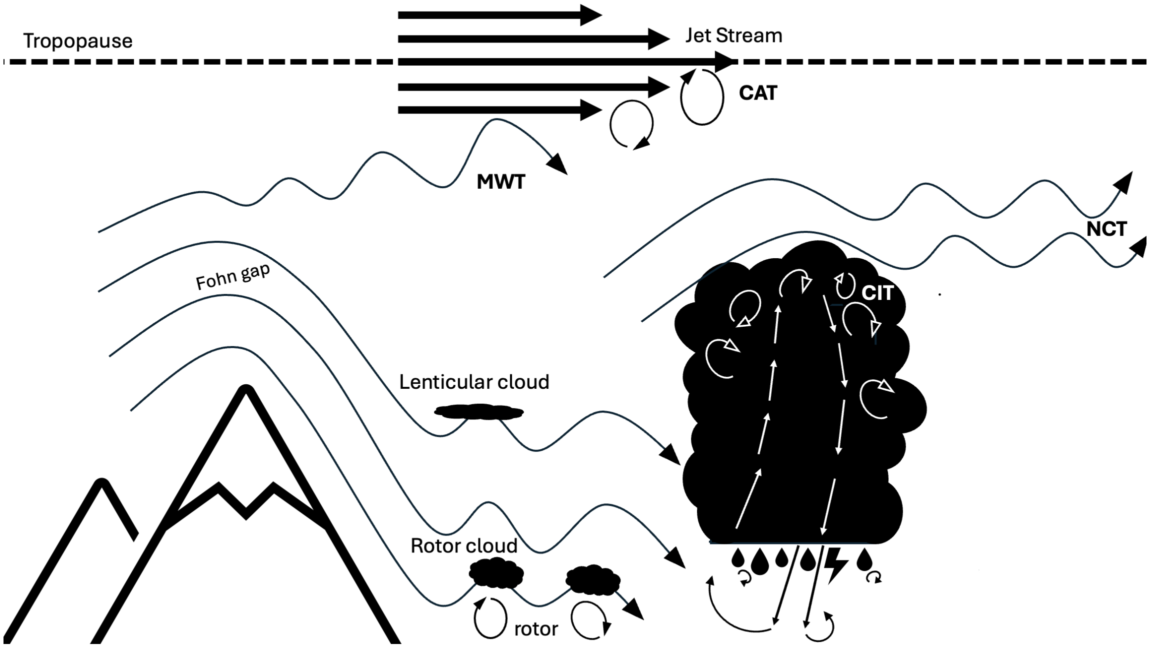

FIGURE 1.1: A schematic displaying the mechanisms that develop the four main types of upper-level atmospheric turbulence that impact aviation; clear air (CAT), convectively induced (CIT), mountain wave (MWT) and near cloud (NCT) turbulence (Adapated from Marlton,(2016), Kim et al. (2018) and Kuettner and Jenkins (1953))

One useful way of breaking down aviation-scale turbulence in literature is to categorise an event by its formation, or environment in which it developed. For example, clear air turbulence (CAT; Section 1.2), occurs within a stratified, convectively cloud free ("clear air") environment. If turbulence was linked to an active vertically deep convective system, it would be referenced to as convectively induced turbulence (CIT; Section 1.4) or perhaps near cloud turbulence (NCT; Section 1.4) depending on the distance from the active zone. Fig. 1.1 portrays a simplified diagram of this categorisation, with different mechanism leading to the formation of CAT, CIT, NCT and finally mountain wave turbulence (MWT; Section 1.3). Through this categorisation, turbulent events can be broken down by severity and formation. This leads to an effective and beneficial way for pilots to report on such an encounter and for forecasting or research purposes. A pilot report of turbulence is referred to as a PIREP.

1.2 Clear air turbulence

The American National Committee on Clear Air Turbulence defines CAT as "turbulence in the free atmosphere of interest in aerospace operations that is not in, or adjacent to visible convective activity. This includes turbulence found in cirrus clouds not in or adjacent to visible convective activity " (Pao and Goldburg, 1969). This definition allows room for interpretation for the mechanisms that generate CAT, with MWT and NCT often included with the CAT category. Fig. 1.1 highlights this, with breaking waves induced by the large convective feature on the right of the figure leading to NCT and the breaking mountain (lee) waves forming MWT on the left, both developing within "clear air". Therefore, MWT and NCT can reside in the overarching definition of CAT. However, within this thesis, when discussing CAT, it is purely focused on turbulence generated by jet streams and streaks (top of fig. 1.1). Ellrod et al. (2015), through the use of satellite imagery and PIREPs, discusses that cirrus clouds can be used as an indication of CAT. Cirrus clouds consist of ice crystals and reside at high altitudes within the troposphere between 3 to 18km from the surface depending on global location (WMO, 2024). Aircraft, and large ship, can even form their own cirrus clouds in the upper atmosphere refereed to as contrails.

Mid-latitude jet streams are bands of fast flowing winds that propagate globally eastward in the northern hemisphere (NH) and westward in the southern hemisphere (SH). CAT generation is linked to jet streams due to increased shear-driven instabilities such as Kelvin-Helmholtz Instability (KHI) on the edges and sides of the jet cores, with maximas in CAT found above and below these regions (Wolff and Sharamn, 2008). KHI, which is the instability induced by shear in a stratified flow, is on occasion visible in a moist atmosphere, with air parcels lifted to their condensation levels generating billow clouds (Sharman and Lane, 2016). The jet stream max in zonal wind speed is often located just below the tropopause (Halton and Hakim,2013), a location where CAT has been found to occur most frequently (Wolff and Sharman, 2008). Jet streams, and their associated upper-level frontal systems, lead to locally enhanced areas of shear and increased KHI. The subtropical and mid-latitude jet streams develop through different mechanisms. The angular momentum transport from the Hadley cell circulations develop a weak subtropical jet at latitudes of 30-40 °N/S. However, the mid-latitude polar jet stream is driven by large scale transient eddies, and meridional temperature gradient (MTG) (Madonna et al., 2017). It owes its existence to the thermal wind balance and equator to pole temperature contrast. Its westerly (easterly) propagation in the NH (SH) develops through the difference in tropospheric heights between the poles and tropics, and the Coriolis effect deflecting the movement of air, leading to the jet stream encompassing the globe. The polar-driven mid-latitude jet streams have a strong seasonal dependence with winters linked to a maximum in wind speed, shear and CAT. The winter zonal mean wind speeds in the NH are double that of their relative summers, assuming wind and temperature profiles followed thermal wind balance to a high accuracy. The NH summer jet's relative speed decreases due to a weaker MTG (Wolff and Sharman, 2008). The seasonality of the jet between winter to summer in the NH is greater than the seasonal shift in the SH. Due to greater fractional area of the SH covered by oceans, and the thermal inertia of oceans (Holton and Hakim, 2012), the north-south temperature gradients do not vary as much in SH summer and winter.

1.2.1 Climate change; impact on clear air turbulence

The anthropogenic increase in troposheric carbon dioxide (CO_2) has had a damaging and fatal impact on our planet with sea level rise and the increase in the severity and length of dangerous weather phenomena such as heatwaves and floods already impacting people on a global scale (IPCC, 2023). Considering the large impact of atmospheric turbulence on the aviation sector, a key area of research developed to understand how CAT could change due to global troposheric warming.

The North Atlantic basin is one of the busiest and most congested flight regions in the world (Kim et al., 2018). The National Air Traffic Services (2023) define it as the busiest oceanic aerospace, with on average 1,700 flights travelling through the area a day. In this region, Lee et al. (2019) suggests that anthropogenic warming has enhanced winter-time polar jet shear in recent years, due to a steepening in the horizontal temperature gradient (HTG) between the troposphere and stratosphere. Lee et al. (2019), using pressure-level zonal winds and temperature values from ECMWF (European Centre for Medium-Range Weather Forecasts) ERA-interims datasets, found a significant increase by +11-17% in vertical wind shear between 1979 (beginning of satellite sourced data) and 2017. The increase is hypothesized to correlate to the steepening in HTG, with the stratosphere cooling at a similar rate to global tropospheric warming. The MTG between the poles and tropics has also impacted the eddy driven jet across the globe (Lee et al., 2023), with the change in MTG shown evidently in fig. 1.2. Williams (2016) suggested in a future atmospheric scenario, with double the concentration of tropospheric

CO_2, cruising aircraft would spend an extra 2,000 h per year in the air, assuming no growth in the industry, due to a stronger upper-level eddy-driven jet stream. This equates to 7.2 million gallons of jet fuel and 70 million kgs of CO_2

The aforementioned increase in wind speed and shear within the eddy driven polar jet stream over the North Atlantic Ocean was first hypothesised to impact CAT formation in Williams and Joshi (2013). This paper, using a coupled atmosphere-ocean global climate model (GCM), focused on a future atmospheric scenario with CO_2 concentration double that of a pre-industrial atmosphere. This model applied was version 2.1 of the Geophysical Fluid Dynamics Laboratory (GFDL) model referenced as GFDL-CM2.1. It was developed within the Coupled Model Intercomparison Project (CMIP) 3rd phase. The World Climate Research Programme (WCRP) developed CMIP to evaluate and improve GCMs and to understand future and past climate variability (Bock et al. 2020). CMIP started with a purpose to evaluate the historical and future changes to our climate occurring from natural or anthropogenic forcing. Since its starting point with only a small number of GCMs, it has been updated with six phases and grown into a large worldwide multi-model research project (Eyring et al., 2016).

Williams and Joshi (2013), using GFDL-CM2.1 (grid spacing latitude; 2.0°, longitude; 2.5°), quantified a projected increase in the median strength of North Atlantic CAT by +10-40% and an overall projected rise by +40-170% in Moderate or Greater (MOG) CAT due to a doubling of the CO_2 concentration. Using the same scenarios and GFDL-CM2.1, Williams (2017), built on this previous paper by breaking down MOG into five severities. Light, light to moderate, moderate, moderate to severe and severe CAT frequency increased on average by +59%, +75%, +94%, +127% and +149% respectively over the North Atlantic. Storer et al., (2017), using the Met Office Hadley Centre HadGEM2-ES GCM (part of CMIP5), investigated the global shifts to CAT across these five severities. The HadGEM2-ES model has a horizontal mesh grid spacing of 1.25° by 1.875° in latitude and longitude. From a pre-industrial control state to a future 2050-2080 simulated atmosphere , the largest increase in CAT developed within the mid to high latitudes, over the busiest flight paths. The projected severe CAT rates increased over the North Atlantic, Europe, North America and North Pacific by +181.4%, +160.7%, +112.7% and +91.6, respectively. Despite smaller changes over Africa, South America and Australia, a global increasing response in CAT developed across atmospheric pressure levels of 200 hPa and 250 hPa. Over the North Atlantic, Storer et al., (2017) projected a significant increase in summertime CAT, with a concluding point that summertime CAT in 2050-80 was as common as wintertime CAT from their control period. Storer et al. (2017) also focused over the Asian continent, projecting a change of +102.5%, +92.4%, +78.1%, +59.2% and +64.1% at 200hPa for light, light to moderate, moderate, moderate to severe and severe turbulence. Storer et al. (2017) analysed projections focus on the high end of greenhouse gas emission scenarios, with the largest CO_2 emissions (Representative Concentration Pathway 8.5, RCP8.5). RCPs, which apply different climate concentrations and atmospheric forcing dimensions, have now been replaced by Shared Socioeconomic Pathways (SSP) within CMIP6 GCMS. SSPs build on RCPs but include key scenario drivers such as human population, economic growth and urbanization (Riahi et al., 2017).

Hu et, al (2021), focusing over East Asia and using an ensemble of CMIP5 regional climate models (RCM) and GCMs, found a significant increase in CAT by +6.9%, +9.1% +12% , +13% and +15% for light, light to moderate, moderate, moderate to severe and severe turbulence. The potential CAT increase was found greatest over the 35-50°N. This paper's simulated future projections used the RCP8.5 climate warming metric. Kim et al. (2023) also projected an increase in CAT by +7 to +80% and +14 to +116% across multiple regions of the globe for MOG turbulent events in their respective summers and winters. This paper found an global increase for all seasons across three types of upper-level atmospheric turbulence (CAT, MWT, NCT), with the greatest seasonal increase, averaged across the different types, by +91%. Kim et al., (2023) projects future shifts to CAT, MWT and NCT within a CMIP6 GCM, using a high end SSP5-8.5 scenario. SSP5-8.5 implies a fossil-fueled pathway for the future, with an increase in competitive markets and technology

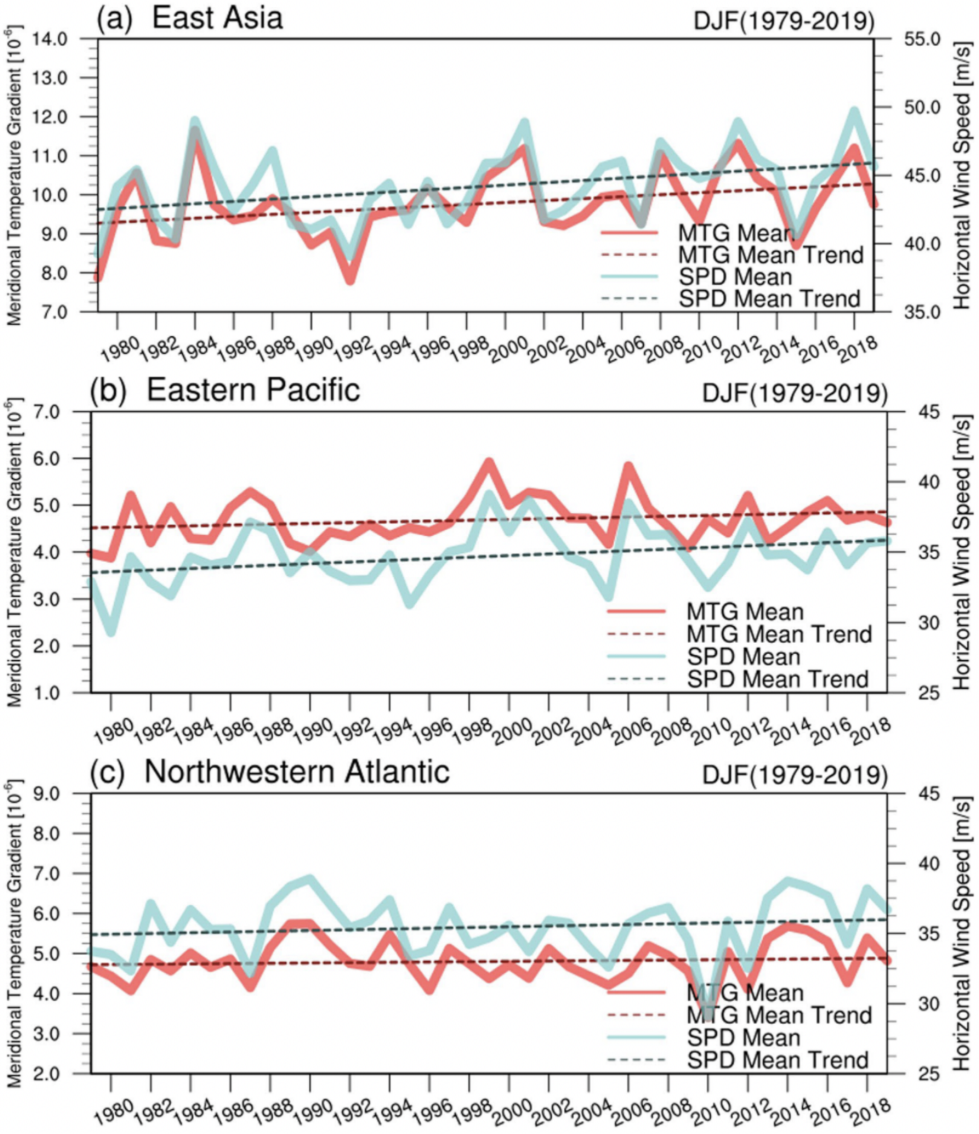

FIGURE 1.2: Lee et al. (2023) published fig. showing yearly (only NH winter) meridional temperature gradient values (pink solid line), and horizontal wind speeds (SPD) values (light blue solid line) over a 41 year period. East Asia (170°E to 130°W, 35 to 55°N), Eastern Pacific (170°E to 130°W, 35˘55°N) and northwestern Atlantic (80˘20°W, 35˘60°N) focuses findings are displayed with subplots a), b) and c), respectively.

but high challenges to mitigation. RCP8.5 and SSP5-8.5 share the same radiative forcing, with an assumption that since the industrial resolution (1750) to the future year 2100, an increase of 8.5 watts is applied per meter squared (Riahi et al., 2017).

GCMs are one way to effectively project the future of atmospheric turbulence with global warming. Williams et al. (2022) evaluated CMIP5's HadGEM-ES model against ECMWF ERA5 data, and found good agreement, suggesting that GCMs are capable of diagnosing CAT in future scenarios. Re-analysis datasets are created through blending observations, satellite data and short-term forecast data sets to encompass previous atmospheres, with ERA5 the 5th generation of ECMWFs re-analysis data developed by the Copernicus Climate Change Service (ECMWF, 2024).

Prosser et al. (2023) and Lee et al. (2023), using ERA5, found significant evidence that CAT frequency has globally changed over the past 40/41 years. Over the North Atlantic, Prosser et al. (2023) found NH winter, summer, spring and autumn have had a absolute increase in the number of hours (h) of turbulence between 1979 and 2020 by +26.7 h , +10.4 h, +26.0 h and +20.1 h for light or greater (LOG) turbulence. For severe or greater (SOG) turbulence, the number of hours increase by +3.1h, +1.9h, +2.3h and +2.4h, respectively, which is an overall increase by +49%, +52%, +85% and +47% for each season. Lee et al. (2023) concluded the greatest increase in MOG was evident over southeast Asia, with the strengthening of the East Asian jet closely linked to an anthropogenic steepening of MTG between the tropics and eastern Eurasia. Positive temperature gradients also arose over the eastern Pacific and northwestern Pacific as shown by fig. 1.2. This fig. shows the increase in the MTG and horizontal wind speeds (SPD) over these three previously touched on regions. Lee et al. (2023) using linear regression to assess the trends found an increase of +10.9%, +7.6% and +3.4% for the winter MTG and +8.0%, +6.9% and +3.0% in SPD over the 41 year period over East Asia, Eastern Pacific and northwestern Atlantic, respectively. Overall, this correlated with the greatest increases in NH winter CAT over the four decades, found in the region the greatest change in MTG and SPD.

1.2.2 Determining clear air turbulence in the atmosphere

Forecast predictions for atmospheric turbulence first began to developed in the second World War, with different synoptic scale features correlating to observations of CAT (Sharman and Lane,2016) as aircraft first reached altitudes near the tropopause (Ellrod et al., 2015). Since then, the world of meteorology and CAT forecasting has rapidly developed to the point where CAT forecasts are 75-80% accurate (Wolff and Sharman, 2008). There are two World Area Forecast Centres (WAFC) responsible for forecasting severe weather that impact aviation on a global scale (Gill, 2014). WAFCs were developed by the International Civil Aviation Organization (ICAO) in 1982 in collaboration with the World Meteorological Organization (WMO) (Kim, et al., 2018). These two centres are located in Kansas City, MS, USA (US National Weather Service) and Exeter, UK (UK Met. Office). They produce Significant Weather Charts (SigWX) to the public, private and governmental sectors, previously 4 times a day (Gill, 2014). Recent updates have allowed the WAFCs to provide data with 3 hr time steps with a full automated and new format. SigWX are developed through the World Area Forecasting Systems (WAFS), which has also been updated with finer grid model resolution and increased vertical levels. These updates will aid future CAT forecasting. CAT WAFS, and SigWX use an output tool refereed to as the graphical Turbulence Guidance (GTG). GTG is now on its 4th iteration, and uses a range of indices to represent CAT in the atmosphere (Met. Office, 2024).

Weather and climate model estimates of aviation turbulence use indices to represent CAT within the atmosphere, due to the difficulties in resolving turbulent kinetic energy within NWP and GCMS. It is assumed that large scale eddies eventually cascade down the inertial sub-range in to the micro scale (Sharman et al., 2006). The upper percentile values of each index are associated with an eddy dissipation rate, and thus a severity of CAT. Through applying a range of indices, one can effectively encapsulate different scenarios in which CAT can develop (

Sharman et al., 2006). To verify the accuracy of each index, relative or receiving operating characterise (ROC) curves are often applied to diagnose the probability of detection.

For CAT index verification, ROC curve analysis uses EDR$^{1/3}$ thresholds to derive probabilities of detection, and create a ratio between true or false alarm rates. The difference between the probability of true positive and false positive, shown effectively by the area under the curve (AUC) within fig. 1.3, determines the discrimination skill of the index (Gill and Buchanan, 2014). The black dashed diagonal line within fig. 1.3 represents a line of no skill. If an index successfully diagnoses CAT, with no probability of false detection, AUC would be equal to 1 (Gill,2014). PIREP collated EDR values are often applied as the reference data, to verify the ROC curve analysis and define a True or False positive (Sharman and Pearson, 2017).

In terms of research projects, PIREP datasets are effective for testing CAT indices or in representing the climatology of CAT over a region (Wolff and Sharman, 2008). However, there is a limited amount of PIREPs for moderate to severe events, especially since operational aircraft try to avoid encounters with turbulence as much as possible. In terms of a complete dataset, spatially and temporally there are gaps when just using PIREP information (Gill,2014), as they report one single isolated event rather then the longevity of a patch of turbulence (Lane

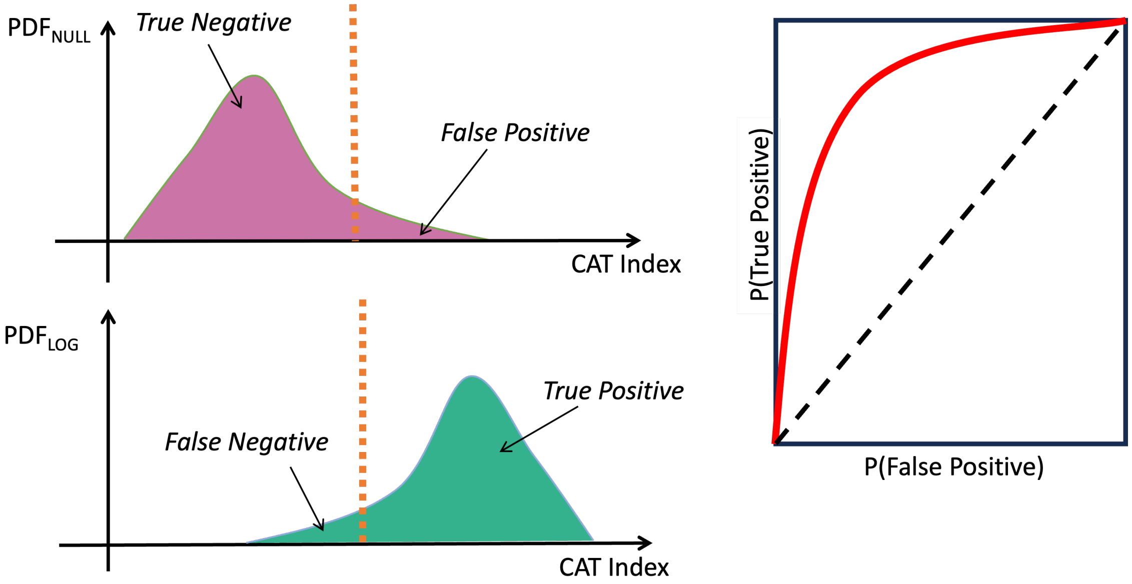

FIGURE 1.3: Simplified diagram exploring the probability density function (PDF) of lighter or greater (LOG) against CAT, or MWT index for the bottom left green density plot, and probability density function of a Null result against the same index in the top left pink density plot. The probability (P) of a True positive and False positive are plotted in the right hand subplot, with the red curve showing an arbitrary example. The area under the red curve relates to how well the index is able to diagnose turbulence. The dashed line represents a point where the probability of true and false positives are equal, so the index has no skill in diagnosing turbulence.

et., al, 2009).

PIREP also have different pilot experience biases (Lane et., al 2006), as well as median uncertainties of 50km horizontally, 200s in time and 70 m vertically away from the actual area of CAT (Sharman et al., 2006). Modelled data, and re-analysis data, are often used over PIREPS when investigating changes in CAT in time and over large regions such as the North Atlantic basin. This was highlighted previously in Section 1.2.1, with CMIP3 and CMIP5 GCMs projecting future trends in CAT. These GCMs have now been surpassed by CMIP6, with a wide range of available resolutions. CMIP6 has a subsection of fine resolutions, which one could suggest are capable of resolving a patch of turbulence, based on the size found in Sharman et al. (2014). Further information on these models are found in chapter 2.

1.3 Mountain wave turbulence

Mountains often act as a topographic barrier to low-level wind. Orographically forced airflow can develop large amplitude gravity (lee) waves, that horizontally and vertically propagate and often break at typical commercial aircraft cruising altitudes (Sharman and Lane,2016). The steepening, overturning and breaking of these wave comes from the amplitude growing with the reduction in air density in height (Kim et.al, 2018) or certain upper-level atmospheric conditions, such as opposing wind shear (Smith, 1989) developing the wave. The wave amplitude and development is dependent on the background winds and the stability across the atmospheric vertical profile (Kim et al., 2018). Atmospheric wave breaking can arise through nonlinear effects at a critical level or even by encountering jet stream cores, that exist below the tropopause. The breakdown is highlighted in fig. 1.1. The critical level is defined as a point the phase speed of the wave is equal to the background wind projected onto a horizontal wind vector (Kim et al., 2018 ; Lane et al., 2009 ; Sharman and Lane, 2016). In relation to MWT, the critical level often occurs as the wave transitions across the tropopause into a more stable atmosphere. At this point, the vertical wavelength decreases, aiding the breakdown of the gravity waves, leading to upper-level turbulence (VanZandt and Fritts, 1989).

In the 1990's MWT was responsible for 30% of all turbulence encounters over land (Turner, 1999). Within the upper troposphere and lower stratosphere, MWT is the most critical single mechanism that impacts aviation safety, assuming a reduction in surface effects and cloud or precipitation hazards, around mountainous terrain (Lane, et al.,2009). In fact, within a 12 year climatology, over the western half of the USA, MWT was found to be the major source of upper-level turbulence (compared to CAT, NCT, CIT), particularly in NH winter (Wolff and Sharman, 2008).

In comparison to NH summer, winter had 90% more MWT events over the USA which was linked strong winter low-level westerlies over the Rocky Mountain Range and lower troposheric heights. Within the boundary layer, lee waves can become trapped and break downstream of the mountain, with peaks and rotors of the wave generating low-level turbulence (LLT). These rotors, highlighted in fig. 1.1, are dangerous small-scale circulations, which can be identified by rotor clouds that cap the rotation under the crest of the lee wave (fig. 1.1) (Sharman and Lane, 2016).

1.3.1 Climate change; impact on mountain wave turbulence

Rainfall rates globally have increased with global warming, due to the duration and intensity of storm systems shifting. Despite this increase leading to high amount of general erosion, the rate of global warming is much faster than that of a mountain eroding. Therefore, any future shifts in MWT due to global warming are only associated with shifts in low-level wind speed or changes to upper-level conditions. As touched in section 1.2.2, Kim et al. (2023) found a projected increase in MWT, as well as NCT and CAT, within NorESM2-MM, a CMIP6 GCM with a grid spacing of 0.94° by 1.25° (latitude by longitude). Over the mid to high latitudes in the NH, MOG MWT had a estimate median relative increase of +26 to +84% between a historical period of 1970-2014 and future SSP5-8.5 atmosphere of

2056-2100. The region with the greatest average increase in projected MOG MWT arose over summer-time North America by +84%. Over the range of indices, the minimum change in this region and time was -35.1% and maximum at +292.5%. This publication only has two regions with an median decline in MOG MWT, these are the North Atlantic (including Greenland) in winter (-8.9%) and Europe in summer (-0.8%). These regions also had a reduction in wind stress and near surface wind flow.

The energy sector has produced a wide amount of research in the near-surface wind flow, with the importance on wind turbines and implication of renewable energy sources. Near surface wind speed, 10m above the surface, have dropped globally by -8% between the 1980 to 2010 (Zeng et al., 2019), with a projected decline of -21% by 2100. This reduction in wind flow is known as terrestrial stilling (TS), and has the potential to impact the energy center, the hydrological cycle and accumulations of low-level pollution (Deng et al., 2022). Interestingly, in 2010, there was a turning point with a global increase in near surface wind speed. This shift mostly developed within the northern mid-latitudes, with 79% of stations showing a rise from North America, Asia and Europe. There are several hypotheses for TS and its recent reversal, with TS linked to changes in large-scale circulations, urbanisation increasing terrestrial roughness (Zeng et al., 2019) and the reversal linked to a possible connection between modes of variability such as the

Tropical Northern Atlantic Index (TNA), North Atlantic Oscillation (NAO) (Zeng et al., 2019) or the Atlantic Multidecadal Oscillation (AMO) and Pacific Decadal Oscillation (PDO) (Deng et al., 2023). Interestingly, Deng et al. (2022), using observations from the Global Surface Summary of Day database and range of CMIP6 GCMs, projected that NH TS was likely to continue into the 21st century within a number of future scenarios, despite the recent reversal. Kim et al. (2023)'s interesting connection between a drop in MWT and slower surface wind flow, may imply TS could have an impact of future MWT production rates.

1.3.2 Determining mountain wave turbulence in the atmosphere

MWT and CAT are not detectable by on-board radio detection and ranging (radar) equipment, due to the lack of water droplets to detect. Ground Doppler radars have the potential to determine altitude and intensity of CAT through very high frequency wind profiles when focusing on atmospheric features conducive to CAT (Chapter 2) such as jet streams (Ellrod et al., 2015). Light Detection and Ranging (lidar), using the ultra violet (UV) Rayleigh spectrum, has been found to detect light to moderate and moderate MWT/CAT at distance of 5km and 10km in front of an aircraft, respectively. This is through the ability to pick up air density fluctuations (Vrancken, et al., 2016). There is no public information on any plans of implementing UV LIDAR equipment on aircraft fleets, although Kauffmann (2002) found it more cost effective for the aviation sector to pay insurance claims than implement LIDAR on all aircraft. Several studies have used satellite imagery to determine regions of MWT, assuming that lenticular high to mid-level clouds or capped rotor clouds at low levels (shown in fig. 1.1) are associated with mountain wave generation and upper-level turbulence signatures (Lane et al., 2009). Fohn gaps, highlighted in fig. 1.1, are linked to intense mid-level turbulence, and can be detected through a plume of cirrus downstream from mountainous terrain (Ellrod et al., 2015). Remote sensing can be used for short scale forecasting through detection of circus clouds for both MWT and CAT.

However, in terms of long-range forecasting and researching projected MWT in future scenarios (Kim et al., 2023), indices are applied to diagnose this type of turbulence. The theory around how MWT develops is well documented, but the nonlinear processes (Gill and Striling, 2013) and the wavelengths of these inertial gravity waves and associated turbulent eddies, are on a scale (tens of kilometers) too small to represent in operational NWP and climate model data (Sharman and Pearson, 2017). Through ROC analysis and PIREP data sets over North America, Sharman and Pearson (2017) verified that an ensemble of MWT diagnostics can effectively determine MWT at these upper-levels. This ensemble of MWT indices, which are found in WAFC's GTG system, scored a high verification of 0.989 (AUC) for upper-level heights. As shown in fig. 1.2, this AUC score is associated with a high probability of detection, with a large rate of true positive events. Further information of MWT indices, and their relation to CAT indices, are discussed in Chapter 2 of this thesis.

1.4 Other types of atmospheric turbulence

1.4.1 Convectively induced and near cloud turbulence

Large convective features and systems, that spread across the troposphere, can generate turbulence within its cloud or out of cloud, 10s of kms away from active sites. CIT (cloud induced) develops in cloud, due to strong updrafts and down drafts developing within deep convection, with MOG CIT associated with 9-12 km of vertical cloud depth (Wolff and Sharman, 2008). Clouds with such a vertical depth, are typically electrified, due to the separation of hydrometers by convection (MacGorman and Rust, 1998). Several studies show that lightning flash density rate, which is another dangerous phenomena for aircraft, can be related to MOG CIT frequency through similar conditions needed for both phenomenons to arise (Sharman and Lane, 2016). CIT only exists for a period of a few minutes, unless developed within a mesoscale convective systems (MSC) (Shaman and Lane, 2016), and is detectable by on-board RADAR equipment, so is not likely to strike an aircraft unexpectedly without warning.

NCT, which develops out of the cloud, like CAT and MWT is closely linked to gravity wave breaking and shear driven instabilities. The convective feature can develop inertial gravity waves that have horizontal wavelengths between 5 and 200 kms (Chun and Kim, 2008), breaking at their critical levels breaking into turbulent eddies. NCT can develop vertically above a convective feature, with deformation of convectively induced flow and buoyancy gradients, leading to enhanced wind shear (Kim et al., 2023, Lane et al., 2003). NCT can also develop below the cloud base, due to the rapid sublimation of ice and snow generating turbulence (Sharman and Lane, 2016). Kim et al. (2023) projected a global increase in the frequency of NCT, with regions such as the South Pacific, Indian Ocean and North America having the most substantial summertime rise of +114.3%, +101.6% and +104.5% between 1970-2014 and 2056-2100 (future SSP5-8.5 simulated atmosphere). The Intergovernmental Panel on Climate Changes (IPCC)'s sixth assessment report suggests high confidence in the projected increase in the frequency and intensity of severe convective systems, such as MCS, across a range of publications applying high resolution convection permitting regional models. Assuming this increase is related to a rise in deep vertical convective feature, one can expect an increase in CIT and NCT with global warming (IPCC, 2023).

1.4.2 Impact on airports

Within an airport, LLT and wake turbulence can be disruptive to aircraft take off and landing. LLT develops around the surface and can be generated by trapped mountain lee wave, surface fronts, and low-level thermal forcing. Wake turbulence, which is aircraft generated, can be a critical consideration for ground control scheduling. The majority of aircraft that take flight, and gain lift, form two rotating vortices off the winds, which can develop into trailing vortex rolls. The vortex velocity is dependent on the aircraft size and weight, with wake turbulence becoming more serious in the 1970s after the beginning of operation for Boeing 747, a wide-winged heavier aircraft manufactured by Boeing Commercial Airplanes (Gerz et al., 2002). The FAA have air traffic distance guidelines to avoid wake turbulence, as it can lead to loss of aircraft control situations (FAA; Aircraft Wake turbulence, 2024). With distances spanning between 4 to 8 miles depending on the configuration of aircraft order and weight comparisons (FAA; Aeronautical information Manual, 2024). Airports and aviation are also likely to be impeded by other meteorological variables changing with global warming. Coastal airports have already been impacted by rising sea levels. Anthropogenically prolonged heatwaves will impact aircraft lift and the increasing number of extreme weather events may lead to poorer flying conditions, delays and accidents (Puempel, 2016).

1.5 Thesis Aims

Upper-level atmospheric turbulence is changing with global warming, with world wide CAT rates increasing rapidly over the last 40 years (Prosser et al., 2023; Lee et al., 2023) and projected to continue in this trend till the end of the century (Williams and Joshi, 2013; Williams, 2017 , Storer et al., 2017; Kim et al. , 2023). The majority of these studies apply CMIP3 or CMIP5 GCMs, which have now been surpassed by the newest phase, CMIP6. These publications apply one set of modelled data for their future projections, and in doing so do not get a spread across projections for different models. One uncertainty in climate modelling is "response uncertainty", with models using the same climate warming metric simulating difference future responses (Hawkins and Sutton, 2009). Previous atmospheric turbulence research has not explored response uncertainty, and has therefore limited the certainty in their findings. There is a gap in the scientific community for research on projected CAT, as verified across a range of GCMs, with differing simulated atmosphere resolutions.

Within several papers, a percentage increase in CAT is the main way of presenting a change in this type of atmospheric turbulence in time. Despite this being an effective way of determining an overall change in CAT, it does not explore the physical representation in the atmosphere. Does the increase in CAT over the last

40/41 years, shown by Prosser et al., 2023 and Lee et al., 2023, equate to more patches or larger patches of turbulence? As CAT patches are vertically thin (1km in depth) and horizontally wide (60-70km), focus on horizontal grid spacing for the simulated atmospheres is important, with a range of resolutions effective for understanding projected trends. Understanding how the patches of CAT could change is another key area of research that has not been tackled previous in CAT literature.

Due to the dangerous and sudden impact CAT can have on an aircraft, several aforementioned studies have investigated CAT in future atmospheric scenarios. However, there are a limited number of papers that focus on MWT trends in time. Kim et al. (2023) is one publication that address this key gap in literature. However, its results focus on a change between 1970-2014 to 2056-2100. Future projections for the next few decades, prior to 2056, also need to be addressed. Global MWT future projected trends, across a number of GCMs, is a key area to develop within the turbulence research community.

Due to these gaps in the scientific atmospheric turbulence literature, this thesis aims to;

1. Quantify change in CAT within a range of CMIP6 GCMs, with the main focus over the North Atlantic. Within this aim, evaluating the systematic

relations between climate model resolution and projected turbulence will also be addressed.

2. Understand if patches of CAT may vary in a future scenario due to a change in frequency or size, across a range of GCMs, over the NH and SH latitudes where CAT is most prominent.
3. Globally quantify shifts in MWT within a range of CMIP6 GCMs and address the shifts in MWT prior to 2056. Understand if terrestrial stilling is having an impact on MWT within these GCMs.

This thesis will discuss the methods and GCMs applied to address the above aims in Chapter 2. The investigation and manuscript for each aim is presented between Chapters 3-5. A summary and impacts of results are discussed in Chapter 6.

Chapter 2

Methodology and data

This thesis is written through manuscripts, with individual results chapters including specific methods and data sections for the related paper. To reduce repetition this chapter discusses the background assumptions and theory as to why indices are applied to represent CAT and MWT (Section 2.1 & 2.2). All findings within this thesis use CMIP6 GCMs, hence a final section of this chapter discusses these models and their limitations (Section 2.3).

2.1 Diagnosing Clear Air Turbulence

As briefly discussed in the introduction, CAT forms around upper level jet streams, in regions of increased shear production. Wind shear, along a density interface, can develop through different vertical and horizontal mechanisms. Large scale shearing and stretching deformation zones can amplify horizontal and vertical temperature gradients, increasing the probability of CAT through production in KHI and reduction in the Richardson number (Ri) (Overeem, 2002). Ri is a dimensionless atmospheric quantity that determines the ratio of turbulence production by buoyancy to velocity shear, it is also often used to characterise the stability of the atmosphere (Nappo , 2012). Using the Mile-Howard criterion, if Richardson number (Ri) is less than 0.25, unstable waves resulting from vertical shear are extremely likely to occur. If Ri is more than 1, and KHI is present, the wave amplitude will decrease. Ri$\leq$ 0.25 requires strong vertical wind shear and a weak thermal stratification (shear equation denominator). **Negative Ri** is an index used within this thesis to quantify this dynamically unstable large-scale flow. Aircraft-scale turbulence exists due to the injection of energy at large scales that cascade downscale to aircraft sized eddies. CAT develops with energy quickly dissipating from KHI into small-scale turbulence through the inertial sub-range (Ellrod et al., 2015). The inertial sub-range is a region where only inertial forces are responsible for transferring energy from larger scales to smaller scales. Within the boundary layer and free atmosphere, turbulent eddies in the inertial sub-range range from a few meters to scales where viscous effects become significant.

TKE is on a scale too small to be resolved by even the finest regional climate models to date. Therefore, to represent CAT within this thesis, twenty-one indices are applied to modelled data, with the assumption that EDR $^{1/3}$ equates to upper-percentile ranges for each index. This thesis follows suit to Williams (2017) that defined the upper percentage ranges of 97.0-99.1, 99.1-99.6, 99.6-99.8, 99.8-99.9 and 99.9-100%, linked to 0.1-0.2, 0.2-0.3, 0.3-0.4, 0.4-0.5 and >0.5 $m^{2/3}$ s^{-1} for EDR $^{1/3}$, for light, light to moderate, moderate, moderate to severe and severe CAT. These turbulence intensities are related to deviations in vertical acceleration from the normal acceleration of gravity (1g) of an aircraft by 0.2-0.4, 0.4-0.6, 0.6-0.8, 0.8-1.0 and >1.0 g, respectively (Ellrod et al., 2015; Williams, 2017). These values are for a large commercial aircraft, a type of craft expected for transatlantic travel. Williams (2017) focus on the North Atlantic flight corridor (50–75°N, 300–350°E). Within Chapters 3 and 4, threshold values, differing across the twenty-one indices, are based on the above percentage ranges for each index averaged over this transatlantic basin, for the decade 1950-1960 over all seasons.

2.1.1 Favourable conditions for CAT production

An ensemble of indices is applied, within this thesis, due to the nature of CAT developing from a number of atmospheric scenarios across synoptic, mesoscale and microscale situations. Fig 2.1 highlights four differing jet positions that are extremely favourable for CAT to form (hatched region). The purpose of this figure is to highlight that curved jet streams, in combination with upper-level troughs and ridges can often be more turbulent than a typical zonal jet stream (Ellrod et al., 2015). Troughs and ridges are elongated areas of high and low atmospheric pressure. Therefore, this thesis applied a considerable number of indices to represent the jet in a number of situations, and to capture different CAT formation situations, as discussed further below.

Scenario 1 in fig.2.1 portrays a col pattern with the combination of surface low-pressure, an amplified ridge and a slightly positively titled trough. Positively tilted implies the trough is leaning towards the north east (south west) in the NH (SH). Scenario 4 portrays a negatively tilted trough, which leans towards the north west (south east) in the NH (SH). Scenario 1 encompasses several dynamical ways CAT can develop. CAT could be generated north to northwest of the surface low, with enhanced cyclogensis aiding flow deformation and vertical wind shear production. **Flow deformation** and **Magnitude of vertical wind shear of horizontal wind** are two indices applied within this thesis to diagnose CAT.

Across our twenty-one indices, several share elements. For example, several diagnostics build on flow deformation and wind shear, such as **Flow deformation times wind speed**, **Flow deformation times vertical temperature gradient**,

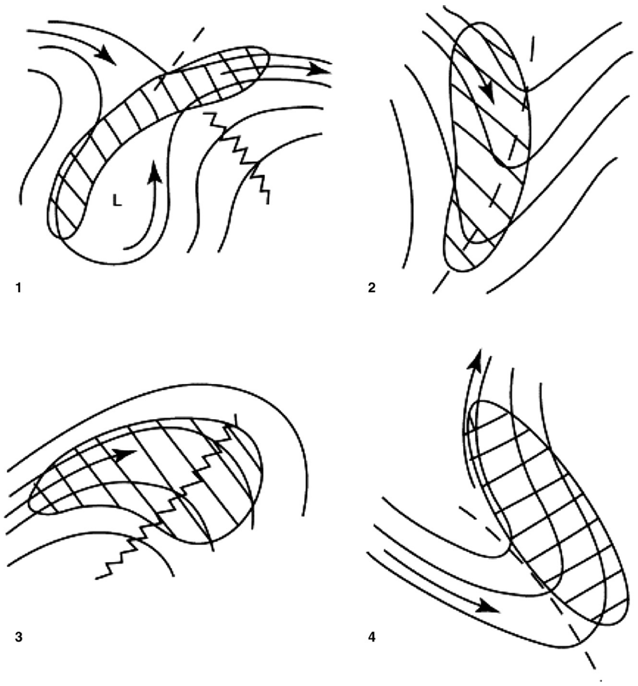

FIGURE 2.1: Simplified streamlines of jet stream scenarios in which flow patterns are favourable for CAT production (Hatched areas). The lines with arrows are linked to the jet stream locations. Scenario 1,2,3 and 4 are related to a col pattern, a sharp trough, a ridge, and a negatively titled trough. Sourced from Ellrod et al. (2015).

Brown index (contains flow deformation), **Brown energy dissipation rate** (contains flow deformation and wind shear), **Variant 1 Ellrod index** (contains flow deformation and wind shear) , **Variant 2 Ellrod index** (contains flow deformation and wind shear), **Colson–Panofsky index** (contains Wind shear) and **Negative Ri** (contains wind shear). The **Colson–Panofsky index** is effectively representing the vertical kinetic energy in a system (proportional to the TKE), but in its break down it is a combination of Ri and the vertical wind shear (Colson and Panofsky, 1965).

Within Scenario 1 in fig 2.1, the amplifying ridge could lead to a breakdown in anticyclonic flow. Anticyclonic flow (clockwise in NH and anti-clockwise in SH) can only develop to a certain curvature before the absolute rotation combats the planetary rotation, developing inertial instability and horizontal divergence of air parcels. This ridge and the jet core could be experiencing a large latitude displacement, leading to geostrophic imbalance. This would lead to an ageostrophic adjustment of air being brought back to geostrophic balance, where the Coriolis force and the pressure gradient force are equal. Ageostrophic flow enhances vertical wind shear which generates KHI and CAT production. Here we list other the indices, not previously mentioned, able to represent this scenario; **Magnitude of horizontal divergence**, **Magnitude of potential vorticity**, **Magnitude of residual non-linear balance equation**,**Version 1 of North Carolina State University index**, **Negative absolute vorticity advection** and **Magnitude of relative vorticity advection**.

Since this anticyclonic scenario would generate shearing winds, the first list of indices would also effectively represent this CAT production situation. Wind shear around Scenario 1 also relates to the slight positive tilt. If this depiction had a stronger positive tilt (tilted further towards the north east), directional wind shear would be enhanced, due to the ridge feature being influenced by a strong cyclonic flow. **Wind speed time directional shear** is an index that would effectively represent that situation.

The amplifying ridge pattern is also apparent in Scenario 3 within fig 2.1, with CAT development aided through anticyclonic shear, released inertial instability and geostrophic imbalance. A ridge pattern (scenario 3), from observations, is linked to the highest frequency of CAT (Ellrod et al., 2015). However, Ellrod et al. (2015) discusses that Scenario 2 is associated with the highest percentage of intense CAT. This pattern portrays a slightly positively titled upper-level trough with a strong wind maximum upstream of the trough. This scenario is favourable for CAT generation through a wide range of dynamics. Upstream of the trough upper-level convergence has developed aiding the production of gravity waves (and therefore CAT) through subsidence. The curve of the flow also develops an increase in geostrophic imbalance which enhancing wind shear. Unbalanced ageostrophic flow is associated with a number of scenarios such as diverging air flow, intensified jet streaks and curvatures in flow (ridges and troughs) (Sharman and Lane, 2016).

Within Scenario 3, cold air advection could also arise and develop an air mass density discontinuity and KHI (Sharman and Lane, 2016). All previous indices could effectively represent this situation. Several indices, not yet discussed, could also diagnosis CAT here, particularly through the gravity wave breaking. These include **Magnitude of relative vertical vorticity squared**, **Magnitude of horizontal temperature gradient** and **Wind speed**. Atmospheric gravity waves, which propagated vertically in the atmosphere, typically overturn and breakdown in TKE (KHI) at horizontal wavelengths ranging from a few meters to a few kilometers. Gravity wave motion itself can even develop micro-scale KHI through vertical flow displacements, aiding CAT development (Ellrod et al., 2015).

Scenario 4 depicts a negatively titled upper-level trough, with increased CAT production evident downstream from the maximum in curvature. In this scenario, CAT development associated is with cyclogenesis, with CAT developing before the trough, suggesting a barolcinic zone underneath the jet core. This scenario often develops thick cirrus clouds (Ellrod et al., 2015). Cirrus has been linked to jet scenarios with enhanced deformation zones (Scenario 1) and steep troughs (Scenario 2) (Ellrod et al., 2015). Fig 2.1 is effective in highlighting the many mechanisms CAT can develop from, but does not encapsulate all such mechanisms. CAT can develop through the breakdown of internal gravity waves, and even from the existence of waves modulating background wind shear, leading to mircro scale KHI (Ellrod. et al., 2015).

CAT is also associated with tropopause folds, effectively represented by the **Frontogensis function** (Kim et al., 2018), which is incorporated within the GTG tool and is linearly proportional to flow deformation (Knox, 1997). **Frontogensis function** was found to be the best single diagnostics to represent CAT in the mid to upper levels (Sharman et al., 2006) but was also found to often overestimate CAT in certain scenarios (Knox et al., 2008). This thesis applies an ensemble of indices to effectively cover as many scenarios as possible that generate CAT, either through theoretical connections to CAT or through prognostic methods of verifying indices. Indices and equations are listed in full in Appendix A.1.

2.2 Diagnosing mountain wave turbulence

This thesis follows previous literature (Kim et al., 2023 ; Sharman and Pearsons, 2017) and makes the assumption that MOG MWT is arising globally at the 98% percentile of each MWT index. Indices are applied to represent MWT in our projected atmosphere, due to the similar issue of TKE small-scale nature. Sharman and Pearsons (2017), through a combination of CAT indices, several ground surface variables and PIREP data, found that the most effective way to represent MWT with current model resolution was to combined a CAT index with near-surface wind speed, terrain gradient and terrain height. Despite wind speed direction applied in different algorithms (Turner, 1999), Sharman and Pearson (2017) determined wind direction and vertical velocity unnecessary through low statistic scores. Several CAT indices were applied but fourteen indices overall proved effective in diagnosing MWT over the continental USA, with all indices performing with an AUC (ROC analysis) above 0.85. The ROC curve analysis provided an average of 0.989 for MWT indices and 0.965 for CAT indices used within the GTG ensemble (Sharman and Pearsons, 2017).

The **Magnitude of horizontal temperature gradient** (CAT index), combined with terrain height, gradient and low-level wind speed, produced a AUC of 0.991 for high altitudes over the USA. This MWT index, with five others from the 14 indices in Sharman and Pearsons (2017), is applied in Chapter 5 of this thesis. This indices are **Frontogensis function**, **Magnitude of horizontal divergence**, **Wind Speed**, **Flow Deformation** and **Flow deformation times wind speed** (Chapter 5). Unfortunately the remaining 5 indices applied in Sharman and Pearsons (2017) and Kim et al. (2023) had aspects not available from our CMIP6 GCMs.

The MWT indices are chosen through prognostic methods, with verification of results a key factor as to their application. These indices at 98% rate, are associated with increase in instability (KHI), which correlates with a break down of mountain generated gravity wave.

2.3 Global climate models

To effectively investigate future trends in atmospheric turbulence over time, it is beneficial to use modelled data, with three dimensional values spread out equally in time and space. CMIP6, the 6th and most recent CMIP phase, has a subsection of high resolution models, developed as part of the High-resolution intercomparison project (HighResMIP). HighResMIP was created for the scientific community to evaluate the dependence of a particular phenomenon on model resolution and to reduce the resolution gap between NWP and GCMs (Haarsma et al. 2016). Many of the models and experiments contributing to HighResMIP were developed with the PRIMAVERA (PRocess-based climate sIMulation: AdVances in high- resolution modelling and European Risk Assessments) project.

For an effective multi-model comparison, three GCMs each with several resolutions, are applied across this thesis. The Met-Office Hadley Centre coupled model HadGEM-GC3.1 has three simulated atmosphere and ocean grid spacing domains of 25km (-HH/HM), 60km (-MM) and 135km (-LL) (Roberts et al., 2019). HadGEM-GC3.1-LL is the coarsest sub-model applied in this thesis, with its finest counterpart (HadGEM-GC3.1-HH/HM) the overall highest resolution model applied. The Max-Planck institute MPI-ESM1.2 provides two sub-models with atmospheric grid spacing's of 34km (-XR) and 67km (-HR) (Gutjahr et al., 2019). Within this thesis a sub-model refers to a model within each overarching GCM, with the number of models related to the number of resolutions within each GCM. For example MPI-ESM1.2 is the overarching GCM, with two sub models MPI-ESM1.2-XR (34km) and MPI-ESM.1.2-HR (67km). The third, and final, GCM is EC-Earth3P , also with two sub-models or simulated resolutions, EC-Earth3P-HR with an atmospheric grid of 36km and EC-Earth3P with 71km (Haarsma et al.,2020). The EC-Earth models were developed by the EC-Earth consortium, which is a collaboration project across of 27 research institutions over 12 European countries (EC-Earth, 2024). CAT has not been previously investigated with models that get this close to resolving individual patches of turbulence, with the median patch of CAT horizontally 60-70kms, and 1km vertically (Sharman et al., 2014). The horizontal resolution is are of key importance in this thesis, due to the wide yet thin nature of patches of CAT in the atmosphere.

The CMIP6 GCMs forcing chosen are within Tier 2 of HighResMIP experiments, with coupled ocean and atmosphere simulations, that span the period 1950 to 2050. Within this tier, the coupled historic runs, using fixed 1950 decade mean forcing for initial conditions, produce data between 1950-2014 and are referred to as "hist-1950". Future simulations apply the high-end SSP5-8.5 forcing, which are similar to RCP8.5, referred to as "highres-future", and include 2015-2050. The forcing and initialisation applied for all our GCMs and differences between time periods (pre-2015 and after-2015) projections are displayed in Table 2.1.

	Hist-1950	**Highres-future**
Period	1950-2014	2015-2050
Anthropogenic aerosol forcing	Concentrations used in Historic CMIP6 simulations	Specified aerosol optical depth and effective radius deltas from Macv2.0 SP Model
Natural aerosol forcing-dust	As used in Historic	ScenarioMIP
Volcanic aerosol	As used in Historic	ScenarioMIP
GHG concentrations	As used in Historic	SSP5-8.5
Ozone forcing	CMIP6 monthly concentrations, 3-D field or zonal mean, as in Historic	CMIP6 monthly concentrations, 3-D field or zonal mean 2015-2100, based on SSP5-8.5 ScenarioMIP
Solar variability	As in Historic	CMIP6 dataset
Imposed boundary conditions	Based on observations documented; land surface types, soil properties and orography. LAI to evolve consistent with land use change	Same as Hist-1950

TABLE 2.1: Forcing and initialization for the simulations used in this thesis. LAI and GHG stand for Leaf Area Index and greenhouse gases. ScenarioMIP links to Model Intercomparison Projects (MIP) high-end CMIP6 SSP5-8.5 scenario. Macv2.0 SP is a simplified aerosol forcing method (Haarsma et al, 2016).

2.3.1 Limitations of GCMs

Despite the application of HighResMIP high resolution GCMs in this thesis, the grid-spacing domain is still too large to represent the eddies that impact aviation, therefore the assumptions discussed in Section 2.1.1 are made. This thesis also applied daily data values, that are averaged often into yearly results. There are limitations to this with CAT short compared to daily averages. Due to limitations in the output available for PRIMAVERA only six MWT indices are applied in Chapter 6 and CIT and NCT are not included. The warming trend is the simulated response to the initial conditions and the forcing given within Table 2.1 and as such not a forecast but a possible future scenario.

Chapter 3

Trends in clear-air turbulence over the North Atlantic

Abstract

Clear-air turbulence (CAT) has a large impact on the aviation sector. Our current understanding of how CAT may increase with climate change in future is largely based on simulations from CMIP3 and CMIP5 global climate models (GCMs). However, these models have now been superseded by high-resolution CMIP6 GCMs, which for the first time have grid lengths at which individual turbulence patches may start to be resolved. Here we use a multi-model approach to quantify projected moderate CAT changes over the North Atlantic using CMIP6 models.

The influence of the model resolution on CAT projections is analysed. Twenty-one CAT diagnostics are used, in order to represent uncertainties in CAT production mechanisms. Each diagnostic responds differently in time, but the majority display an increase in moderate CAT between 1950 and 2050. Although winter is historically the most turbulent season, there is strong multi-model agreement that autumn and summer will have the greatest overall relative increase in CAT frequency. By 2050, summers are projected to become as turbulent as 1950 winters and autumns. The global-mean seasonal near-surface temperature is used as a comparative metric. For every 1 °C of global near-surface warming, winter, spring, summer and autumn are projected to have an average of +9%, +9%, +14% and +14% more moderate CAT, respectively. Our results confirm that the aviation sector should prepare for a more turbulent future, with increased stress on flight planning control, longer flight routes and further costs.

3.1 Introduction

Clear-Air Turbulence (CAT) is an upper-level atmospheric phenomenon that has a hazardous and expensive impact on the aviation sector. Atmospheric turbulence is the leading cause (71%) of all in-flight weather-related injuries (Hu et al. 2021) and annually costs the United States of America US$200 million (Williams

2014). CAT usually develops in cloud-free, stably stratified atmospheric environments (Jaeger and Sprenger 2007) and is undetectable using current on-board radar equipment. CAT develops in regions of shear-driven instability and is often found around upper-level[1] jet streams. Jet streams are narrow bands of intense winds, which have a strong seasonal dependence and owe their intensity to latitudinal horizontal temperature gradients. Due to the steepening of the pole-to-equator temperature gradient in the upper troposphere and lower stratosphere, jet streams are expected to intensify in wind shear with anthropogenic climate change (Lee et al. 2019). The extra annual cost on the aviation industry to avoid CAT is £16 million (Search Technology 2000).

In a future scenario, with double the pre-industrial CO_2 atmospheric concentration, longer transatlantic flights would add an extra 2000 hours of annual travel and an additional 70 million kg of CO_2 in annual fuel emissions (Williams 2016). In the same CO_2 scenario, Williams and Joshi (2013) projected winter-time moderate-or-greater CAT encounters to increase by +40 to +170% over the North Atlantic. Building on this previous work, and using the same CO_2 concentration scenario, Williams (2017) projected moderate CAT to increase by +94% in wintertime over the North Atlantic basin. Moderate turbulence inflicts vertical accelerations of up

---

[1] Defined here as a typical commercial aircraft cruising height, 300–150 hPa or 9000–14,000 m from the surface

to 0.5 g (4.9 m s^{-2}) on aircraft (Lane et al. 2004). Transatlantic air travel often confronts CAT due to the presence of the mid-latitude eddy-driven jet stream over the North Atlantic.

Williams and Joshi (2013) and Williams (2017) used a Coupled Model Inter- comparison Project phase 3 (CMIP3) coupled atmosphere-ocean climate model, with a grid resolution of 2.5° × 2.0°. The World Climate Research Programme (WCRP), previously called the World Group on Coupled Modelling (WGCM), first developed the Coupled Model Inter-comparison Projects in the 1990s, to evaluate and improve global climate models (GCM) and to understand future and past climate variabilities (Bock et al. 2020). The three latest generations are CMIP3, CMIP5, and CMIP6 (Bock et al. 2020). Hu et al. (2021), using CMIP5 GCMs for their control state and a regional climate model, found an increase in CAT severities across the South China Sea, with moderate turbulence increasing by +12% over 50 years.

Storer et al. (2017) also found a significant rise in moderate winter- time CAT across the globe. They projected an increase of +143%, +100%, +90%, and +127% at 200 hPa over the North Atlantic, North America, North Pacific, and Europe, respectively. Storer et al. (2017) used a CMIP5 GCM, namely the Met Office Hadley Centre HadGEM2-ES model. Williams and Storer (2022) compared this GCM against ERA-Interim reanalysis data from the European Centre for Medium

Range Forecasts (ECMWF) and concluded that GCMs can successfully diagnose CAT and its response to climate change, when compared to reanalysis data.

The horizontal resolution coarseness of CMIP3 and CMIP5 GCMs led to the development of the High-resolution inter-comparison project (HighResMIP), which is a subsection of CMIP6 (Haarsma et al. 2016). PRIMAVERA (PRo-cess-based climate sIMulation: AdVances in high-resolution modelling and European Risk Assessments), launched in 2015 to manage and collate GCMs, further aided the development of HighResMIP. HighResMIP was created for the scientific community to evaluate the dependence of model resolution on a particular phenomenon and to reduce the resolution gap between numerical weather prediction (NWP) models and GCMs (Haarsma et al. 2016).

Haarsma et al. (2016) suggested that an improvement in the horizontal resolution within a model could lead to a better representation of vertical dynamics in a system. For example, they found that vertically moving small-scale gravity waves were better represented in models with a finer horizontal resolution. The new CMIP generation also uses the Shared Socioeconomic Pathways (SSP) scenarios. These global warming simulations, within CMIP6, were found to better represent northern hemisphere (NH) storm tracks and jet streams, than CMIP5's Representative Concentration Pathway (RCP) 4.5 or CMIP3's special report emission scenario SRES A1B (Harvey et al. 2020). The experimentation of different emission scenarios has lead to further developed CMIP6 model climate sensitivity, in comparison to previous CMIP phases.

Upper-level atmospheric turbulence is anywhere from planetary to millimetres in horizontal size, but typically impacts aviation between 100 m and 1 km (Storer et al.2017). Sharman et al. (2014), using extensive pilot reports (PIREPS), suggest a climatology for the turbulent state of the upper atmosphere. They concluded that a median patch of turbulence was approximately 60–70 km wide horizontally and 1 km deep vertically. Several CMIP6 GCMs have a close capability to resolve this median length scale (Sect. 2; Methodology). CAT has not previously been investigated with GCMs with such a capability. Therefore, this paper explores projected moderate CAT changes in time and with anthropogenic climate change using CMIP6 HighResMIP GCMs. A multi-model approach is applied to understand the dependence of CAT projections on model resolution. This study includes all seasons, over the North Atlantic. The layout of this paper is as follows. Section 2 discusses the approach and GCMs modelled data used. The results are discussed in Sect. 3. Section 4 draws the main conclusions from these findings.

3.2 Data and methods

The Met Office Hadley Centre HadGEM3-GC3.1 model, the Max-Planck Institute MPI-ESM1-2 model, and the European community Earth systems EC-Earth-3 model are the three CMIP6 HighResMIP GCMs chosen for this upper- level turbulence analysis. HadGEM3-GC3.1 is the latest Met Office global climate model configuration and was the UK community's submission to CMIP6. This configuration has many new improvements and systematic error corrections compared to the corresponding CMIP5 submission (HadGEM3-GC2; Williams et al. (2018). HadGEM3-GC3.1 scored a high 727 out of 1000 on the Watterson et al. (2014) basic overall climate model metric, with HadGEM3-GC3.0 and HadGEM3-GC2 averaging at 711 and 686, respectively (Williams et al. 2018). HadGEM3-GC3.1 has three model resolutions available: HH/HM which has a horizontal grid spacing of 25 km, MM which has 60 km, and LL which has 135 km. The number of ensemble members for each resolution is found in Table 3.1.

Twenty-seven European research organisations and universities worked together to submit the updated version of EC-Earth to CMIP6. EC-Earth's new atmosphere and ocean model projections have finer horizontal and vertical resolutions than CMIP5's EC-Earth-2 GCMs (Haarsma et al 2020). Their HighResMIP sub-models

	Horizontal Grid Spacing; atmospheric mesh spacing at 50°N	Number of Ensemble members
HadGEM3-GC3.1	25 km (HH, HM)	1, 3
(From the UK Met Office Hadley Centre)	60 km (MM)	3
	135 km (LL)	4
EC-Earth 3	36 km (3P-HR)	2
(From a collection of European institutions)	71 km (3P)	2
MPI-ESM1-2	34 km (XR)	1
(From the Max-Planck Institute)	67 km (HR)	1

TABLE 3.1: The horizontal grid spacing and the number of ensemble members for three CMIP6 HighResMIP GCMs: EC-Earth3, HadGEM3-GC3.1, and MPI-ESMI-2 (Hasrsma et al. 2020, Roberts et al., 2019, Gutjahr et al. (2019)

are EC-Earth-3P (71 km) and EC-Earth-3P-HR (36 km). Due to a problem with greenhouse gas concentrations within ensemble member number 1 of EC-Earth-3P (71 km), two years (2013, 2014) are omitted from the EC-Earth-3P analysis in Sect. 3. The Max-Planck Institute Meteorology Earth System GCMs are the final models used within this investigation: MPI- ESM1-2-HR (67 km) and MPI-ESM1-2-XR (34 km). MPI- ESM1-2-HR had a computational cost 20 times greater than its older, coarser version (-LR). This has led to improvements in representations of teleconnections and mid-latitude dynamics (Mauritsen et al. 2019). The Max-Planck Institute sub-models only have one ensemble member (Table 3.1). The CMIP6 GCMs have three main tiered experiments. Of these, the historically forced coupled climate and ocean experiments (hist-1950) and the future projected forcings of 2015–2050 (highres-future) were used. Future projections (2015–2050) simulated using the SSP5-8.5 high-end impact scenario (Haarsma et al. 2016). Theses CMIP6 models were chosen due to their accessibility and available data on certain height levels, necessary to calculate our CAT indices. These models cannot resolve the thin vertical depth (1 km) of a patch of turbulence in the atmosphere. Therefore, this study focuses on the horizontal grid spacings across the GCMs (Table 3.1).

Twenty-one indices are used to represent CAT in the upper-atmosphere. These indices, first collated by Williams and Joshi (2013), have been used in previous literature to represent turbulent flow and instability, and the usage of 21 indices ensure the results are as robust as possible. Using an ensemble of these diagnostics permits diagnostic uncertainty quantification. Each index is listed in the appendix. The assumption that energy cascades from larger scales into smaller eddies is made with many NWP models and on average, is an appropriate representation of the spatial structure of atmospheric turbulence (Koch et al. 2005), and is so applied within this study. Each index represents different mechanisms for turbulent air flow. For example, an anticyclonically curved jet stream and the CAT associated with it, could be well represented by the vorticity advection index in combination with the magnitude of vertical wind shear. The Brown index, which is a combination of absolute vorticity and flow deformation, does not perform well in a strongly anticyclonic system because it does not efficiently distinguish between anticyclonic or cyclonic flow (Knox 1997). The frontogenesis function, an index related to the amplification of inertia-gravity waves during frontogenesis and their breakdown (Lane et al. 2004), also does not perform well in anticyclonic flow (Knox 1997), but well in cyclonical bent jet streams. The commonly used CAT forecasting Graphical Turbulence Guidance (GTG) tool is made up from several of our indices. Sharman and Pearson (2017) verified, through receiving operating characteristic curve analysis, that these GTG diagnostics effectively diagnose light-or-greater CAT at high altitudes. This paper takes an ensemble across the twenty-one indices to encapsulate a range of CAT-generated situations.

The cube-rooted eddy dissipation rate (EDR) is a common quantitative measure for atmospheric turbulence, as it is directly proportional to the root mean square vertical acceleration of a plane (MacCready 1964). This paper follows Williams (2017) and assumes certain EDR values relate to the severity of the turbulence encounter and the upper percentile ranges in each index correspond to these dissipation rates. Light, light-to-moderate, moderate, moderate-to- severe, and severe turbulent airflow arises in the 97.0–99.1%, 99.1–99.6%, 99.6–99.8%, 99.8–99.9%, 99.9–100% percentiles of each index, respectively. The cube-rooted EDR values ($m^{2/3}s^{1}$) for the previously defined severities, in succession, are 0.1–0.2, 0.2–0.3, 0.3–0.4, 0.4–0.5, and > 0.5 (Williams 2017). This paper mainly focuses on moderate turbulence encounters, as moderate turbulence is more common than severe turbulence and more hazardous than light turbulence. To quantify a change in time and with climate change, a reference period must be defined. Here we use moderate CAT values between the years 1950–1959 inclusive as a reference to quantify the percentage change in CAT. All seasons are included, within this controlled state. The yearly moderate CAT percentage changes over a 101-year period (1950–2050) are discussed in Sect. 3.3. The North Atlantic basin (50–75$^{\circ}N$, 300–350$^{\circ}E$) is the region of interest. The atmospheric height of analysis is at the typical cruising height of aircraft, 200 hPa.

3.3 Results

Moderate turbulence occurs within an EDR range of 0.3–0.4 $\mathrm{m}^{2/3}$ s^{1}, or within the 99.6–99.8th percentile ranges within each index. The middle (green) boxplots, across fig. 3.1, show the distribution of the 99.6th percentile value for each index between 1950 and 1959 for all GCMs and their sub-models. Indices are abbreviated with full names listed in the fig 3.1 caption. When considering one model, its simulated threshold values are different for each severity. However, if considering multiple models, these values could be related to more than one severity.

FIGURE 3.1: The distribution of 1950–59 EDR-related thresholds displayed for each diagnostic; vertical wind shear of the horizontal wind(WShear; a), Brown energy dissipation rate (BED; b), variant one of Ellrod's index (E1; c), variant two of Ellrod's index (E2; d), negative Richardson number (NegRi; e), horizontal temperature gradient (HTG; f), flow deformation times vertical temperature gradient (FDVTG; g), version 1 of North Carolina State University index (NCSUV1; h), horizontal wind speed (WSpeed; i), wind Speed times directional shear (W_SpeedDS; j), magnitude of horizontal divergence (HorDiv; k), magnitude of residual of non-linear balance equation (ResNLBE; l), vertical vorticity squared (Vortsq; m), relative vorticity advection (RelVortadv; n), magnitude of absolute negative vorticity advection (NegVortadv, o), flow deformation (FD; p), flow deformation times wind speed (FDWSpeed; q), frontogenesis function (FF; r), Brown index (BI; s), potential vorticity (PV; t), Colson-Panofsky index (CP; u). Thresholds created using all ensemble runs, for all submodels within the three GCMs listed in Sect. 2. The distribution of 1950–59 EDR-related thresholds displayed for each diagnostic, continued: There are five CAT severities displayed: light (blue), light to moderate (orange), moderate (green), moderate to severe (grey) and severe (purple). The 25th and 75th percentiles bound the boxes shown, with the vertical black line through each box representing the median data point. The whiskers extend to show the rest of the distribution.

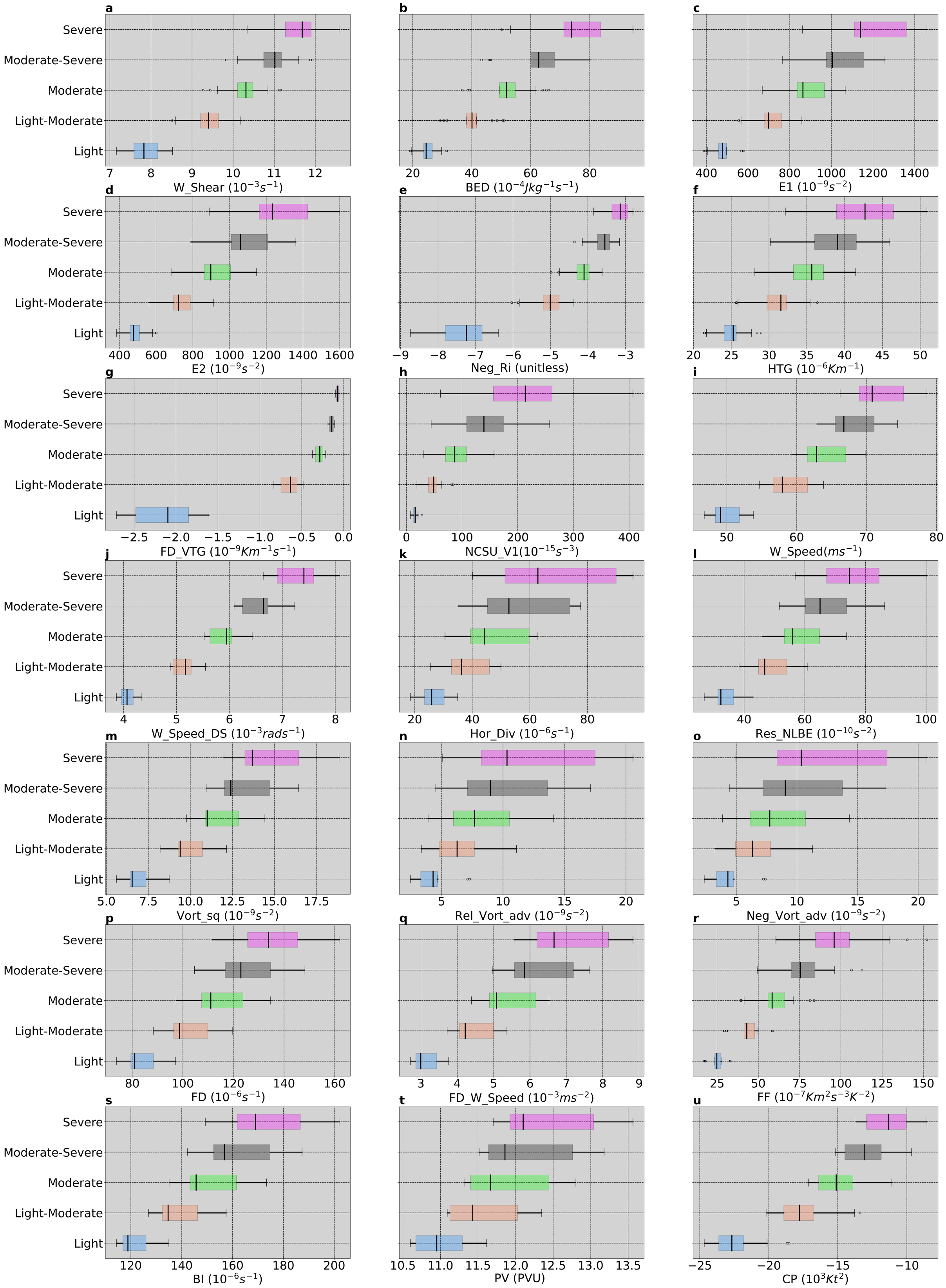
Severe
Moderate-Severe
Moderate
Light-Moderate
Light
a
7 8 9 10 11 12
W_Shear ($10^{-3}s^{-1}$)
b
20 40 60 80
BED ($10^{-4}Jkg^{-1}s^{-1}$)
c
400 600 800 1000 1200 1400
E1 ($10^{-9}s^{-2}$)
d
400 600 800 1000 1200 1400 1600
E2 ($10^{-9}s^{-2}$)
e
−9 −8 −7 −6 −5 −4 −3
Neg_Ri (unitless)
f
20 25 30 35 40 45 50
HTG ($10^{-6}Km^{-1}$)
g
−2.5 −2.0 −1.5 −1.0 −0.5 0.0
FD_VTG ($10^{-9}Km^{-1}s^{-1}$)
h
0 100 200 300 400
NCSU_V1($10^{-15}s^{-3}$)
i
50 60 70 80
W_Speed(ms^{-1})
j
4 5 6 7 8
W_Speed_DS ($10^{-3}rads^{-1}$)
k
20 40 60 80
Hor_Div ($10^{-6}s^{-1}$)
l
40 60 80 100
Res_NLBE ($10^{-10}s^{-2}$)
m
5.0 7.5 10.0 12.5 15.0 17.5
Vort_sq ($10^{-9}s^{-2}$)
n
5 10 15 20
Rel_Vort_adv ($10^{-9}s^{-2}$)
o
5 10 15 20
Neg_Vort_adv ($10^{-9}s^{-2}$)
p
80 100 120 140 160
FD ($10^{-6}s^{-1}$)
q
3 4 5 6 7 8 9
FD_W_Speed ($10^{-3}ms^{-2}$)
r
25 50 75 100 125 150
FF ($10^{-7}Km^2s^{-3}K^{-2}$)
s
120 140 160 180 200
BI ($10^{-6}s^{-1}$)
t
10.5 11.0 11.5 12.0 12.5 13.0 13.5
PV (PVU)
u
−25 −20 −15 −10
CP (10^3Kt^2)

Median lines that reside to the far left of the ranges suggest that one or two outlying sub-models have altered the spread and led to an overlap of box plots within fig 3.1. Interestingly, often if the boxes do not overlap, the whiskers, which represent remaining points above and below 75th and 25th quartiles of the distribution, are overlayed. This is shown in fig.3.1a (vertical wind shear of the horizontal wind), where boxes do not touch but the whiskers do. Vertical wind shear is a diagnostic linked directly with the generation of CAT and is a component in several of the indices. Generally, within fig 3.1, as the CAT severity increases, the medians of the diagnosed threshold values, and their standard deviations, increase. Interestingly, flow deformation multiplied by vertical temperature gradient has a broad range of light values, compared to the other severities (fig 3 1g). This is also apparent for light threshold ranges for negative Richardson number (fig 3.1e), an interesting finding as severe turbulence arises in the upper 99.9th percentile of an index and its thresholds would be more likely to differ than light turbulence. In the rest of this paper, for simplicity, only moderate CAT events are evaluated. Moderate turbulence has a suitable spread of threshold values within fig.3.1 for a robust comparison between GCMs.

3.3.1 CAT variations in time for individual CAT indices

Out of the twenty-one indices, twelve show a definitive overall increase in moderate CAT in time (fig 3.2), despite some interannual variability. This increase is particularly evident in the last few decades of the hundred-year period. These diagnostics are as follows: version 1 of the North Carolina State University index (NCSU: fig 3.2h), wind speed (fig 3.2i), residual of the non-linear balance equation (fig 3.2l), vertical vorticity squared (fig 3.2m), relative vorticity advection (fig 3.2n), negative absolute vorticity advection (fig 3.2o), flow deformation (fig 3.2p), flow deformation multiplied by wind speed (fig 3.2q), frontogenesis function (fig 3.2r), Brown's index (fig 3.2s), potential vorticity (PV; fig 3.2t) and Colson-Panofsky index (fig 3.2u). PV has a few anomalously large peaks above +1000%. This is only for EC-Earth-3P (71 km) models in the years 2012 and 2050. Wind speed multiplied by directional shear (fig 3.2j) and magnitude of horizontal divergence (fig 3.2k) both had 6 out of 7 sub-models projecting an increase in CAT. It can be extrapolated that on average, across the model resolutions, fourteen indices project an increase in CAT between 1950 and 2050. Interestingly, relative vorticity advection (fig 3.2q), negative absolute vorticity advection (fig 3.2r), and Brown index (fig 3.2s) project their greatest increase in CAT within coarser models of each sub-model, particularly EC-Earth-3P (71 km) and HadGEM3-GC3.1-LL (135 km). Here we use the term "coarser" to refer to models with horizontal grid spacing $\geq$ 60 km.

Variant one of Ellrod's index (T1; fig 3. 2c), which is a combination of flow deformation and wind shear (Ellrod and Knapp 1992), has one model (HadGEM3-GC3.1- MM) projecting no change to CAT. All other sub models project T1 decreasing in time. Vertical wind shear of the horizontal wind (fig 3. 2a), Brown energy dissipation rate (fig 3. 2b), variant two of Ellrod's index (fig 3. 2d), negative Richardson number (fig 3. 2e) and horizontal temperature gradient (fig 3. 2f) also project a decline in moderate CAT but for all GCMs. CAT develops in regions of increased vertical wind shear instability, yet horizontal wind shear ends the period with a decrease in the number of moderate CAT events from the 1950 threshold period (fig 3. 2d). Projected wind speed related CAT events at 200 hPa are expected to rise in this period, with maximums of +400% (fig 3. 2i). Wind speeds across neighbouring atmospheric heights may increase at a similar or larger rate, decreasing wind shear values. Atrill et al. (2021) also project a decline in wind shear over polar regions and determined the same explanation, but the annual mean wind shear is increasing over the North Atlantic Ocean in time, as found by Lee et al. (2019). Flow deformation multiplied by vertical temperature gradient interestingly had three models projecting a rise in moderate CAT and four simulating a decline. The three sub-models projecting an increase are MPI-ESM1-2-HR, EC-Earth-3P and HadGEM3-GC3.1-LL. These are all the coarsest sub-models within their respective GCMs.

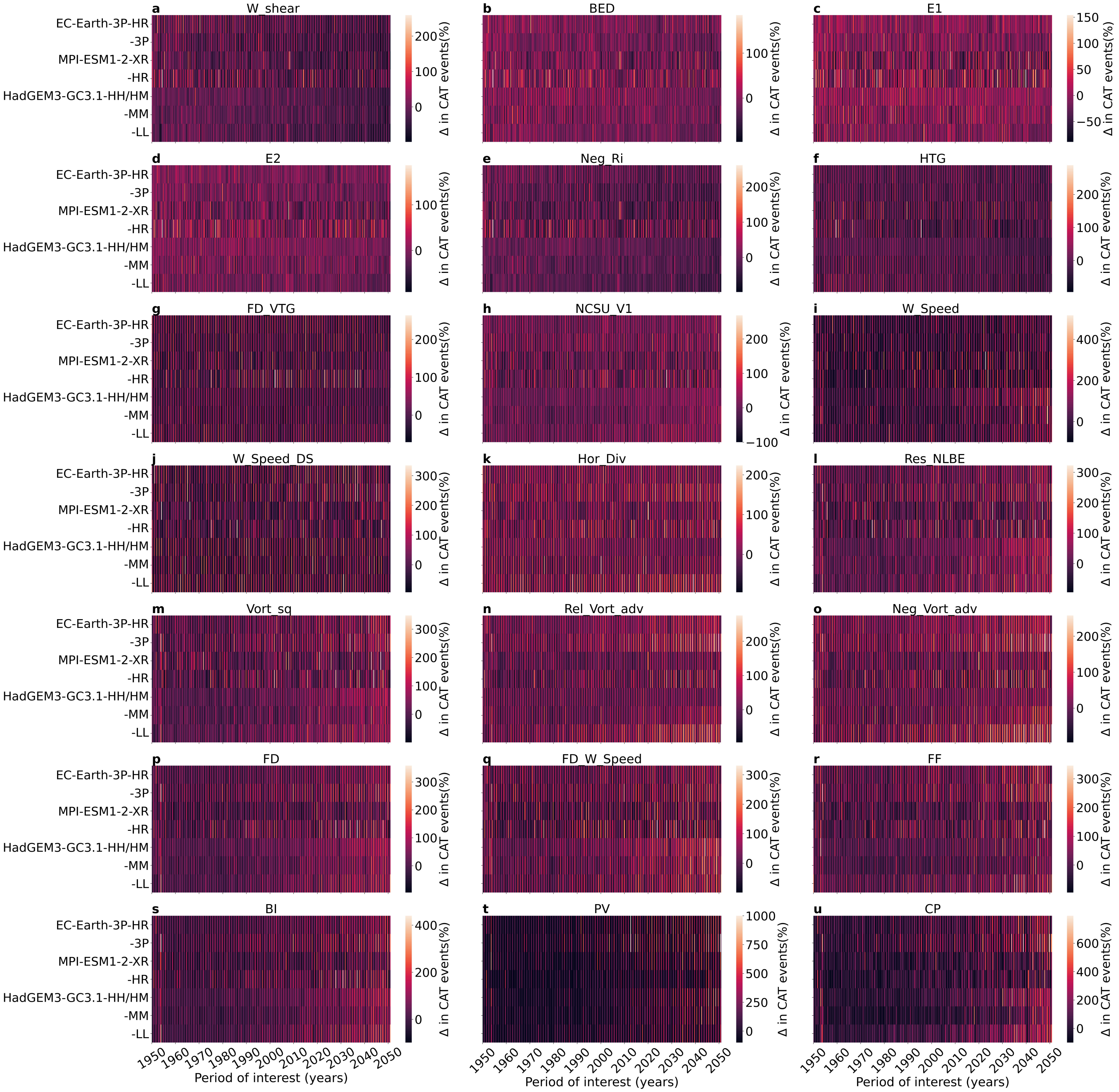

FIGURE 3.2: The projected change in moderate CAT encounters from the threshold values for twenty-one indices that represent CAT across time. The percentage change in time for the three chosen CMIP6 GCMs is also shown, with each sub model included. Findings are averaged across each ensemble member (if applicable). The range of percentage change, shown through colour bars within the subplots, differ and increase from a to u

Due to all indices being closely linked and not physically independent, it is difficult to group them. One could look at the building components and group diagnostics in terms of having a vertical derivative or not. There is an almost even split across the indices, with ten and eleven diagnostics linked with either vertical and horizontal or just horizontal derivatives. Overall, there is a mixture of indices projected to increase and decrease in time in both categories. However, when including wind speed times directional shear (fig 3. 2j) and magnitude of horizontal divergence (fig 3. 2k) increasing in time, 82% of horizontal-only derivative related diagnostics project increases in CAT. There is a half-half mix within the vertical derivatives category (including T1).

3.3.2 North Atlantic seasonal CAT projections

Within this section, fig 3. 3 displays the yearly percentage changes for each season, using the 1950s decade and all seasons within this period as a reference to investigate the seasonality of CAT. Fig 3.4 shows the same information, but with the reference period now being for each season separately rather than all seasons, so that all lines oscillate around zero in the 1950s by definition. EC-Earth and HadGEM3-GC3.1 models project an increase in winter moderate CAT in time over the North Atlantic. After the year 2030 in fig 3. 3, HadGEM3-GC3.1 sub models project 100% more moderate DJF CAT events than the reference period. Despite the coarsest HadGEM3-GC3.1 model (-LL: 135 km) suggesting a dip after 2040 to + 50%, there are only marginal differences between each HadGEM3-GC3.1 submodel for DJF in time.

However, within fig 3. 4, when compared to its individual 1950s reference, DJF is not increasing at the fastest rate over the period. Due to the independence of the variables and normality within the distribution, fig 3. 4 meets the assumption for linear regression analysis and slopes (trends in time) are discussed. The slopes representing DJF are second steepest in three models, third steepest in two models and smallest in two models (EC-Earth-3P,HadGEM3-GC3.1-MM; fig 3. 4b, f). Wintertime over the North Atlantic is historically a period of increased upper-level instability with the greatest risk of moderate turbulence, due to the strengthening of the meridional temperature gradient. Despite strong model agreement projecting an increase in moderate DJF CAT event, other seasons could increase at a greater rate.

The moderate CAT frequency in summer is also projected to rise at the end of the 101-year period, as shown in HadGEM3-GC3.1 and EC-Earth-3 subplots within fig 3. 3. JJA lines reside initially on or below 0% through out fig 3. 3 from 1950 to 2000 but shift positively and reach around + 25% (HadGEM3-GC3.1) and + 35% (EC-Earth-3) by 2020. JJA lines fluctuate at the end of the period at a similar range to DJF/SON at the beginning of the 101-years. This could imply that current and

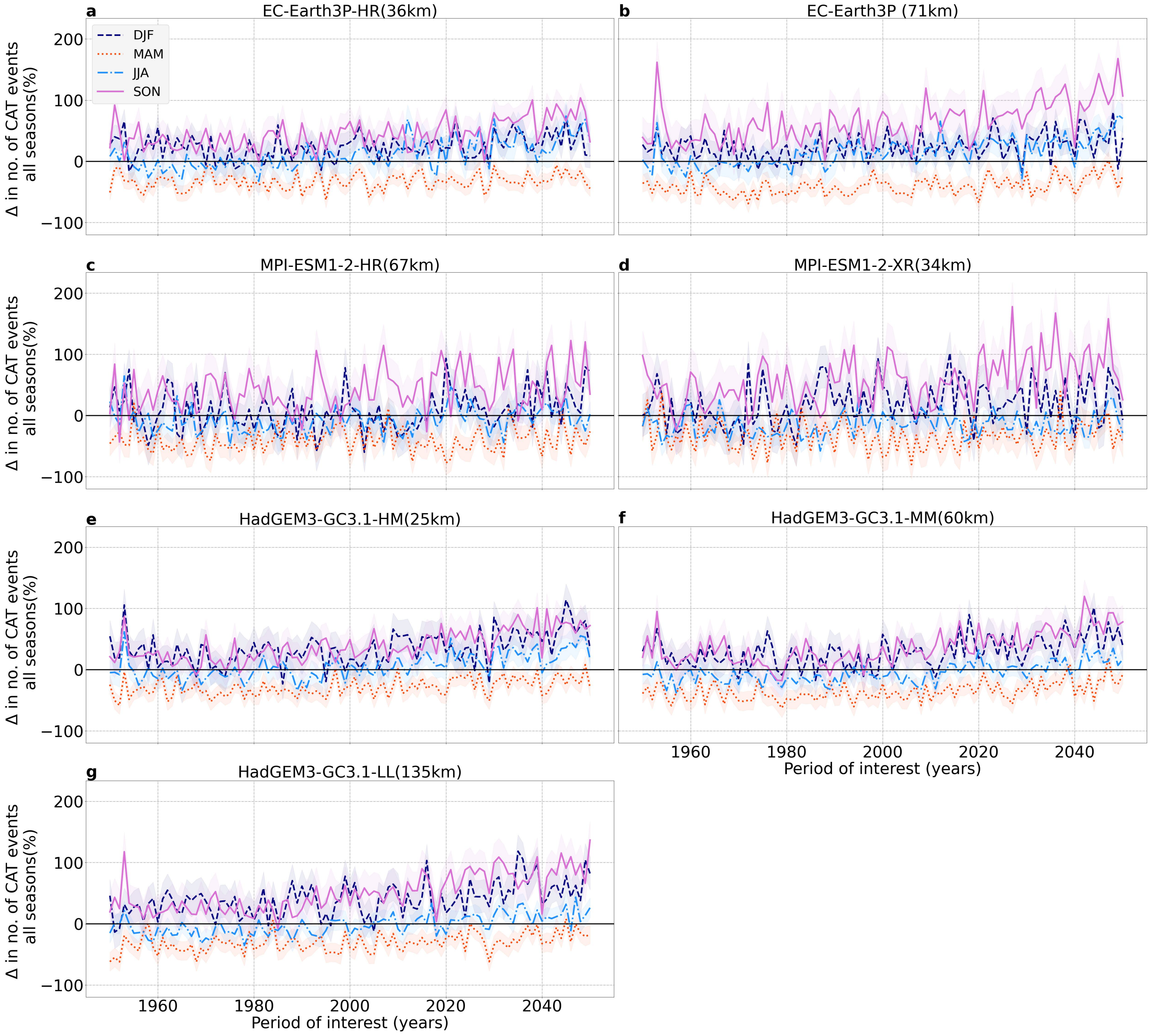

FIGURE 3.3: Seasonal percentage changes in CAT, from the 1950 to 1959 threshold period that includes all seasons, against time (averaged across ensemble members). Season defined by a differing colour and line style, with northern hemisphere (NH) Winter (December–January– February; DJF), autumn (September–October–November; SON), summer (June–July–August; JJA) and spring (March–April–May; MAM) coloured navy blue and dashed, pink and solid, light blue and dash dotted, and orange and dotted, respectively. Population standard deviation error shaded

future JJA turbulence encounters have increased to the same original rate that DJF and SON had in the 1950s. Future CAT encounters in summer could become as common as the 1950s' most turbulent seasons. This rapid change in JJA is evident in fig 3. 4. In fact, the two EC-Earth-3P sub-models within fig 3.4a, b project a significant increase in summer moderate CAT in time over the North Atlantic, at a greater rate in time than comparative seasons within the figure. These EC-Earth JJA rates peak at maximums of + 69.18% (3P-HR, fig 3. 3a) in 2035 and + 76.13% (3P, fig 3.4b) in 2048. The coarser HadGEM3- GC3.1 models, MM (60 km) and LL (135KM) also project a significant JJA increase with similar trend of 0.37%/year and 0.38%/year (fig 3.3f, g).

MPI-ESM1-2-XR, -HR and HadGEM3-GC3.1-HM/HH (fig 3.4c–e) project a smaller percentage change in time for JJA moderate turbulent events, with slopes of 0.12 and 0.13 %/ year. The MPI-ESM1-2 results (Figs. 3d, e and 4d, e) generally have no significant trends in time for DJF, MAM, or JJA and have a significant amount of inter-annual variability. This model does, however, project an obvious increase in CAT for northern hemisphere autumn (SON). There is strong multi-model agreement that CAT events in SON will increase at a rapid rate in time. After 2020 and 2040 in fig 3. 3, MPI-ESM1-2-HR (67 km) and EC-Earth-3P (71 km) project a sharp increase in the number of SON CAT events, reaching maximums of + 150%. Finer-resolution counter parts of MPI-ESM1-2 and HadGEM3-GC3.1 project an increase, but not at the same rate. Within fig 3. 4, the greatest increase is simulated within the Max-Planck coarser sub-model (67 km, fig 3. 4d) at + 105.19% in 2027. Averaging across sub-models, MPI-ESM1-2, EC-Earth and HadGEM3-GC3.1 simulate maximums of + 95.72%, + 62.69% and + 71.96% near the end of the 101-year period. Both Max-Planck and Met Office Centre Hadley sub-models project their greatest increase in CAT within NH autumn.

Spring over the North Atlantic is a season with characteristically the fewest moderate CAT events. When including all seasons in the 1950–59 reference, the MAM lines reside below zero (fig 3. 3). This suggests that the number of DJF and SON projected moderate CAT events in the 1950s is greater than the number of MAM CAT events throughout the 101-year period. However, there is an increase displayed in the HadGEM3-GC3.1 MAM lines within fig 3. 4, with one sub model projecting a greater increase than DJF at 0.35%/ year (fig 3. 4f). Despite this increase, MAM is quite variable across GCMs and sub-models, for example MPI-ESM1- 2-HR projects a negative slope in time (fig 3. 4d). Therefore, further seasonal analysis is needed.

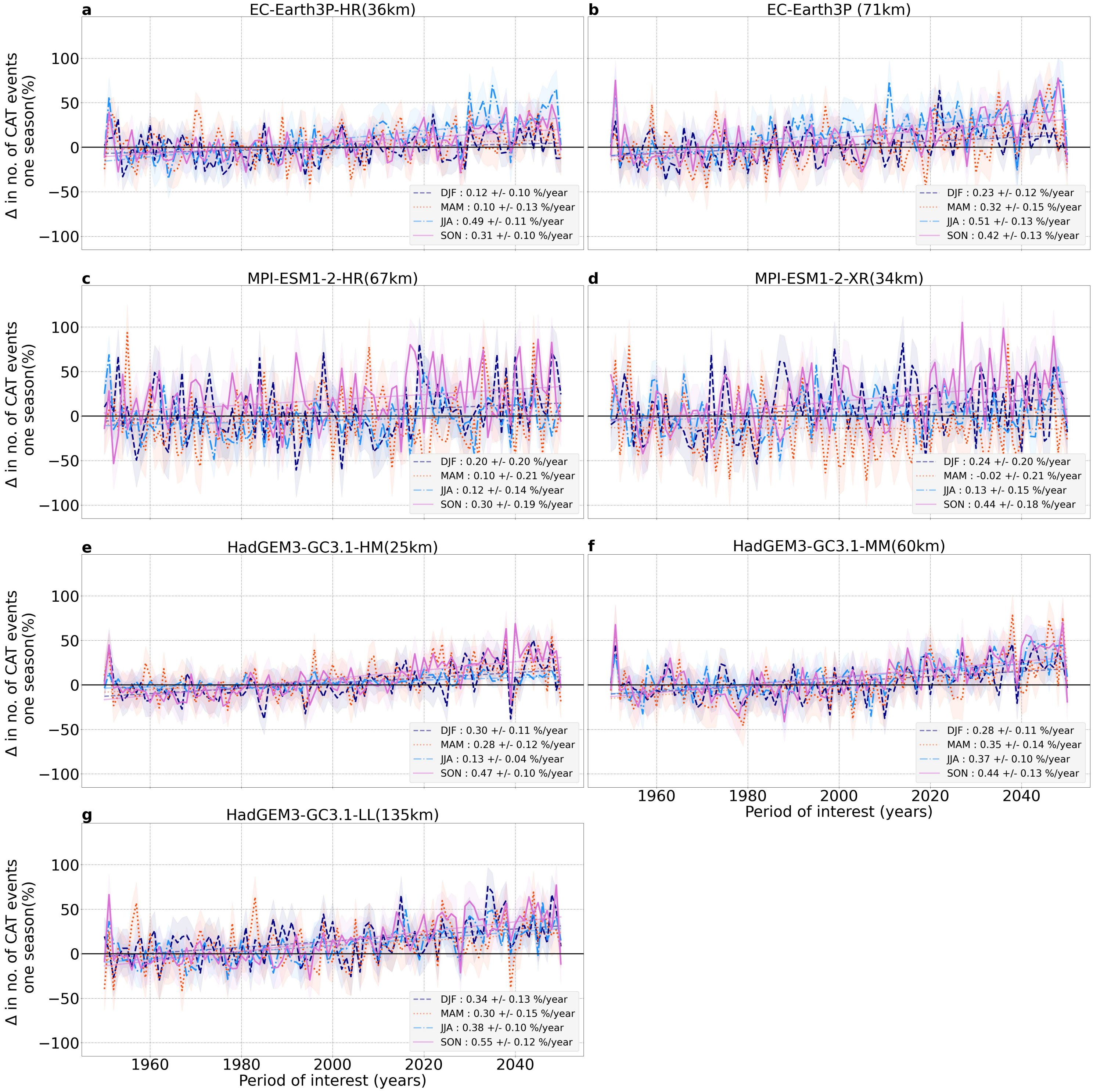

FIGURE 3.4: Seasonal percentage changes in CAT, from the 1950 to 1959 threshold period that includes just one season, against time (averaged across ensemble members). Season defined by a differing colour and line style as done in figure. 3.3

3.3.3 Moderate CAT variations with global near surface temperature

Thus far, section 3.3 has concentrated on the change in CAT with time. To isolate the relationship between global surface warming and upper-atmospheric CAT over the North Atlantic, the warming trend in each model is considered. The mean near-surface (2m height) global temperatures in time are displayed in fig 3. 5. As anticipated, these temperatures increase with time for all GCMs across all seasons. The SSP high-end projections modelled within the CMIP6 GCMs relate this warming to anthropogenic sources. All ensemble members, if applicable, have been included in fig 3. 5. MAM and SON have a very similar warming trend in time, across all climate models. This relates to the equal and opposite seasonal differences between the northern and southern hemispheres. One may have assumed DJF and JJA to have the same global average in surface air temperature, like MAM and SON, but they differ due to differences in land mass between the hemispheres and the larger oceans to land heat capacity.

HadGEM3-GC3.1 has the largest sample size available with 11 ensemble members over the sub models against only 6 other GCM members. HADGEM3-GC3.1 models have coldest start of the period, relative to the other GCMs. This is most apparent for ensemble member number 4 within HadGEM3-GC3.1-LL model runs, with a large change in DJF near-surface air temperatures (TAS) of 4.05 °C between 1950 and 2050. MPI-ESM1-2 and EC-Earth-3 models project a similar and interchangeable increase in global temperature change. Within MPI-ESM1-2, the finer -XR sub model is overall colder than the HR model, particularly in the beginning of the period. This new generation of CMIP models has a higher climate sensitivity than previous CMIP5 generations (Harvey et al. 2020). This spread of future temperature could be linked to this heightened sensitivity. Sensitivity is defined here as an outcome that arises from the physical and dynamical chaos within climate models, and something that is not directly developed by a climate modeller. This may be one explanation as to why different ensemble runs, within the same sub model, reach temperatures at different stages in time within fig 3. 5. The change in TAS for each year from 1950 is analysed in later figures, to better compare the warming trend with CAT in each sub-model and to consider the inter-annual TAS variability.

Figure 6 outlines the relationships between moderate CAT percentage change (fig 3. 4) and the change in global mean seasonal TAS. The slopes of regression are a form of analysis used to determine a trend within TAS. There is good internal agreement across the HadGEM3-GC3.1 (fig 3. 6e–g) models for DJF with projected CAT increasing by 8.67–9.74%/°C. The Met Office Hadley Centre mid-resolution (60 km) sub model (HadGEM3-GC3.1-MM) projects NH spring values to increase by 11.69% per degree. This is the second fastest rate after NH autumn within fig 3. 6f, placing DJF with the lowest increase. Despite EC-Earth- 3P (71 km) projecting a similar increase of 11.89%/°C for MAM, the remaining sub-models within MPI-ESM1-2 and EC-Earth project an insignificant increase with TAS.

There is an apparent model grid dependence for SON projections. Across all GCMs, the coarser sub-model versions project the maximum SON percentage changes, by a difference of 2%/°C for HadGEM3-GC3.1 and EC-Earth-3 models and by 6% between MPI-ESM1-2 rates. EC-Earth3P (71 km) and HadGEM3-GC3.1-LL (135 km) simulate increases of 14.53%/°C and 14.74%/°C, respectively. MPI- ESM1-2-HR simulated the largest projected SON rate of 19.14%/°C. However, the confidence of this trend is combatted by a large interval of ± 7.97%/°C. MPI-ESM1-2's results have a large spectrum of uncertainty with relatively large confidence interval ranges. This could, however, be related to the ensemble size of MPI-ESM1. NH Summer projections vary across fig 3. 6, from HadGEM3-GC3.1 modelled data suggesting an increase at a similar or just below SON. MPI-ESM1-2 projected an increase in JJA by 6.75%/degree on average and EC-Earth-3P simulate respectively large JJA trends, projecting + 20.64%/°C and + 18.75%/°C for EC-Earth-3P-HR (36 km) and -3P (71 km). EC-Earth-3P-HR projects larger increase for summer-time moderate CAT per degree than any other season or model. This suggests a rapid increase in the number of CAT events for summer, which is a season that has historically not been as comparably turbulent.

3.3.4 Averaged trends with anthropogenic climate changes

To reduce uncertainty that arose from averaging over ensemble members, fig 3. 7 displays fig 3. 6's regression line slopes, with confidence intervals for all ensemble members. Within fig 3. 7, the boxes are colour coded in terms of resolution range. Autumn across the North Atlantic is projected to have a large increase per degree of surface warming. SON's slopes (fig 3. 7c) range from 10.78 to 15.24, 13.21 to 19.14, and 10.45 to 17.37%/°C for the EC-Earth-3P, MPI-ESM-2, and HadGEM3-GC3.1 ensembles, respectively. Each square, representing an individual ensemble member's slope, displayed within fig 3. 7c propagates closely to the median line. This is also visible for DJF trends (fig 3. 7a). DJF's slopes has few multi-model disagreements, with HadGEM3-GC3.1, MPI-ESM1-2, and EC-Earth-3 on average increasing by 9.10 ± 1.83, 9.73 ± 6.26, and 7.56 ± 2.86 % per degree.

This strong model agreement is not apparent within NH summer projections, with JJA on average increasing by 12.41 ± 1.39%/°C, 6.71 ± 4.76%/°C and 21.18 ± 3.02%/C for HadGEM3-GC3.1, MPI-ESM1-2 and EC-Earth-3 models. This wide variability is evident across GCMs but is not the case internally, with ensemble members residing usually in similar brackets. For example, all EC- Earth-3 ensemble member JJA results lie above the median line, ranging from 15.70 to 22.53%/C.

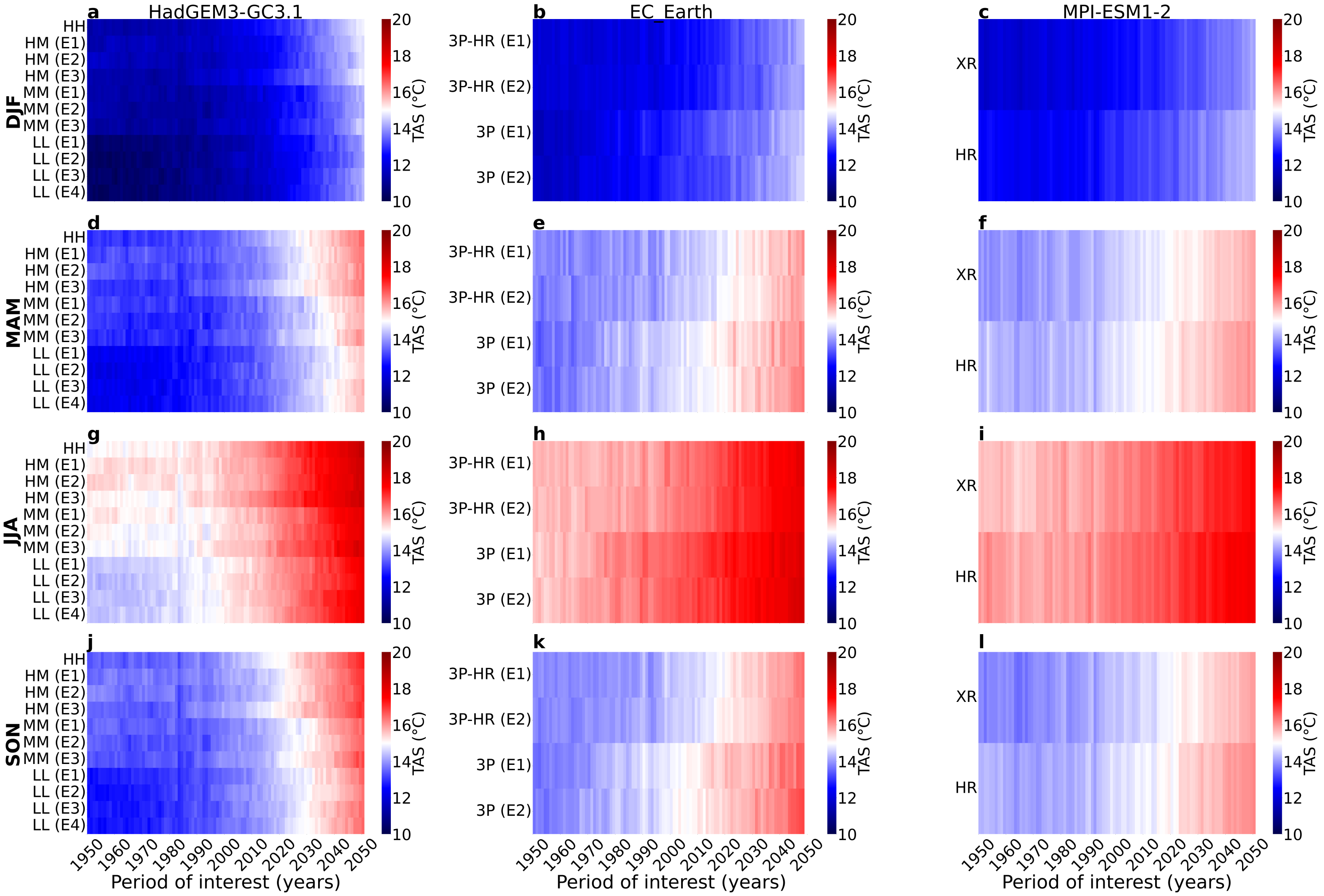

FIGURE 3.5: The global mean seasonal near surface temperatures (TAS) projected over time for each chosen CMIP6 global climate model. All sub models and ensemble members are included. Global mean TAS for HadGEM-GC3 DJF, MAM, JJA and SON are displayed in subplots a, d, g and j. For EC-Earth the same retrospective seasons are shown in subplots b, e, h, and k and MPI-ESM1.2 are shown in subplots c, f, i and l

Interestingly, NH summer is projected to increase in the number of moderate CAT events at a similar (or greater) rate than NH Autumn. NH spring over the North Atlantic has a wide spread of moderate CAT projections. On average EC- Earth-3 and HadGEM3-GC3.1 MAM slopes are increasing at a similar rate with median values of 9.64 ± 4.75 and 8.89 ± 3.31%/°C, but there is a considerable spread of 0.07 to 13.21 and 2.37 to 23.90%/°C, respectively. HadGEM3- GC3.1-MM ensemble 1 projects the greatest increase in moderate CAT per degree for NH spring (23.90%/°C). However, this comes with a high slope uncertainty of ± 8.87%/°C. Ensemble 2 of this Met Office Hadley Centre model projects an increase of only 5.77 ± 7.40%/°C. To complete these large uncertainties associated with NH spring, MPI-ESM1-2 has the smallest average increase of + 2.50 ± 7.1%/°C.

There is at least one ensemble member for each of the GCMs that projects a minimal change per degree in spring. This adds weight to a MAM future scenario with negligible moderate CAT increases. However, there are many projections with increases similar to DJF. If one takes an ensemble member and multi-model average across these GCMs, MAM is projected to increase by 8.81 ± 1.90%/°C. This quantitative median applied to the other seasons leads to an overall increase in moderate CAT events by 8.94 ± 1.54%/°C,13.82 ± 1.27%/°C, and 13.69 ± 1.28%/°C for DJF, SON, and JJA, respectively. This is not a weighted average, as HadGEM3-GC3.1 makes up 11 of the 17 sampled slopes, so has a larger influence on averages across

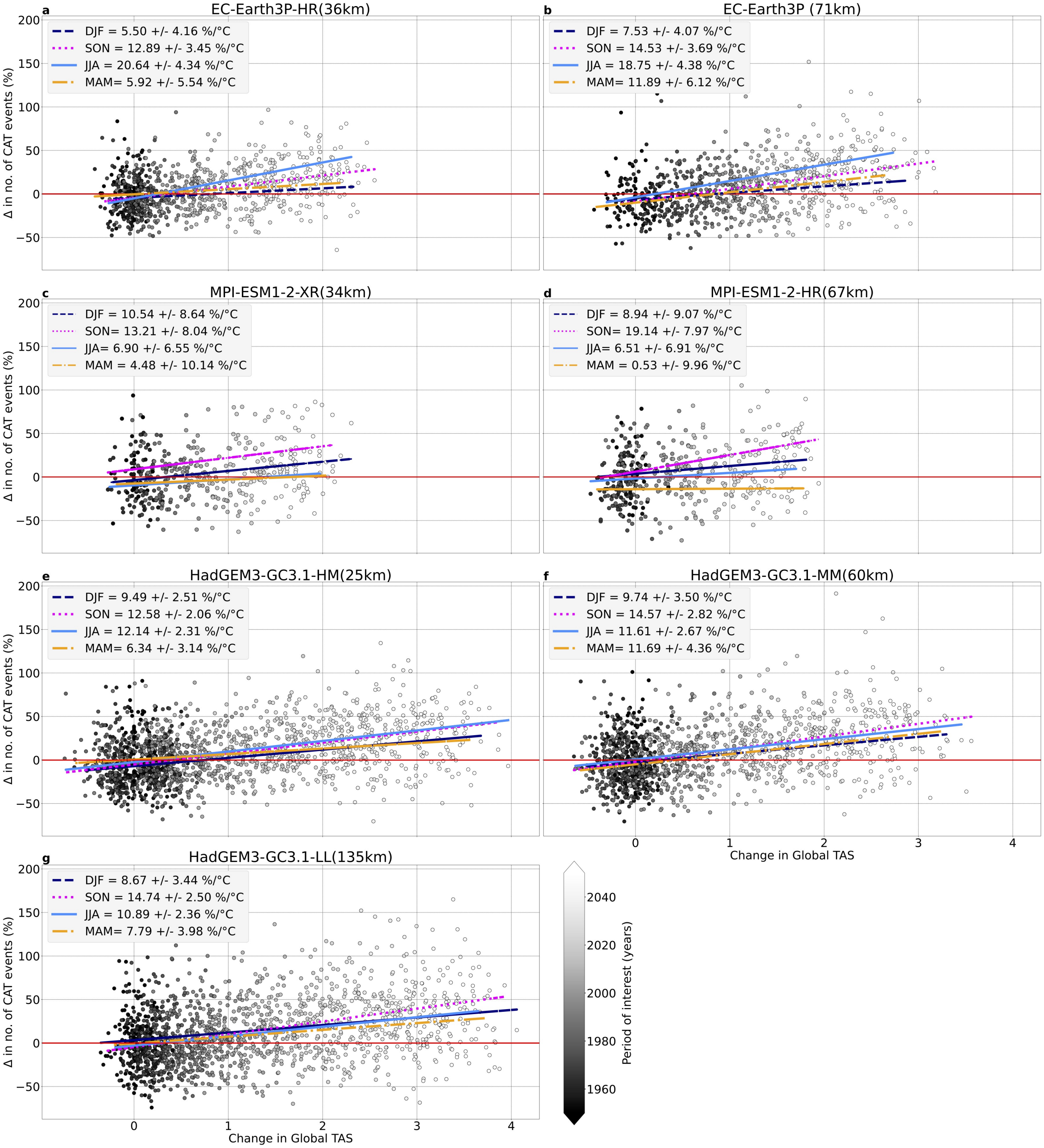

FIGURE 3.6: The moderate percentage change scattered against change in mean global seasonal near surface temperature (TAS). Shade of scatter relates to the year of moderate CAT events. Season defined by colour and line style, with DJF, SON, JJA, and MAM coloured blue and dashed,pink and dotted, light blue and solid, and orange and dash dotted, respectively. The line of regression slopes, with 95% confidence intervals, take an average over ensemble members

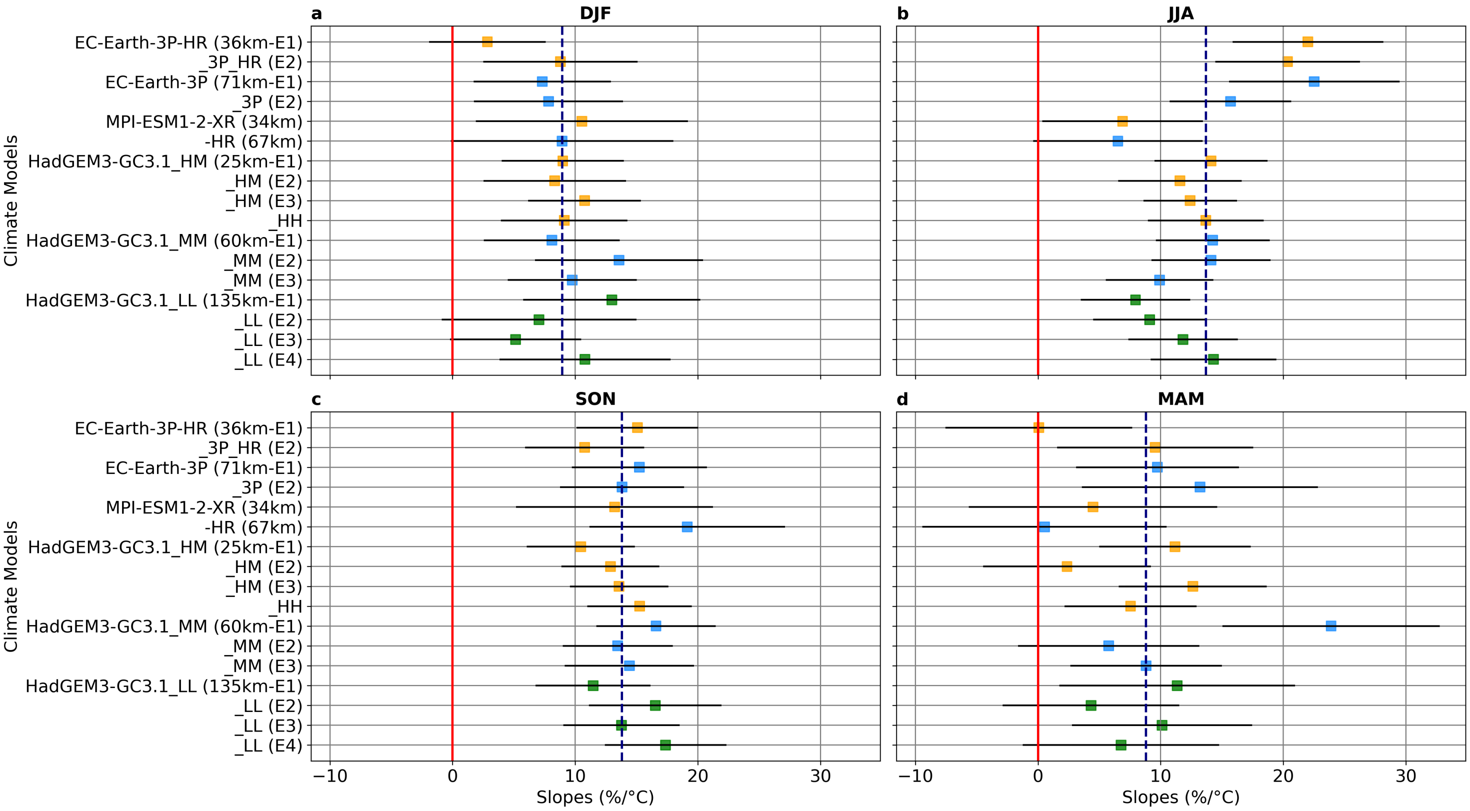

FIGURE 3.7: Regression line slopes showing the trend between moderate CAT percentage changes over the North Atlantic, against the global mean seasonal near-surface temperature for all ensemble members within HadGEM3-GC3.1, EC-Earth-3P, and MPI-ESM1-2. The colour of the square represents the range of which the sub-model's horizontal resolution resides within, with 25–36 km shaded orange, 60–71 km shaded blue, and 135 km shaded green. The navy dashed line is the average (median) across all squares for each season, with subplot a, b, c, and d displaying slopes from DJF, JJA, SON, and MAM.

GCMs.

3.4 Summary and discussion

This paper has explored the projected moderate CAT changes with anthropogenic climate change using a sample of CMIP6 HighResMIP GCMs. This publication uses three models, the Met-Office Hadley Centre model HadGEM3- GC3.1, the Max-Planck Institute model MPI-ESM1-2, and from a collaboration of European universities and organisations, the EC-Earth-3 model. All model simulations cover the period 1950 to 2050 and follow the CMIP6 HighResMIP protocol. There are several different resolutions across these GCMs, and so a multi-model approach was applied to understand the dependency of CAT projections on model resolution. CAT changes in the North Atlantic in northern hemisphere winter (DJF), summer (JJA), autumn (SON), and spring (MAM) are individually analysed from Figs. 3, 4, 6 and 7. Twenty-one indices are used to represent the different dynamical scenarios for CAT production. There were variations in the results for the different indices and climate models. Most diagnostics displayed an increase in moderate CAT from 1950 to 2050. The greatest projected increase arose in the last 30–40 years of the period of interest. For three indices, the sub-models with coarser resolutions (grid lengths 60 km) simulated the maximum increases in moderate CAT.

HadGEM3-GC3.1 and EC-Earth-3 models projected an increase in wintertime CAT across the 101-year period, with large interannual fluctuations after 2030. These models also simulated an increase in CAT with time for all seasons. In contrast, the MPI-ESM1-2 changes had no significant trends for DJF, MAM, or JJA in time. However, there was strong multi-model agreement that CAT events in SON will increase at a fast rate in time, compared to other seasons. The greatest seasonal increase for SON was projected in MPI-ESM1-2-HR by +105% in late 2020 (fig 3. 4d). The number of CAT events in summer is also projected to rise at the end of the 101-year period, as shown in the HadGEM3- GC3.1 and EC-Earth-3 subplots within Figs. 3 and 4. This implies current and future JJA turbulence encounters may have increased to the same original rate DJF and SON had in the 1950s.

Overall, no dependence on model horizontal resolution was found after averaging across the indices for DJF, JJA and MAM. Global seasonal-mean near-surface temperature was used as the metric of global warming in each model, allowing the expression of projected CAT changes per degree of global warming. Within SON results, and individual diagnostics, coarser sub-models generally produce greater increases in time and with near-surface warming. We speculate that perhaps the move to high resolution climate models may result in projections of increased SON CAT being revised downward slightly. Autumn, over the North Atlantic, had good multi-model agreement on future CAT projections, with all GCMs agreeing an increase between around 10 and 20%/°C, with a median percentage increase of 13.82 ± 1.27%/°C. A high multi-model agreement also arose for DJF CAT changes. Wintertime CAT on average will increase by 8.94 ± 1.54%/°C. This differs from JJA slopes, which had a considerable spread across the GCMs. NH summer CAT projections, over the North Atlantic, on average suggest an increase of 13.69 ± 1.28%/°C, a similar average to NH autumn results. However, on average for each GCM, JJA is projected to increase in the number of CAT encounters by 21.18 ± 3.02%/°C, 12.41 ± 1.39%/°C and 6.71 ± 4.76%/°C for EC-Earth-3, HadGEM3-GC3.1 and MPI-ESM1-2. Despite CAT previously not being commonly encountered in NH spring, both HadGEM3-GC3.1 and EC- Earth-3 models projected a significant increase time and with global warming. On average, across all models, MAM had an increase in the number of moderate CAT events by 8.81 ± 1.90% per degree of global seasonal near-surface warming. This rate is similar to that found for the most turbulent season DJF. In summary, this multi-model analysis found that moderate CAT will increase in future over the North Atlantic, for all seasons. This will have consequences for to the aviation industry, with more flights disrupted and increased damages and costs. Future work should quantify how this overall increase will impact aircraft directly and if the increase found over the North Atlantic in this study is linked to a higher density of CAT outbreaks in particular regions.

Chapter 4

Evaluation of clear air turbulence patches in high-resolution global climate models

Abstract

Clear Air Turbulence (CAT) is a type of upper-level atmospheric turbulence that has a dangerous and costly impact on the aviation sector. Aircraft encounter patches of CAT which are approximately 60-70km in width, but vertically thin at 1km. Previous literature has found that CAT has increased globally, and is projected to continue increasing in the future. Previous work has mainly focused on the overall percentage change in CAT. To understand what this physically equates

to in terms of the patch variation, this paper aims to understand how an increase in CAT is related to the number and properties of CAT patches. Using a range of global climate models (GCMs), with some capable of resolving an average patch size, this investigation focused on two mid-to high latitude bands over the northern hemisphere (NH) and southern hemisphere (SH). Projections display an increase in the total amount of CAT (km^2) within the atmosphere for winter, autumn and spring in both hemispheres. There is large model disagreement on the trend for summer-time CAT. On average a decline in the amount of CAT is seen in summer, with the SH area reducing in summer-time CAT by -105.35 +/- 35.33 km^2 per year. Winter-time CAT over the NH and SH areas increased on average by +360.16 +/- 48.10 km^2 and +474.13 +/- 43.72 km^2 per year. This winter-time trend occurs due to an increase in both the average patch size and the number of patches, with a rise of +1.32 +/- 0.42 km^2 and 0.05+/- 0.007 patches per year and 0.89 +/- 0.31 km^2 and 0.07 +/- 0.007 patches per year for the NH and SH area, respectively. In comparison to the NH winter, SH JJA displays a greater increase in the total amount of CAT by an extra 11,511 km^2 by 2050 and with two more extra patches of CAT compared to NH. For NH spring and SH autumn general increases in CAT projections were found to be developing due to an increase in the number of patches, whereas NH autumn and SH spring involved an increase in both size and number.

4.1 Introduction

Aircraft often encounter patches of atmospheric turbulence throughout their flight from take off, cruising, to landing. These encounters have negative impacts on the aviation sector, accounting for 71% of all in flight injuries (Hu et al. 2021) and around 30 medical claims a day (Ellrod and Knapp, 1992). These situations can exacerbate the fear of flying into the general public (Aerophobia) (Sharman et al., 2014). An extensive study, from the Boeing Corporation, found that 17% of the population in the United States will answer 'yes" to having Aerophobia. This study found this fear equated to a 9% loss in customers and US$1.6 billion loss in revenue for the US airline in the 1982 economy (Oakes et al., 2010). There are other economic issues on the sector, with turbulence having an impact on the structural integrity of the craft, leading to increased repairs, time lost in inspection and maintenance, and the impact of delays and fuel consumption during a turbulent flight (Sharman et al., 2014, Tebaldi et al., 2002).

Clear air turbulence (CAT) is a type of upper-level atmospheric turbulence that impacts aircraft at typical cruising heights. At this upper level, the flight is in a segment were passengers and crew members are more likely not to be wearing their seat belts (Kim et al., 2018). CAT develops within regions of increased shear and Kelvin Helmholtz instability (KHI), in atmospheric conditions that have no convective cloud features. Despite flight paths being designed to avoid regions of CAT as much as possible, with forecasts determining regions of turbulence with an accuracy of 75-80% (Wolff and Sharman, 2008), aircraft can suddenly encounter CAT without warning. CAT lacks water droplets, and is therefore not detectable by on-board radar equipment.

Over the North Atlantic area, Williams (2017) assumes that 2.1% of the region has light CAT occurring within it. As CAT severity increases, the likelihood of encountering CAT decreases, for example only 0.1% of the area is associated with severe CAT. Severe, or extreme, CAT is very rare. An aircraft's response to encountering such severity would be fast, abrupt altitude shifts with the craft violently tossed around, and a loss of control likely (Sharman and Lane, 2019). These encounters can have an impact on the structure of a plane, with repeated turbulence encounters leading to metal fatigue and in very rare cases structural failure (Ellrod et al., 2015).

There are several conditions deemed favourable for CAT development in the atmosphere. The majority are found in areas of increased KHI, near jet streams or upper-level fronts, with 2 out of 3 CAT events located around a jet (Ellrod et al., 2015). The eddy-driven jet stream, that owes its existence to both meridional and horizontal temperature gradients, flows around the globe in the mid to high latitudes of the Northern and Southern hemispheres (NH/SH). Due to this dependence on temperature gradients, there are seasonal difference to the flow, with a weaker meridional temperature gradient in the summer associated with a slower jet stream. Winter in both hemispheres is linked to stronger, faster jet with an increase in shear and KHI. Theoretically, the NH summer mean zonal jet flow should be half that of NH winter flow (Holton and Hakim, 2013; Sharman and Lane, 2019). Interestingly, due to the large fraction of the ocean, compared to land, within the SH, SH winter and summer have less variation in jet strength, compared to NH. CAT can also arise within sub-tropical jet streams, which are situated at 30°N/S at the upper troposphere, where the Hadley and Ferrell cell converge.

There is evidence that CAT frequency has increased globally with ECMWF (European Center for Medium Weather Forecasting) ERA5 re-analysis data showing definitive trends over the last 40/41 years (Prosser et, al, 2023, Lee et al. 2023). These trends have been attributed to global troposheric warming, strengthening temperature gradients, leading to faster, more chaotic jet streams. Two areas of the globe with large increase were the North Atlantic, with severe or greater CAT increasing by +49%, +52%, +85% and +47% within NH winter, summer, spring and autumn, (Prosser et al., 2023) and over East Asia with a positive trend between 0.048 to 0.054% per year (Lee et al., 2023). Over East Asia, Hu et, al, (2021) projected CAT to increase in frequency in a high end emissions Representative

Concentration Pathway scenario (RCP5-8.5) by +6.9% for encounters with a light severity, +12% for moderate and +15% for severe events. This publication used global climate models (GCMs) and re-analysis data to diagnose CAT. GCM's representation of CAT, when compared to re-analysis data, has been shown to portray an effective dynamical response of the atmosphere, in regards to turbulence (Williams and Storer, 2022). Several studies apply GCM data to effectively understand future changes to CAT. For example, Storer et al. (2017) projected a increase in severe turbulence by +62% in South America, +160.7% over Europe, +181.4% over the North Atlantic, +91.6 % over the North Pacific, +112.7% over North America and more across the globe, in a future RCP5-8.5 scenario. Coupled Model Inter-comparison Project phase 5 (CMIP5) GCM data was used with Storer. et al.(2017). CMIP5 has now been surpassed by a newer phase referenced as CMIP6. Smith et al. (2023) uses three CMIP6 High-ResMIP (High-resolution inter-comparison project) GCMs to investigated trends over the North Atlantic per degree of global near-surface warming. These three GCMs had a range of resolutions, leading to a seven multi-model investigation that found an overall increase in moderate CAT by +9%, +9%, +14% and +14% in northern hemisphere winter, spring, summer and autumn per degree of warming. All aforementioned papers explore the percentage change to CAT over the last few decades and into the future, but none explore what this entails physically for the patches of turbulence in the atmosphere.

Sharman et al. (2014) conducted an extensive study using 200 aircraft fitted with a software package which automatically estimated and reported on atmospheric turbulence intensity. With the cooperation of two different airlines, the cubed root of eddy (energy) dissipation rates ($EDR^{1/3}$') were collated over a 10 year period at mid-high altitudes, primarily over the Continental United States. The cubed square root of EDR is a quantity used often in aviation turbulence research due to its proportionate relationship to the vertical acceleration of an aircraft. Physically EDR represents the dissipative rate of kinetic energy conversion into heat (Sharman and Lane, 2019). Sharman et al. (2014) derived a climatology for a patch of turbulence, and defined it as an area of turbulence spread over a certain distance, with no spatial breaks, that lasts more than 5 minutes, starts and ends with $EDR^{1/3}$'s associated with light turbulence and has at least one $EDR^{1/3}$ that peaks over light to moderate turbulence (0.2 $m^{2/3}s^{-1}$). Differences across the two airlines arose, mostly from different sample sizes and differences in flight routes, but overall a median patch of turbulence's width and height found to be 60-70km and 1km . This result was similar to that published in Vinnichko et al. (1980) with a median patch of 20-60km and 200-700 m in length and width. The lower band of this median average (20km) for width agrees with a Steiner (1966) that estimated a length of 16km for CAT and 600-900m for width. Understanding how patch size is possibly changing with climate change may be critical to flight planning and may help us to further understand the projected increase in CAT. Here this paper aims to understand how future projected patches of moderate CAT may vary in a range of GCMs, rather than observations, over the NH and SH latitudes where CAT is most prominent. This paper initially discusses the modelled data applied, and the method of representing a patch of CAT. After this section, results and discussion of the key areas are explored and finally main points are concluded.

4.2 Methodology and Data

This investigation focuses on the mid to high latitude bands (30-75°N/S) for both hemispheres, where the eddy driven jet stream flows, at an atmospheric pressure level of 200 hPa, which is often used by cruising aircraft. This region of interest is presented within fig 4.1, which represents the upper-level wind speeds averaged over a day in 1950. Winds speeds are a combination of zonal and meridional flow. The lower latitude band of 30°N/S is an appropriate barrier with the Hadley-cell driven sub-tropical jet stream occupying the band at 200 hPa. Therefore, results will show projections of CAT generated by both jet streams, although majority associated with the polar eddy driven jet. For future reference, section 4.3 results reference NH and SH as only the results within these two bands highlighted in fig 4.1, and not the entire hemispheres.

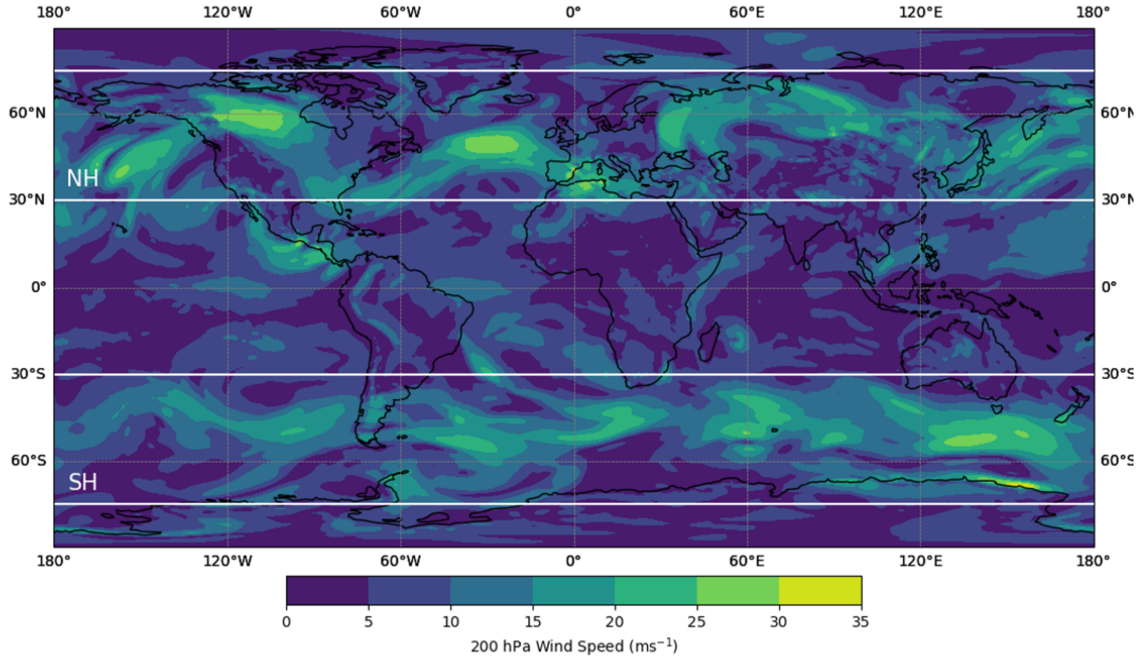

FIGURE 4.1: Upper-level wind speeds for Jan 1st in 1950 within HadGEM3-GC3.1-HM ensemble member 1. This figure used to highlight zones of interest in the northern and southern hemisphere by the white dashed lines (30-75°N/S).

Data from three GCMs are investigated within this study. Met Office Hadley Centre's HadGEM3-GC3.1 GCM data is used, which has three grid sized resolutions that are noted within this publication by 'HH/HM', 'MM' and 'LL'. Their simulated atmospheres have latitude and longitude degree spacing's of 0.23° by 0.35° (HH/HM), 0.55° by 0.83° (MM) and 1.25 ° by 1.875° (LL) (Hasrsma et al. 2020). MPI-ESM1.2, from the Max-Planck Institute, and EC-Earth3P, from a consortium of institutions, are also used within this investigation. Both have two different resolutions available for analysis, with MPI-ESM1.2 having a finer model referred to as 'XR' (0.47 ° by 0.47 °) and a coarser model 'HR' (0.94° by 0.94°) (Roberts et al., 2019). EC-Earth's two grid spaced domains are denoted by '-3P-HR' (0.35° by 0.35°) and '-3P' (0.70° by 0.70°) (Gutjahr et al.,2019). These GCMs are collated from CMIP6 HighResMIP, which is a group of CMIP6 models that was developed to reduce the model resolution differences between NWP models and GCMs (Haarsma et al. 2016). If one assumes a patch of turbulence is on average 60-70kms in width, these HighResMIP GCMs may start to resolve the individual patches in the atmosphere. These resolutions allow us to investigate the projected change to the patch size or number over time.

Turbulent kinetic energy (TKE) is on a scale too small to be resolved by current global climate modeling systems. Therefore, to identify CAT, this paper uses the assumption that large scale eddies transfer into smaller scale eddies which lead to the TKE. Through this assumption, diagnostic indices can be applied, with the premise that the upper quantiles of each index correspond to a certain EDR value.

Table 4.1 displays the rates needed for each severity of CAT, and what percentile ranges are used for each diagnostic. An average over twenty-one indices was applied within the results. The large number of diagnostics, helps to reduce formation bias, with each index effectively representing different scenarios in which CAT develops. The "Percentage Difference" column within Table 4.1 highlights the small range within each index CAT, of a certain severity, arises with in. It also represents the amount of upper-level atmospheric turbulence within the atmosphere. These percentage ranges, first discussed in Williams (2017), are based on values over the North Atlantic.

Smith et al. (2023) found an overall increase in CAT over the same region of interest as Williams (2017). Due to available access to threshold values applied in Smith et al. (2023), this paper applies such values to determine the existence of a light, light to moderate, moderate, moderate to severe and severe for all 21 indices also used in Smith et al. (2023). Through this methodology, this work can be compared effectively against Smith et al. (2023), which also uses the same three GCMs within this investigation. This paper defines a patch of CAT as an area with index values over a threshold for a given severity and assume connections in both the horizontal and diagonal components. When discussing the size of a patch of CAT, this paper refers only to its horizontal area and does not consider its vertical width, since the GCM's vertical resolution is not deemed sufficient for evaluating vertical structures. Future investigations with higher vertical resolutions should attempt this analysis.

Turbulence Strength	**Energy Dissipation Rate ($m^{2/3}s^{-1}$)**	**Percentile Range (%)**	**Percentage Difference (%)**
Light	0.1-0.2	97.0-99.1	2.1
Light to Moderate	0.2-0.3	99.1-99.6	0.5
Moderate	0.3-0.4	99.6-99.8	0.2
Moderate to Severe	0.4-0.5	99.8-99.9	0.1
Severe	>0.5	99.9-100	0.1

TABLE 4.1: Energy dissipation rates (EDR) for a median-weight category aircraft and their associated percentage range for each severity of CAT within indices. (Williams, 2017)

4.3 Results and Discussion

4.3.1 Percentage of CAT over Mid-high Latitudes

Before the CAT patch analysis , we initially focus on the amount of projected CAT that exists over the NH and SH bands (shown in fig 4.1) and how the amount of CAT varies over the 101 year period. Using Williams (2017) reference ranges for each severity of CAT (Table 4.1), Smith et al. (2023) developed threshold values for each index over the North Atlantic within a 10-year period, across all seasons. Their values of light CAT would occur within 2.1% of the atmosphere over the North Atlantic, over their 10 year period. Fig 4.2 and 4.3 display the daily percentage of CAT existing in the NH and SH bands using these Smith et al. (2023) threshold ranges. As discussed in methodology, through using thresholds determined in a region over the North Atlantic, this papers results can be effectively compared to Smith et, al (2023) and other previous work that has used this area such as Williams (2017) and Williams and Joshi (2014).

The percentage of CAT, for each severity, differ to the original range seen in Table 4.1, as our analysis includes a much wider area of interest. These figures show the daily percentages of CAT over 101 years, with a decadal average written over each sequential 10 boxes. The colour bar is plotted using a logarithmic scale, to effectively distinguish the differences across the 5 severities.

Light and Light to moderate, as expected by the ranges in Table 4.1, occupy a greater percentage of the area, compared to the remaining severities. Interestingly, despite both moderate to severe and severe turbulence existing in 0.1% of the atmosphere in Smith et al. (2023), severe often fluctuates at a higher percentage than moderate to severe. This is highlighted in both fig 4.2 and 4.3, with the introduction of light green lines, particularly prevalent near the end of the 101 year period. This difference between the two severities is linked to the distribution of CAT over these two large hemisphere bands differing to that over the North Atlantic, with the maximum threshold met and exceed more often than the moderate to severe range. For example in a probability density function (PDF) histogram, the y-axis maximum tail would extend further in these NH/SH bands compared to a PDF over the North Atlantic.

These figures highlight the seasonality of CAT, with winter and summer in both hemispheres clearly distinguishable, with a greater percentage found in winter than summer. This paper does not consider convectively induced turbulence (CIT) which is most prominent in summer (Wolff et al., 2008). Theoretically the eddy driven jet stream in the SH has less variation between winter and summer than NH jet, this is evident in comparing the percentage difference in CAT across these seasons within these figures. For the NH area, over the century, averaged across GCM projections, CAT occupies 1.85%, 0.45%, 0.19% 0.11% and 0.13% in winter and 1.44%, 0.32% , 0.14%, 0.08% and 0.11% in summer for light, light to moderate, moderate, moderate to severe and severe of the area. In comparison, within SH area, projections have a smaller difference between the two seasons with CAT occupying 1.82%, 0.42%, 0.17%, 0.1%, 0.12% in winter and 1.67%, 0.37%, 0.15%, 0.08%, 0.11% in summer, for each severity respectively.

Interestingly, the HadGEM3-GC3.1 and MPI-ESM1.2's coarser models project a slightly higher percentage of CAT over the NH area of interest, then their finer

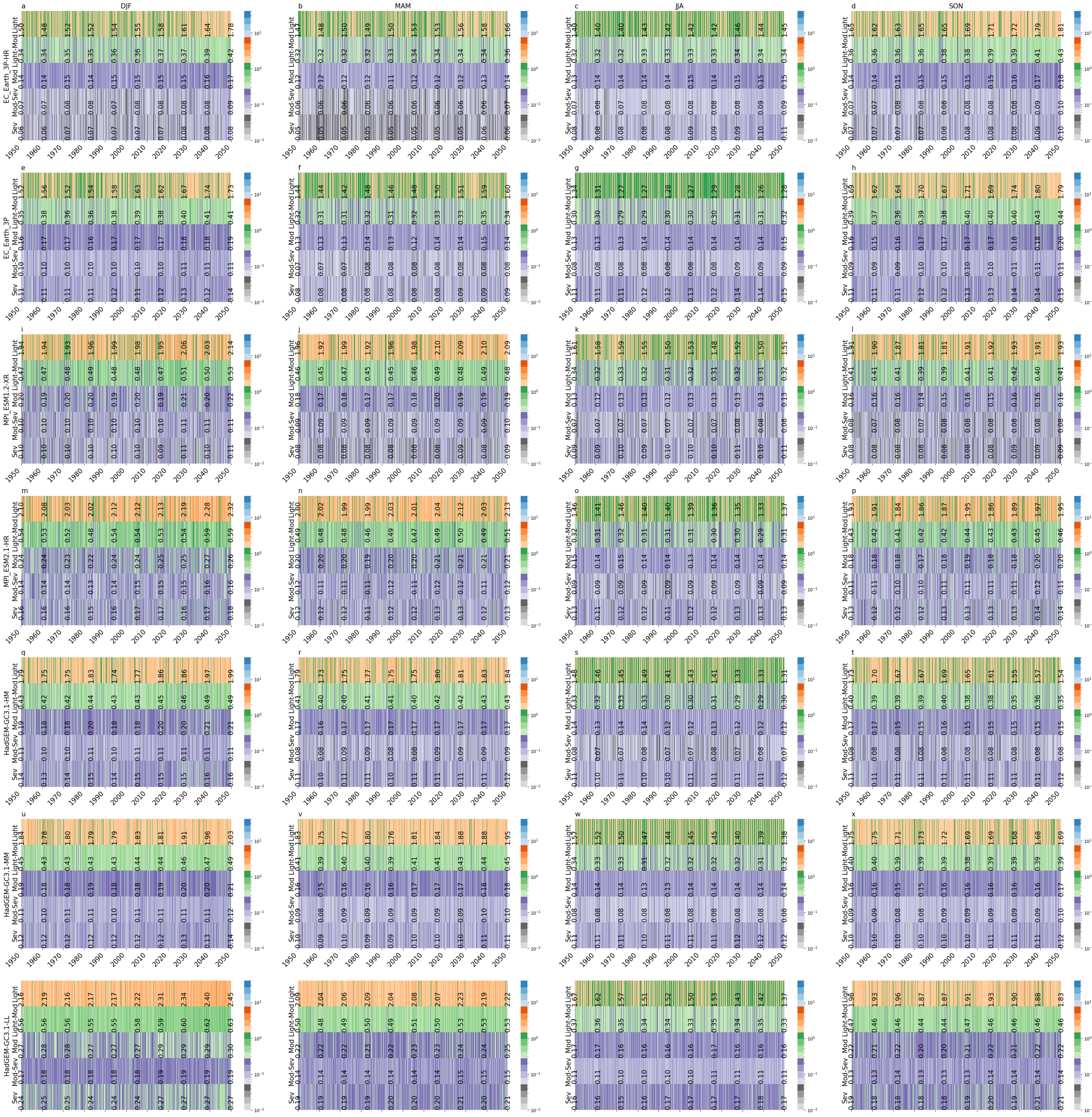

FIGURE 4.2: The fraction of CAT over the area of interest, as a percentage, for the NH band (30-75°N) for all five severities, with colour bar in log10. The median percentage value for each decade is written in black text across 10 lines. The rows are linked to the GCMs sub models in order from top to bottom as EC−Earth−3P−HR,−3P, MPI−ESM1.2−XR,−HR, HadGEM3−GC3.1−HM,-MM,−LL. Columns are associated with the season of interest, with DJF, MAM, JJA and SON travelling left to right across the figure.

counterpart. This is evident within HadGEM3-GC3.1-LL projections, the coarsest model of the seven. This model generally projects a larger amount of CAT for most seasons in the NH than the other GCMs. This is effectively shown in by the semi-continuous shading of orange signifying light CAT over the area within the bottom line of plots in fig 4.2. NH summer (JJA) is the only season without this trend, with orange shifting to green, suggesting a decline in CAT percentage within this model. From the 1950 decade to the 2040 decade, the summer-time percentage of light CAT drops from occupying 1.67% to 1.37% of the area within this HadGEM−GC3.1-LL output. This is a relative decrease of -17.88% for light turbulence. This decline in summer-time light turbulence, between the two decades, is projected in all models but EC-Earth-3P-HR.

Within fig 4.2, NH SON projections for light and light to moderate CAT have MPI-ESM1.2-XR,-HR, EC-Earth-3P and EC-Earth-3P-HR projecting a positive trend, but HadGEM3-GC3.1-HM, -MM and LL displaying a decrease. However, model disagreement changes as we progress to moderate CAT, with NH SON projections having only one model projecting a decline (HadGEM3-GC3.1-HM with relative decrease of -6.06%) . By NH SON severe CAT projections, the amount of CAT in the 2050 decade is greater than 1950 decade for all GCMs, by +0.02% as an absolute increase with a relative change of +12.50%.

In contrast, this trend variation dependent on model and severity is not found

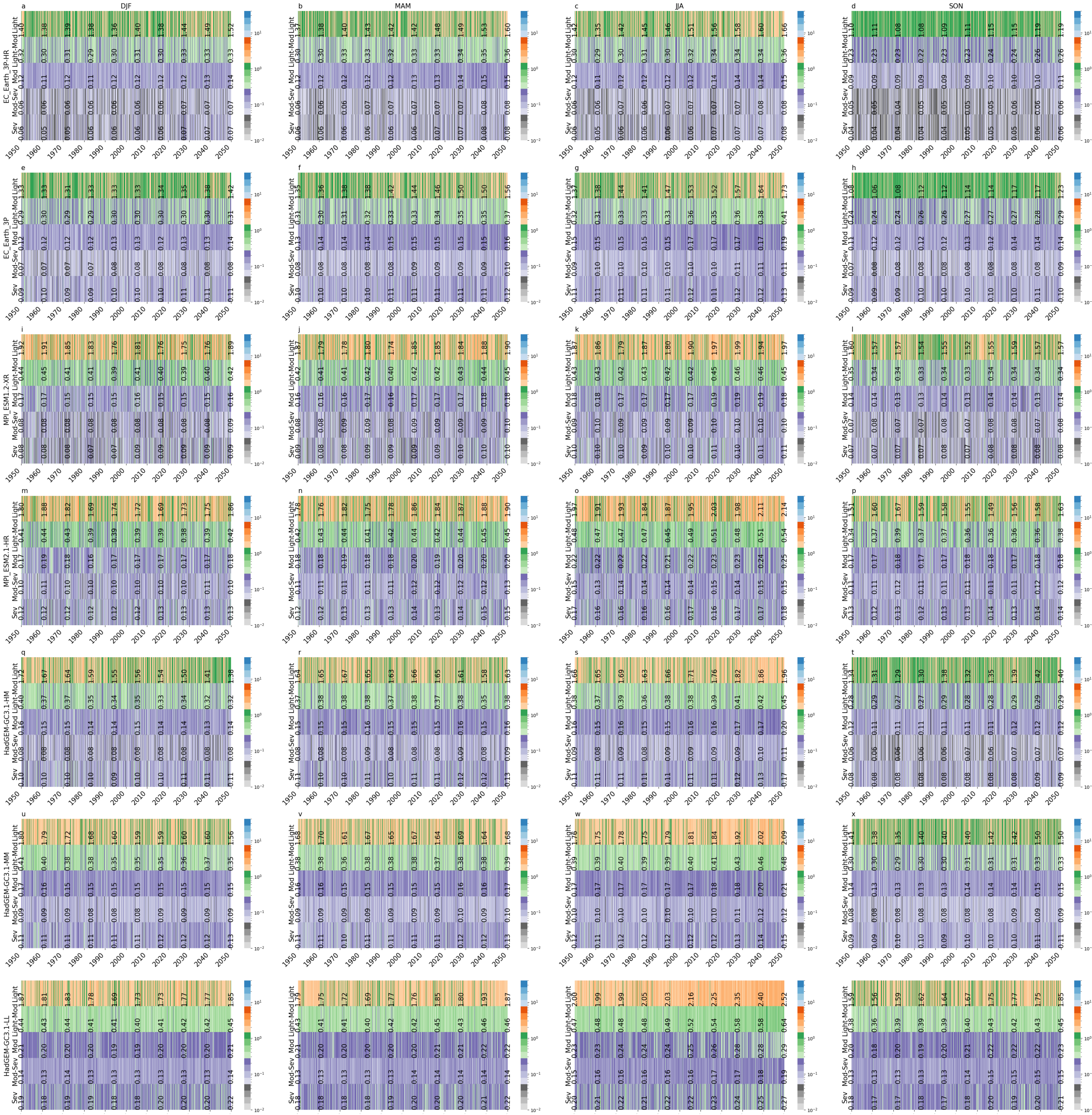

FIGURE 4.3: The daily amount of turbulence compared to the size of the SH band (30-75°S) for all five severity's, with colour bar in log10. The median percentage value for each decade is written in black text across 10 lines. The rows are linked to the GCMs sub models in order from top to bottom as EC−Earth−3P−HR,−3P, MPI−ESM1.2−XR,−HR, HadGEM3−GC3.1−HM,-MM,−LL. Columns are associated with the season of interest, with DJF, MAM, JJA and SON travelling left to right across the figure.

in the SH autumn projections. Despite, HadGEM-GC3.1-HM projected a relative decline of -0.6% in light SH MAM, all other models suggest an increase in the amount of space occupied in 2050 compared to 1950. Between 1950 to 2050, CAT within the SH autumn (MAM) has a relative increase of +4.33% +7.15%, +11.11%, +18.18%, and +23.81%, for light, light to moderate, moderate, moderate to severe and severe, respectively.

Focusing on the difference between these two decades gives an initial understanding of the general trend in CAT of the region over the 101 years, with the NH and SH winter multi-model median showing a relative increase of +11.17%, +13.79%, +13.16%, +11.6% and +17.02%, and +18.37%, +21.67% +22.06%, +25.00% and +29.79% for light, light to moderate, moderate, moderate to severe and severe, respectively. An increase in NH and SH spring is also clearly evident with CAT occupying relatively more of the region by +6.56%, +6.23%, +7.69%, +11.11% and +11.3% for MAM in fig 4.2 and +7.69%, +10.87% +9.26%,+ 15.39% and +17.02% for SON in fig 4.3. These percentage changes represent the relative shift from the 1950's to the 2050's and provide an initial indication of temporal trends in CAT across both hemispheres. A more detailed trend analysis will be presented in Section 4.3.2, with a focus on reducing decadal variability.

4.3.2 Evaluation of Moderate CAT over NH and SH

To effectively evaluate the change in moderate CAT in time, fig 4.4 and 4.5 display the amount of CAT over the first (blue) and last (orange) 30 years of the century as total area (km^2) rather than as a percentage. Here the two histograms, in each subplot, contain the daily total amounts of CAT over the 30 years. The majority of histograms displaying an increase in the probability of a larger area of CAT. There is strong model agreement that the area of CAT occurrence increases in winter, as the distribution of 2020-2050 spreads further along the y-axis. Interestingly, the coarser GCMs have a marginally more substantial shift, with the coarsest model HadGEM3-GC3.1-LL (135km) in both hemispheres having a noticeably thick right hand tail in the distribution. An increase in the total amount of CAT is also evident in autumn and spring projections, for both hemispheres.

There is less model agreement on summer-time moderate CAT totals, with the MPI-ESM1.2 and the majority of HadGEM-GC3.1 models suggesting very little change or reduction within fig 4.4 and 4.5. HadGEM3-GC3.1-HM and -MM both project a reduction in moderate CAT total area squared, between these two periods. This trend was evident within fig 4.2 and 4.3. This decline in summer-time moderate CAT is not evident in EC-Earth-3P-HR and EC-Earth-3P which project a definitive increase in the total amount in NH and SH summer, within fig 4.4 and

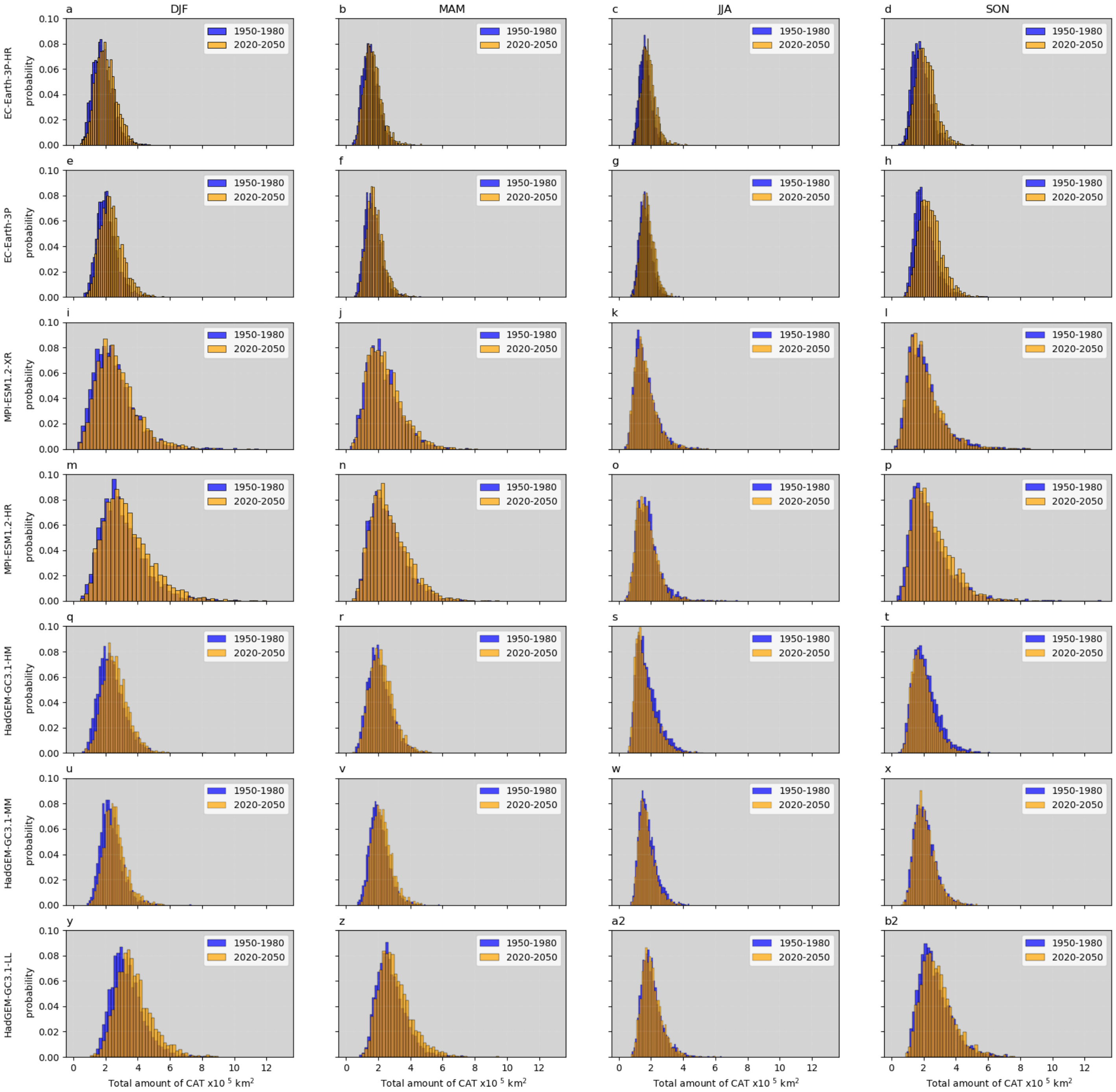

FIGURE 4.4: Histograms of the area of moderate CAT, over the NH band for the first 30 years of the period (1950-80) (blue) and the final 30 years (2020-2050)(orange). The rows show the GCMs sub models from top to bottom (EC−Earth−3P−HR,−3P, MPI−ESM1.2−XR,−HR,HadGEM3−GC3.1−HM,-MM,−LL).Columns are associated with the season of interest.

4.5.

Overall, before progressing on to individual CAT analysis, one can confirm an increase in the total amount of CAT existing in the NH and SH areas, within our GCMs, for winter, autumn and spring. However, both hemispheres projected a mixture of results for moderate summer CAT, with a lot more variation and in some cases a reduction in CAT evident. Our next focus explores if these trends in moderate CAT are related to a change in the number or size of CAT patches.

The daily average number of patches per day, for the NH and SH area, are scattered across time within fig 4.6 and 4.7. The daily average size (km^2) of a patch and the daily total area (km^2) of moderate CAT are also explored within these figures. The legends list trends in time in terms of the rate of change per year of the seasonal-mean number and size of patches, and the total CAT area. These two figures effectively show the model grid domains have an impact on the results, with coarser models generally having larger patches (in width) with a few number of patches throughout the 101 year period. This is evident by the larger spread of purple scatter in fig 4.6-4.7 a- d and q-t (EC-Earth-3P-HR and HaGEM3-GC3.1-HM), which donates a large number of patches from throughout the 101-year analysis. Table 4.2, which displays the 101-year median for the number of patches per day, the average patch size and the total area of moderate CAT for each GCM,

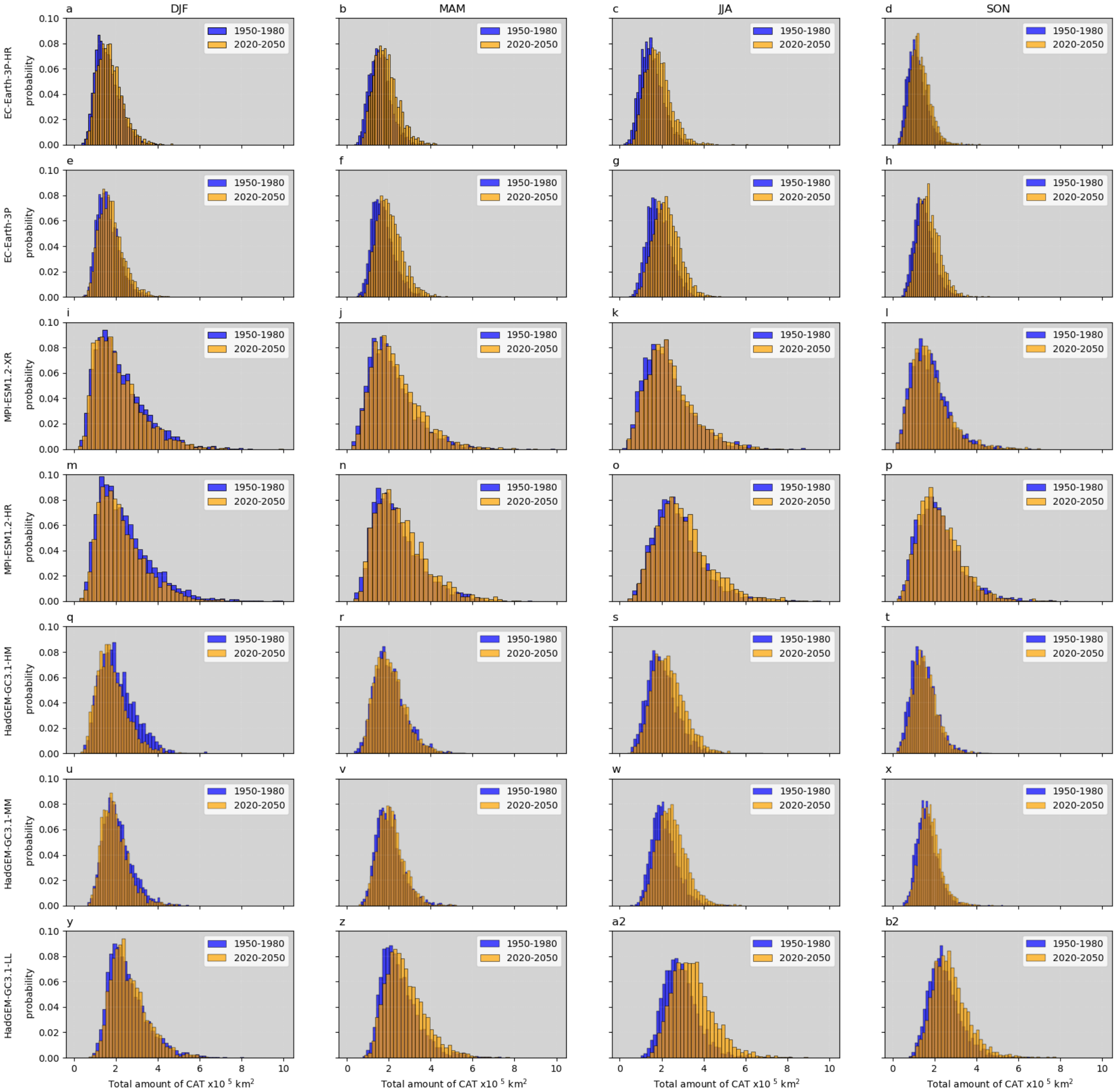

FIGURE 4.5: Histograms of total km^2 for moderate CAT, over the SH band for the first 30 years of the period (1950-80) (blue) and the final 30 years (2020-2050)(Orange). The rows are linked to the GCMs sub models in order from top to bottom as EC−Earth−3P−HR,−3P, MPI−ESM1.2−XR,−HR, HadGEM3−GC3.1−HM,-MM,−LL. Columns are associated with the season of interest.

Model	DJF			MAM		
	No. Patches	Avg Size (km^2)	Total (km^2)	No. Patches	Avg Size (km^2)	Total (km^2)
NH						
EC-Earth-3P-HR	68	1,869	185,645	57	1,891	153,117
EC-Earth-3P	24	6,144	212,659	18	5,293	165,890
MPI-ESM1.2-XR	48	3,793	236,421	44	3,825	215,047
MPI-ESM1.2-HR	18	9,350	288,193	16	9,350	241,985
HadGEM3-GC3.1-HM	130	1,105	241,854	109	1,134	205,662
HadGEM3-GC3.1-MM	34	4,865	241,962	29	4,872	206,395
HadGEM3-GC3.1-LL	12	24,441	341,144	9	24,268	278,063
SH						
EC-Earth-3P-HR	60	1,737	150,776	64	1,737	159,960
EC-Earth-3P	20	5,197	157,829	22	5,207	178,714
MPI-ESM1.2-XR	41	3,464	186,612	44	3,532	199,645
MPI-ESM1.2-HR	14	9,212	202,843	16	9,236	223,572
HadGEM3-GC3.1-HM	91	1,376	172,459	103	1,383	189,705
HadGEM3-GC3.1-MM	26	4,835	187,326	29	4,820	196,842
HadGEM3-GC3.1-LL	8	23,646	244,738	9	23,738	250,051

Model	JJA			SON		
	No. Patches	Avg Size (km^2)	Total (km^2)	No. Patches	Avg Size (km^2)	Total (km^2)
NH						
EC-Earth-3P-HR	86	1,319	169,108	85	1,442	183,760
EC-Earth-3P	26	4,927	164,995	29	5,107	207,644
MPI-ESM1.2-XR	44	2,345	151,158	46	2,853	182,603
MPI-ESM1.2-HR	15	8,971	165,836	17	9,166	217,744
HadGEM3-GC3.1-HM	112	876	157,107	121	882	190,839
HadGEM3-GC3.1-MM	29	4,571	165,278	32	4,673	195,961
HadGEM3-GC3.1-LL	8	21,890	193,377	10	22,698	257,369
SH						
EC-Earth-3P-HR	53	2,059	161,742	41	1,929	117,841
EC-Earth-3P	20	6,829	198,509	16	6,522	154,487
MPI-ESM1.2-XR	41	4,272	212,804	31	4,116	163,642
MPI-ESM1.2-HR	16	12,290	268,738	13	11,546	207,704
HadGEM3-GC3.1-HM	96	1,546	206,457	69	1,419	144,998
HadGEM3-GC3.1-MM	30	4,872	223,886	23	4,872	169,354
HadGEM3-GC3.1-LL	10	24,095	306,311	8	24,095	248,032

TABLE 4.2: The number of patches, average patch size, and total area of CAT on average across the 101-year period for each CMIP6 GCM for all seasons in NH and SH.

also highlights this model dependence. For example, HadGEM3-GC3.1-HM projections suggest an overall median patch size of 1,105 km^2 in NH winter with 130 patches. This models coarsest counterpart (-LL) projects an average patch size of 24, 441 km^2, with only 12 patches. The range of values shown in Table 4.2 is important when discussing Table 4.3, which displays the multi-model median for the number of patches, average patch size and total area of moderate CAT across the GCMs. On average, winter has the largest number of patches and total area in both hemispheres over the 101 year period (Table 4.3). Interestingly, JJA and SON in both hemispheres have similarly large projections of the average patch size, in comparison to DJF and MAM.

Season	**No. Patches**		**Avg Size** (km^2)		**Total** (km^2)	
	NH	SH	NH	SH	NH	SH
DJF	34	26	3,793	3,464	236,421	186,612
MAM	29	29	3,825	3,532	206,395	196,842
JJA	29	30	4,571	4,872	165,278	206,457
SON	32	23	4,673	4,872	195,961	169,354

TABLE 4.3: Multi-model median for the number of daily patches, the average size and the total patch area across the 101 years, over the 21 indices and over the 7 models used for this analysis listed in Table 4.2.


DJF
MAM
JJA
SON
EC_Earth_3P-HR
EC_Earth_3P
MPI_ESM1.2-XR
MPI_ESM1.2-HR
HadGEM_GC3.1-HM
HadGEM_GC3.1-MM
HadGEM_GC3.1-LL
no. of patches
No. of patches
Median patch size (10^3 km^2)
Total (10^5 km^2)
Year
a
no of patches: 0.13 ± 0.016 no. patches/year
Median patch size: 0.91 ± 0.391 km^2/year
Total: 329.08 ± 41.359 km^2/year
b
no of patches: 0.10 ± 0.014 no. patches/year
Median patch size: 0.14 ± 0.304 km^2/year
Total: 221.40 ± 34.040 km^2/year
c
no of patches: 0.14 ± 0.012 no. patches/year
Median patch size: -0.14 ± 0.142 km^2/year
Total: 272.34 ± 27.141 km^2/year
d
no of patches: 0.18 ± 0.016 no. patches/year
Median patch size: 0.48 ± 0.260 km^2/year
Total: 451.23 ± 40.741 km^2/year
e
no of patches: 0.05 ± 0.006 no. patches/year
Median patch size: 1.35 ± 1.744 km^2/year
Total: 360.16 ± 46.996 km^2/year
f
no of patches: 0.04 ± 0.004 no. patches/year
Median patch size: -4.87 ± 1.385 km^2/year
Total: 184.24 ± 33.798 km^2/year
g
no of patches: 0.05 ± 0.003 no. patches/year
Median patch size: -1.57 ± 0.163 km^2/year
Total: 204.82 ± 22.950 km^2/year
h
no of patches: 0.06 ± 0.005 no. patches/year
Median patch size: -0.58 ± 0.120 km^2/year
Total: 486.09 ± 41.793 km^2/year
i
no of patches: 0.06 ± 0.021 no. patches/year
Median patch size: 1.34 ± 0.826 km^2/year
Total: 198.71 ± 83.689 km^2/year
j
no of patches: 0.05 ± 0.016 no. patches/year
Median patch size: -0.50 ± 0.693 km^2/year
Total: 192.97 ± 66.136 km^2/year
k
no of patches: 0.04 ± 0.011 no. patches/year
Median patch size: -0.76 ± 0.395 km^2/year
Total: 1.99 ± 37.662 km^2/year
l
no of patches: 0.02 ± 0.016 no. patches/year
Median patch size: 0.64 ± 0.674 km^2/year
Total: 58.60 ± 55.376 km^2/year
m
no of patches: 0.03 ± 0.007 no. patches/year
Median patch size: 4.87 ± 2.846 km^2/year
Total: 417.72 ± 81.436 km^2/year
n
no of patches: 0.02 ± 0.006 no. patches/year
Median patch size: 0.87 ± 2.102 km^2/year
Total: 149.54 ± 82.888 km^2/year
o
no of patches: 0.01 ± 0.004 no. patches/year
Median patch size: -1.10 ± 0.325 km^2/year
Total: -39.25 ± 39.353 km^2/year
p
no of patches: 0.03 ± 0.006 no. patches/year
Median patch size: 1.17 ± 0.921 km^2/year
Total: 341.21 ± 81.772 km^2/year
q
no of patches: 0.26 ± 0.035 no. patches/year
Median patch size: 2.93 ± 0.411 km^2/year
Total: 369.82 ± 56.954 km^2/year
r
no of patches: 0.14 ± 0.030 no. patches/year
Median patch size: 1.49 ± 0.326 km^2/year
Total: 159.49 ± 49.978 km^2/year
s
no of patches: -0.02 ± 0.019 no. patches/year
Median patch size: -0.07 ± 0.037 km^2/year
Total: -153.91 ± 41.207 km^2/year
t
no of patches: -0.08 ± 0.023 no. patches/year
Median patch size: 0.12 ± 0.101 km^2/year
Total: -219.18 ± 40.963 km^2/year
u
no of patches: 0.05 ± 0.007 no. patches/year
Median patch size: -0.10 ± 0.041 km^2/year
Total: 303.27 ± 40.441 km^2/year
v
no of patches: 0.05 ± 0.007 no. patches/year
Median patch size: -0.04 ± 0.043 km^2/year
Total: 248.76 ± 41.381 km^2/year
w
no of patches: 0.02 ± 0.005 no. patches/year
Median patch size: -0.84 ± 0.105 km^2/year
Total: -35.95 ± 26.249 km^2/year
x
no of patches: 0.02 ± 0.005 no. patches/year
Median patch size: -0.55 ± 0.091 km^2/year
Total: 9.92 ± 32.595 km^2/year
y
no of patches: 0.02 ± 0.002 no. patches/year
Median patch size: -1.38 ± 0.241 km^2/year
Total: 493.76 ± 48.099 km^2/year
z
no of patches: 0.01 ± 0.002 no. patches/year
Median patch size: -1.19 ± 0.412 km^2/year
Total: 276.40 ± 46.952 km^2/year
a2
no of patches: 0.01 ± 0.001 no. patches/year
Median patch size: -9.02 ± 0.606 km^2/year
Total: -5.67 ± 26.087 km^2/year
b2
no of patches: 0.01 ± 0.002 no. patches/year
Median patch size: -9.52 ± 0.699 km^2/year
Total: 127.40 ± 34.550 km^2/year
1960
1980
2000
2020
2040

FIGURE 4.6: Scatter plot of the number of moderate patches per day, the median patch size and total area of CAT over the NH band. The lines of best fit show the change per season, rather than day. The rows show GCMs in order from top to bottom as EC−Earth−3P−HR,−3P, MPI−ESM1.2−XR,−HR, HadGEM3−GC3.1−HM,-MM,−LL. Columns show the seasons DJF, MAM, JJA and SON.

As shown in fig 4.4 and 4.5, the total amount of moderate CAT has increased in time, with the rate of change given by the slopes found in fig 4.6 and 4.7. In winter over the NH area, models project an increase of between +198.71 to +493.76 km^2 more moderate CAT per year, with an average of +360.16 +/- 48.10 km^2. Interestingly, HadGEM3-GC3.1-LL, which projects the maximum increase of +493.76 +/- 48.10 km^2 , also projects a decline in the average patch size, with a drop of -1.38 +/-0.24 km^2 per DJF season. Within this model (fig 4.6.y), the total change in CAT area is connected to the larger number of patches, with +2.02 more patches over the 101 years. A similar outcome is seen in HaGEM3-GC3.1-MM (fig.4.6.u). Over the remaining 5 models, the average patch size and the number of patches increase in time. However, EC-Earth-3P (fig4.6.e) has insignificant linear regression trends in time, with large errors for the median patch size relationship. This implies, time has no significant linear effect on median patch size within this model, at a 95% confidence level, and the slope is not statistically distinguishable from zero. Although, despite these two models disagreeing and one model with an insignificant trend in time, DJF NH winters on average are likely becoming more turbulent due to the increase in both the average patch size and the number of patches. Over the 101 years, GCMs project average patch size has increased by +135.34 +/- 41.51 km^2 with+ 5.05 +/-0.7 more patches.

Over the NH MAM projections, an increase in the total CAT area is evident in HadGEM3-GC3.1-MM and LL projections, despite a decline in the average patch size (fig 4.6.v, x, z, b2). Although, HadGEM3-GC3.1-HM (fig 4.6.r) projects an increase of +16,108 km^2 moderate spring-time CAT, due to both the number of patches increasing by +14.14 ,and the average patch area becoming wider by +150.49 km^2, by the end of the century. However, the remaining GCMs suggest the increase in the total amount of CAT in NH spring is related to an increase in number of patches, due to insignificant increases (fig 4.6.b, n) and decreases (fig 4.6.f,v,z) in patch size. Overall, due to model disagreement and insignificant trends, the model average for an average area of spring-time CAT over the NH area is -0.04+ 0.412 km^2 per year. The multi-model median shows NH spring-time CAT total amounts are increasing by +192.97 +/- 46.95 km^2 per year, with 0.05 +/- 0.01 more patches per year. This total increase is the second highest average across the model projections, with NH SON total area increasing by +127.40 +/- 40.96 km^2 per year, and JJA decreasing insignificantly by -5.67 +/- 27.14 km^2 per year.

EC-Earth-3P and EC-Earth-3P-HR project the second and third greatest increase in the total areas of NH CAT per year (fig.4.6.d, h), within their NH SON projections, with + 486.09 +/- 41.79 km^2 and +451.23 +/- 40.74 km^2 per year, respectively. Interestingly, this EC-Earth-3P increase is dependent on the increase in the number of patches. Over the 101 years, there's +6.06 more patches by the end of the period over the NH area for SON moderate CAT, within this model. However, their average patch size is decreasing by -0.58 +/- 0.12 km^2. HadGEM3-GC3.1-MM and LL (fig 4.6.x, b2) both project a decline in average patch size by -0.55 +/- 0.091 km^2 and -9.52 +/- 0.70 km^2. The remaining model outputs all project a increase in the average patch size, even HadGEM3-GC3.1-HM (fig 4.6.t) which interestingly projects a decrease in the total amount of CAT by -219.18 +/- 40.963 km^2. This HadGEM-GC3.1-HM total area decline is consistent with a drop in the number of patches, with a decrease of -0.08 +/- 0.02 per year. There is a mix in model projections for NH autumn average patch size. The multi-model median projections a wider patch of +48.48 km^2 by the end of the century, despite the three out of seven projecting a decline in size. Despite EC-Earth-3P and EC-Earth-3P-HR projecting their greatest increase in NH moderate CAT in the SON results, the large decrease found in HadGEM-GC3.1-HM results in a multi-model mean increase of +12,867 km^2 over the 101 year period. The number of patches overall increases with +2.02 more patches arising in 2050 than 1950.

Summer-time CAT over the NH area is not increasing on average across the

GCMs, with trends ranging between -153.91 to + 272.34 km^2 per year over the models. HadGEM3-GC3.1-LL, MPI-ESM1.2-XR and MPI-ESM1.2-HR do not produce a significant trend in time for the total amount of CAT. Within these models, the number of patches are increasing in time, whereas the average patch size is decreasing. In all GCMs, apart from HadGEM3-GC3.1-HM, the number of patches increase in the NH summer-time projections. HadGEM3-GC3.1-HM (fig 4.6.s) projects a statistically significant reduction in the average size, number of and total amount of CAT. In contrast, EC-Earth-3P-HR and EC-Earth-3P both project a significant increase in the total amount of summer-time moderate CAT (fig 4.6.c,g). This result is consistent with previous findings projecting an increase of NH summer-time CAT within these models. These two models have their associated increase in CAT related to the number of patches, with EC-Earth-3P-HR and EC-Earth-3P projecting +14.14 and +5.05 more patches by the end of the century. However, as discussed, these model disagreements lead to an insignificant trend in time for NH summer moderate CAT.

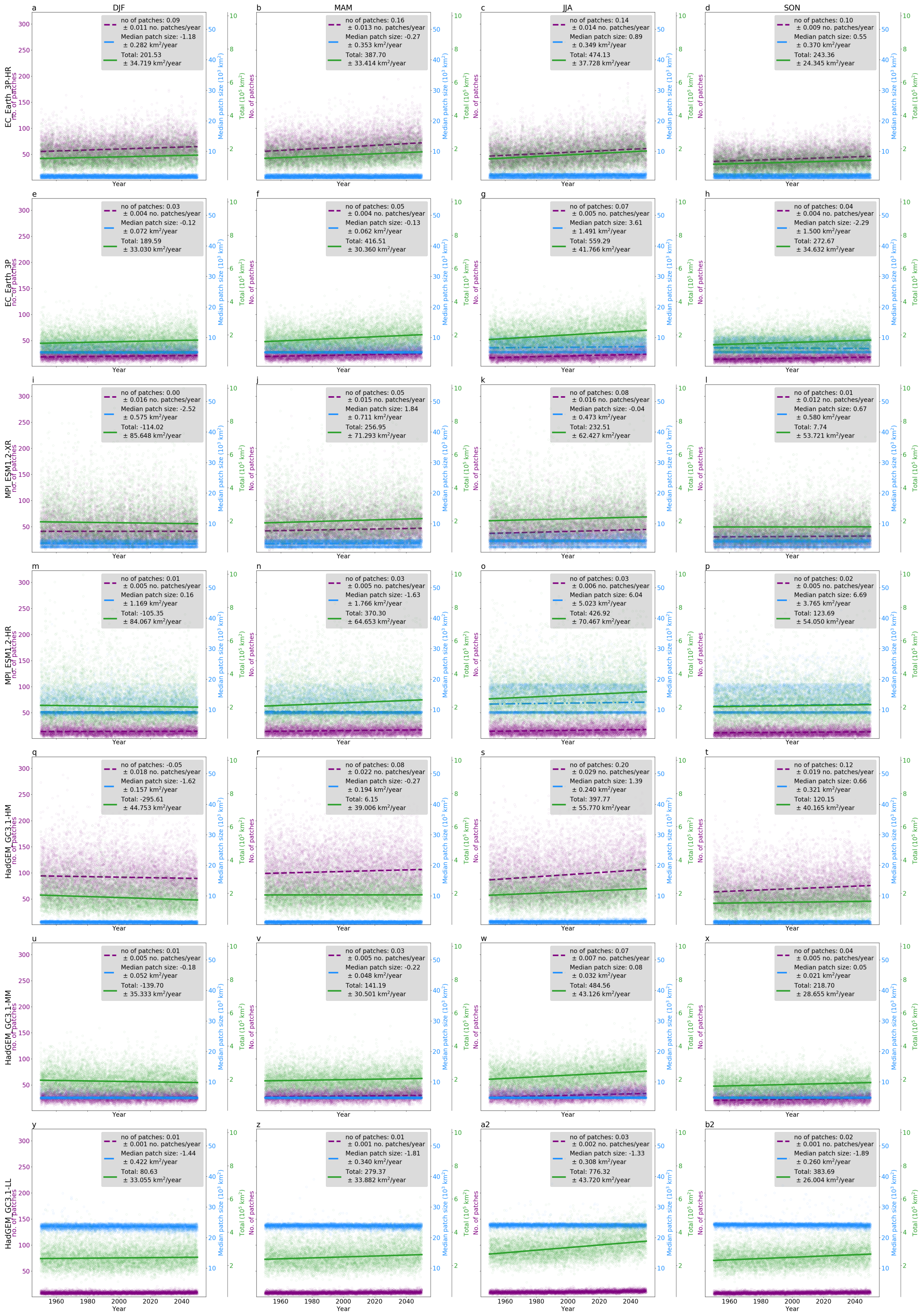
DJF
MAM
JJA
SON
EC_Earth_3P-HR
EC_Earth_3P
MPI_ESM1.2-XR
MPI_ESM1.2-HR
HadGEM_GC3.1-HM
HadGEM_GC3.1-MM
HadGEM_GC3.1-LL
no. of patches
Median patch size (10³ km²)
Total (10⁵ km²)
No. of patches
Year
a
no of patches: 0.09 ± 0.011 no. patches/year
Median patch size: -1.18 ± 0.282 km²/year
Total: 201.53 ± 34.719 km²/year
b
no of patches: 0.16 ± 0.013 no. patches/year
Median patch size: -0.27 ± 0.353 km²/year
Total: 387.70 ± 33.414 km²/year
c
no of patches: 0.14 ± 0.014 no. patches/year
Median patch size: 0.89 ± 0.349 km²/year
Total: 474.13 ± 37.728 km²/year
d
no of patches: 0.10 ± 0.009 no. patches/year
Median patch size: 0.55 ± 0.370 km²/year
Total: 243.36 ± 24.345 km²/year
e
no of patches: 0.03 ± 0.004 no. patches/year
Median patch size: -0.12 ± 0.072 km²/year
Total: 189.59 ± 33.030 km²/year
f
no of patches: 0.05 ± 0.004 no. patches/year
Median patch size: -0.13 ± 0.062 km²/year
Total: 416.51 ± 30.360 km²/year
g
no of patches: 0.07 ± 0.005 no. patches/year
Median patch size: 3.61 ± 1.491 km²/year
Total: 559.29 ± 41.766 km²/year
h
no of patches: 0.04 ± 0.004 no. patches/year
Median patch size: -2.29 ± 1.500 km²/year
Total: 272.67 ± 34.632 km²/year
i
no of patches: 0.00 ± 0.016 no. patches/year
Median patch size: -2.52 ± 0.575 km²/year
Total: -114.02 ± 85.648 km²/year
j
no of patches: 0.05 ± 0.015 no. patches/year
Median patch size: 1.84 ± 0.711 km²/year
Total: 256.95 ± 71.293 km²/year
k
no of patches: 0.08 ± 0.016 no. patches/year
Median patch size: -0.04 ± 0.473 km²/year
Total: 232.51 ± 62.427 km²/year
l
no of patches: 0.01 ± 0.012 no. patches/year
Median patch size: 0.67 ± 0.580 km²/year
Total: 7.74 ± 53.721 km²/year
m
no of patches: 0.01 ± 0.005 no. patches/year
Median patch size: 0.16 ± 1.169 km²/year
Total: -105.35 ± 84.067 km²/year
n
no of patches: 0.03 ± 0.005 no. patches/year
Median patch size: -1.63 ± 1.766 km²/year
Total: 370.30 ± 64.653 km²/year
o
no of patches: 0.03 ± 0.006 no. patches/year
Median patch size: 6.04 ± 5.023 km²/year
Total: 426.92 ± 70.467 km²/year
p
no of patches: 0.02 ± 0.005 no. patches/year
Median patch size: 6.69 ± 3.765 km²/year
Total: 123.69 ± 54.050 km²/year
q
no of patches: -0.05 ± 0.018 no. patches/year
Median patch size: -1.62 ± 0.157 km²/year
Total: -295.61 ± 44.753 km²/year
r
no of patches: 0.08 ± 0.022 no. patches/year
Median patch size: -0.27 ± 0.194 km²/year
Total: 6.15 ± 39.006 km²/year
s
no of patches: 0.20 ± 0.029 no. patches/year
Median patch size: 1.39 ± 0.240 km²/year
Total: 397.77 ± 55.770 km²/year
t
no of patches: 0.12 ± 0.019 no. patches/year
Median patch size: 0.66 ± 0.321 km²/year
Total: 120.15 ± 40.165 km²/year
u
no of patches: 0.01 ± 0.005 no. patches/year
Median patch size: -0.18 ± 0.052 km²/year
Total: -139.70 ± 35.333 km²/year
v
no of patches: 0.03 ± 0.005 no. patches/year
Median patch size: -0.22 ± 0.048 km²/year
Total: 141.19 ± 30.501 km²/year
w
no of patches: 0.07 ± 0.007 no. patches/year
Median patch size: 0.08 ± 0.032 km²/year
Total: 484.56 ± 43.126 km²/year
x
no of patches: 0.04 ± 0.005 no. patches/year
Median patch size: 0.05 ± 0.021 km²/year
Total: 218.70 ± 28.655 km²/year
y
no of patches: 0.01 ± 0.001 no. patches/year
Median patch size: -1.44 ± 0.422 km²/year
Total: 80.63 ± 33.055 km²/year
z
no of patches: 0.01 ± 0.001 no. patches/year
Median patch size: -1.81 ± 0.340 km²/year
Total: 279.37 ± 33.882 km²/year
a2
no of patches: 0.03 ± 0.002 no. patches/year
Median patch size: -1.33 ± 0.308 km²/year
Total: 776.32 ± 43.720 km²/year
b2
no of patches: 0.02 ± 0.001 no. patches/year
Median patch size: -1.89 ± 0.260 km²/year
Total: 383.69 ± 26.004 km²/year
50
100
150
200
250
300
10
20
30
40
50
2
4
6
8
10
1960
1980
2000
2020
2040

FIGURE 4.7: Scatter plot of the number of moderate patches per day, the median patch size and total area of CAT over the SH. The lines of best fit show the change per season, rather than day. The rows are linked to the GCMs sub models in order from top to bottom as EC−Earth−3P−HR,−3P, MPI−ESM1.2−XR,−HR, HadGEM3−GC3.1−HM,-MM,−LL . Columns show seasons (DJF, MAM, JJA and SON).

A decline in the total area of moderate CAT in SH summer is evident in fig 4.7 for 5 out of 7 GCMs. The multi-model median change over the 101 year period is -10, 640.35 km^2 with average patches decreasing in width by -119.18 km^2. MPI-ESM1.2-HR is the only model projecting a wider average patch with an insignificant trend of +0.16 +/- 1.17 km^2 per year. However, the multi-model average for the number of patches is increasing over the 101 period, +2.02 more patches by 2050 compared to 1950. This increase is due the EC-Earth-3P-HR and EC-Earth-3P projections suggesting with +9.09 and +3.03 more patches projected by the end of the period, respectively for each model. Despite, EC-Earth-3P-HR and EC-Earth-3P both projecting a significant increase in the total amount of CAT by +201.52 +/- 34.72km^2 and 189.59 +/- 33.03 km^2 per year, a decline in CAT is found overall across the GCMs.

EC-Earth-3P-HR projects an increase in the total amount of CAT for all seasons, with JJA in the SH area (winter) having a largest increase of +474.13 +/- 37.73 km^2 per year. SH autumn (MAM) follows this with an increase of +387.70 +/- 33.40 km^2 per year, and spring with a rate of +243.36 +/- 24.35. For JJA and SON, this increase can be attributed to both the size and number of patches increasing in time. SH autumn (MAM), like DJF, has an increase in the number of patches but a decline in the width of the average patch size. Across SH autumn, all models, apart from MPI-ESM1.2-XR, project this decline in the median patch size, with an average decrease of -0.25 +/- 0.34 km^2 per year. Interestingly, this is insignificant overall due to MPI-ESM1.2-XR (fig 4.7.j) projecting an increase of +1.84 +/- 0.71 km^2 per year. MPI-ESM1.2-XR projects wider average patches and an increase in the number of patches , which leads to a total rise of +256.95 +/- 71.29 km^2. This individual model output is similar to the GCMs average, with +279.37 +/- 33.88 km^2 per year. The area of CAT in SH autumn is projected to increase by +28, 216.37 km^2 by the end of the century due to an increase in the number of patches, with +5.05 more patches seen in 2050 compared to 1950.

The greatest projected total increase in CAT, across both hemispheres, arises in HadGEM3-GC3.1-LL projection of SH winter values (fig 4.7.a2), with rate of +776.32 +/- 43.72 km^2 per year. Interestingly, this model and MPI-ESM1.2-XR (fig 4.7.k) both project a decline in the median width of a patch of turbulence, but an increase in the number of patches. The remaining five models project an increase in both median patch size and number of patches for SH winter-time CAT. In fact, there is a relatively substantial increase in width within MPI-ESM1.2-HR projections for SH JJA with an increase of +6.04 +/- 5.02 per year. This is the second largest increase in average patch width, with this model projecting the greatest change in SH SON at +6.69 +/- 3.77 km^2 per year. The multi-model median for total amount of extra moderate SH winter-time CAT, by the end of the century, is +47, 887.13 km^2 , with patches wider by an extra +89.89 km^2 and more common by +7.07 more patches.

In comparison to the NH winter, SH JJA has a greater increase in the total amount of CAT by an extra 11,510.97 km^2 and with 2 more extra patches of CAT compared to NH increases. However, despite the large increases in MPI-ESM1.2-HR SH JJA projections, NH winter patches are on average getting wider by 45.45 km^2 more than SH projections.

The final season to explore within fig 4.7 is SH spring. Over the SH area, on average across the GCMs, the total amount of SON CAT increases by +218.70 +/- 34.63 km^2 per year, with the average patch widening by +0.55 +/- 0.37 km^2 per year and the number of patches increasing by +0.04 +/- 0.005 per year . These three variables increase in the majority of models, with only HadGEM3-GC3.1-LL (fig 4.7.b2) and EC-Earth-3P (fig 4.7.h) developing a decrease in the median area of CAT by -1.89+/- 0.26 and -2.29 +/- 1.50 km^2 per year, respectively.

The ranges of the y-axis with fig.4 6 and 4.7 explore the maximum number of patches, the total CAT area (km^2) and the median patch size. The ranges differ between the NH and SH figures, with NH projections having a greater range than SH findings.

4.4 Conclusion

Using an ensemble of CMIP6 GCMs, this paper analysed the area of CAT within two mid to high latitude bands over the NH and SH to determine the projected trends. The initial investigation focused on the percentage of CAT that exists within these two bands (fig's 4.2 and 4.3) . As expected light CAT exists in a larger percentage of the areas, with 1.85% (1.82%) and 1.44% (1.67%) occurring within NH (SH) winter and summer. The seasonality of CAT is evident within these initial findings with winter and summer in both hemispheres clearly distinguishable, with a greater percentage found in winter than summer. Interestingly, there was less variation in the two seasons in the SH area, which is likely related to the eddy-driven jet being more similar between the two seasons, due to less land mass over the SH. Despite both moderate to severe and severe turbulence existing in 0.1% of the atmosphere in our reference threshold from Smith et al. (2023), severe often developed more often than moderate to severe. This is due to the maximums found over these two large areas exceeding that within values from Smith et al. (2023), which used a smaller study region over the North Atlantic. It is shown in fig's 4.2 and 4.3 that the percentage of light CAT over JJA is simulated to decrease in several GCMs. However, different trends are seen for the remaining severities of CAT. The difference between the 2050 and 1950 decades gives an initial understanding of the general trend in CAT over the 101 years, with NH and SH winter having an increase of +0.21%, +0.06%, +0.03%, +0.02% and +0.02% and +0.3%, +0.08% +0.04%, +0.02% and +0.025% for light, light to moderate, moderate, moderate to severe and severe, respectively, but further analysis was required due to decadal variability.

The total amount of moderate CAT per day (km^2) in 1950-80 and 2020-50 is displayed over fig's 4.4 and 4.5. There is strong model agreement that winter, autumn and spring CAT area for both hemispheres was increasing. These histograms highlight the increasing probability of the area of moderate CAT in the future exceeding certain threshold. There is less model agreement on summer-time moderate CAT area trends, with the Max-Planck GCMs and most of the Met Office Hadley Center models suggesting very little change or reduction within fig 4.4 and 4.5. This decline in JJA moderate CAT area is not evident in EC-Earth-3P-HR and EC-Earth-3P which project a definitive increase in the total amount in NH and SH summer, within fig 4.4 and 4.5. EC-Earth projections performing yielding similar results for both hemispheres. EC-Earth projections are consistent in projecting an increase in CAT over both hemispheres for all seasons, whereas MPI-ESM1.2 and HadGEM models have variations.

The main objective of the paper is to determine what this increase or decrease in CAT means in terms of how the patches of CAT vary in time. Figs 4.6 and 4.7 explored the number of patches per day averaged on to a yearly value, the average size of patches in km^2, and the number of patches. Despite some model variability, NH and SH winter CAT area increased on average by +360.16 +/- 48.10 km^2 and +474.13 +/- 43.72 km^2 per year. This increase is due to an increase in both the average patch size and the number of patches, with an increase of +1.32 +/- 0.42 km^2 and +0.05+/- 0.007 patches per year for the NH and 0.89 +/- 0.31 km^2 and +0.07 +/- 0.007 patches per year for SH. In comparison to the NH winter, SH JJA has a greater increase in the total amount of CAT by an extra 11,510.97 km^2 by 2050 and with 2 further extra patches of CAT.

NH spring-time total CAT area is increasing by +192.97 +/- 46.95 km^2 per year, found to be linked to the number of patches increasing by +0.05 +/- 0.01 patches per year, with the average patch size insignificantly increasing in time. Over the SH area, the total area of spring-time CAT increases by +218.70 +/- 34.63 km^2 per year, with the average patch size increasing by +0.55 +/- 0.37 km^2 and the number of patches increasing by +0.04 +/- 0.005 per year.

There is low model agreement over JJA in the NH area, with -5.67 +/- 27.14 km^2 per year the average shift in the total area of CAT. EC-Earth-3P and EC-Earth-3P-HR project an increase in NH JJA CAT area, connected with an increase in the number of patches per year, +14.14 and +5.05 more patches by the end of the century. SH summer projections of CAT area are also decreasing in time, but at a significant rate of -105.35 +/- 35.33 km^2 per year. This decline is associated with a decrease in the average patch size.

Autumn total area CAT projections have a increasing trend in time, with an increase in the NH and SH of +127.4 +/- 40.96 km^2 and +279.37 +/- 33.88 km^2 per year. There is a greater increase in CAT area over SH autumn compared to NH autumn. This NH area SON increase is linked to an increase in the size and number of patches (+48.48 km^2 and +2.02 more patches by end of century). Although there is some model disagreement in the NH SON average moderate patch size projection.

Overall, this paper broke down into the physical shift of CAT patches in time, with the number of patches often increasing, except if the overall trend is negative. For implications on the aviation sector, this may imply flight routes will be forced to take longer, more convoluted paths to avoid these new patches of moderate turbulence. The percentage of CAT over the areas is a small percentage, but as shown through this analysis it is projected to increase in both hemispheres, and will likely impact flight planning control with an increased number of patches to avoid. Further research is needed to explore regional shifts, with this work taking an average over the mid-latitude bands over the north and south hemisphere.

Future work should also focus on the vertical shifts in time, with this analysis focusing on patch width one single atmospheric pressure level.

Chapter 5

Global change in mountain wave turbulence within high resolution climate models

Abstract

Using a multi-model approach, this paper quantified global changes in mountain wave turbulence (MWT) within a high-end warming scenario. Initial analysis found model resolution dependency apparent, therefore three high resolution global climate modeled datasets were used within the analysis; HadGEM3-GC3.1-HM (25km), EC-Earth-3P-HR(36km) and MPI-ESM1.2-XR (34km). Regional dependencies developed around each model and index, with seasonal components

an important contributor to results. A sub-continental approach was developed, focusing on all regions in which MWT arose. On average a projected increase in moderate or greater MWT developed over the entire continent of North America. However, a projected decline developed over the Rocky Mountain range in all seasons but northern hemisphere (NH) winter, with an increase of +60.6% over the 101 year investigation period. NH summer, spring and autumn dropped by -58.3%, -41.2 % and -30.9%. Over several mountain ranges an increase was evident, particularly over Greenland and regions in Asia. However, a drop in moderate or greater MWT also arose over the Alps, Atlas and northern and central Andes. Southern Andes and the Himalayas had seasonal differences resulting in a mix of projected outcomes. A final aim arose around the connection to low-level, surface wind flow and MWT production. This paper found links between MWT trends and the shift in projected median surface wind flow. The aviation sector should be aware of the future projections in MWT, particularly for those where large increase over the 101 year period are evident, such as Asia, Greenland and the Antarctic.

5.1 Introduction

Mountains have a large impact on the atmosphere, from increasing localised precipitation events, to generating vertical and horizontal atmospheric waves. Mountain waves can grow, as they propagate into higher altitudes with lower air density (Kim et al., 2018), steepen and eventually overturn breaking down into turbulent flow. This breakdown arises typically with in the lower stratosphere, or at the tropopause. This boundary, between the troposphere and stratosphere, is a region of enhanced turbulent mixing, with ozone, water vapour and aerosols exchanged between both layers (Whiteway et al.,2003; Lane et.al, 2009). This height is also a typical cruising altitude for the aircraft, a part of the flight in which passengers and on-board crew are more likely not to be wearing their seat belts (Kim et al., 2018). This type of upper level, aviation scale, turbulence is referred to as Mountain Wave Turbulence (MWT). MWT is the most significant mechanisms that impacts aircraft safety near mountains (Lane et al., 2009). All types of upper level atmospheric turbulence are dangerous and damaging phenomenons that have a serious and costly impact the aviation sector. Delays, injuries and fatalities have a huge economic loss worth millions of US dollars a year (Wolff and Sharman, 2008). An aircraft caught in a patch of turbulence has to quickly change altitude. This leads to substantial shift in airspeed, which increases the chance of a system stall (Sharman and Pearsons, 2017). Each branch of turbulence is defined by the mechanisms that it arose from, for example turbulence that develops in vertically deep (9-12km) convective cloud is referred to convectively induced turbulence (CIT) (Wolff and Sharman 2008). MWT, unlike CIT, is not detectable by on-board RADAR equipment (Sharman and Lane, 2016). Therefore flights can be struck suddenly which can lead to serious injuries and damages. Clear Air Turbulence (CAT), coined due to its formation without any convective features, is also not delectable. CAT often forms in the presence of an upper level frontal system, a jet core or jet stream. MWT is often included within CAT, due to its cloud-free, stratified development.

Global troposheric warming has an impact on the frequency of CAT production, with an increase across the North Atlantic and the world concluded in several studies (Williams and Joshi, 2013: Kim et al. 2023; Prosser et al., 2023; Storer et al. 2019 and Smith et al. 2023). Upper level jet streams are shifting in position, speed and momentum with global temperature gradients altered, resulting in an increase in CAT production. However, new areas of research are trying to quantify the impact of global warming on MWT. Any future change to MWT will be equated to a shift in low level wind speed or a change in upper-level dynamical features suppressing or energising the breaking of inertial gravity waves. Kim et al. (2023), using a high-end SSP climate scenario, investigated the change to

CAT, NCT and MWT between 1970-2014 and 2056-2101. Their paper used 14 different diagnostics to represent MWT within modelled data, with several indices and regions projecting an increase in the probability of encountering strong turbulence. The regions with a decline in MWT, had near-surface winds projected to also weaken in time. Observations have shown a global slowing in surface winds over previous decades, referred to in literature as terrestrial stilling (TS). Despite TS shifting with several modes of climate variability (Zeng et al, 2019), it is projected to continue in many areas of the globe, including the northern hemisphere (NH) mid latitudes, in both middle to high warming projections (Deng et al., 2022). Kim et al. (2023) overall found an increase in MWT over two thirds of the globe, with large variations over the tropical regions.

Aircraft encountering turbulence are required to record the time, location and severity of the event. These reports are referred to as PIREPs. PIREP datasets are effective for turbulent climatology research but are not always reliable in their location or timing (Gill,2018), with median uncertainties of around 50km horizontally, 70m vertically and 200s temporally out (Sharman et al., 2006). Many previous studies, investigating trends in atmospheric turbulence, have used global climate models (GCMs) over PIREPs. Williams ands Storer (2022) found GCMs can effectively represent turbulence in the atmosphere as well as re-analysis data. The latest phase of the Coupled Model Intercomparison Project (CMIP6) has a subsection of high resolution global climate models (HighResMIP). This subsection was developed to bridge the gap between numerical weather predictions grid spacing sizes and GCMs, and to investigate global meteorological dynamical processes in higher resolution (Haarsma et al., 2016; Smith, et al., 2023). This paper aims to understand if MWT is projected to change within CMIP6 HighResMIP models over a 101 year period starting in 1950 and ending in 2050. Kim et al. (2023) focused on change after 2056, which leaves a gap in scientific literature for MWT shifts in the next few decades, in which we aim to address. This paper also aims to understand if resolution is important for capturing MWT, if CMIP6 models project TS and if TS differences globally result in changes to MWT. A final aim is to understand seasonality variation in MWT changes. This paper briefly explains the methodology and results and a discussion in Section 5.3. It concludes and discusses future work in section 5.4.

5.2 Methodology and Data

Gill and Striling (2013) found MWT is difficult to forecast, with the theory very well understood, but capacity to resolve the wave-length of inertial gravity waves and the turbulent kinetic energy difficult due to its small scale nature. One can assume large scale eddies will eventually cascade down the inertial sub-range into micro-scale sizes and into turbulent kinetic energy (Lester 1993, Sharman and Lane, 2016). This assumption allows investigations to use data with a range of resolutions. CMIP was set up in the 1990s to evaluate, collate and improve GCMs. Simulations from three CMIP6-HighResMIP GCMs are used in this study. These GCMs are HadGEM3-GC3.1, with three grid spacing domains available (-HM ;25km, -MM;60km, -LL;135km), MPI-ESM1.2 with two domains (-XR; 34km, -HR; 67km) and EC-Earth with two domains (-3P-HR; 36km , -3P; 71km). The finer sub-models may start to resolve patches of turbulence, which are 60km wide and 1km deep (Sharman et al., 2014).

To diagnose regions of turbulence, a number of indices, linked closely to atmospheric instability, are run within our CMIP6 GCMs data. MWT and CAT share similarities in their formation, so previous literature has applied CAT indices to represent MWT in the atmosphere. Sharman and Pearsons (2017) and Kim et al., 2023 combine CAT diagnostics with certain surface and terrain variables to create an index that just diagnoses MWT;

$$Index_{MWT} = Index_{CAT} * Ds$$

Ds is the near-surface element. Within this paper, Ds = surface height (>200m) multiplied by both terrain gradient (>0.5 km m^{-1}) and surface wind speed. Sharman and Pearsons (2017) determined, through experimentation, that these three variables within Ds combined with a CAT diagnostics represented MWT effectively. Kim et al. (2023) tested using vertical velocity within Ds, instead of low-level wind speed, but found a poorer statistical evaluation. Terrain gradient is an important quantity with its association with linear gravity wave theory, and the wave of a gravity wave amplitude being proportional to the terrain slope magnitude (Wolff and Sharman, 2008). This method of calculating MWT was deemed skillful against PIREP data, in comparison to a orthographic gravity wave parameterisation scheme (Kim et al., 2018). In our study, we apply six indices used previously to diagnose the presence of CAT (Williams, Joshi (2014). These CAT indices are Horizontal temperature gradient (HTG), Frontogensis function (FF), the divergence of horizontal wind (DIV), upper level wind speed (WS), flow deformation (FD) and finally a combination of flow deformation and upper level wind speed (FDWS). Each MWT index is denoted with the subscript of their CAT index contributions, for example MWT_{HTG} is the product of Horizontal temperature Gradient and Ds.

Within the aviation sector, receiving operating curve (ROC) analysis is commonly used to verify an index, through curve comparisons between the probability of True and False detection of MWT or CAT in the atmosphere. The area under such curve (AUC) can range between 0.5 to 1, with 1 displaying no false detection. Sharman and Pearsons (2017) found that these 6 indices, with 8 others, are very well at representing MWT at high altitudes with AUC of 0.989. These 8 other indices are unfortunately not applied in this study due to limited vertical level data. Horizontal Temperature gradient (combined with Ds) also was found to pick up MWT effectively with an AUC of 0.991. These results have only been tested over the contiguous united states of America (CONUS). This study assumes moderate or greater (MOG) turbulence is arising globally at the 98th percentile value of each index, following recent MWT literature (Kim et al., 2023).

Low-level wind speed is a variable considered on its own within this paper. The variations in the maximum and median values in wind speed are investigated separately. This method was determined to understand on average how surface wind flow is changing, and if this change is also found in the high-end maximum wind flow.

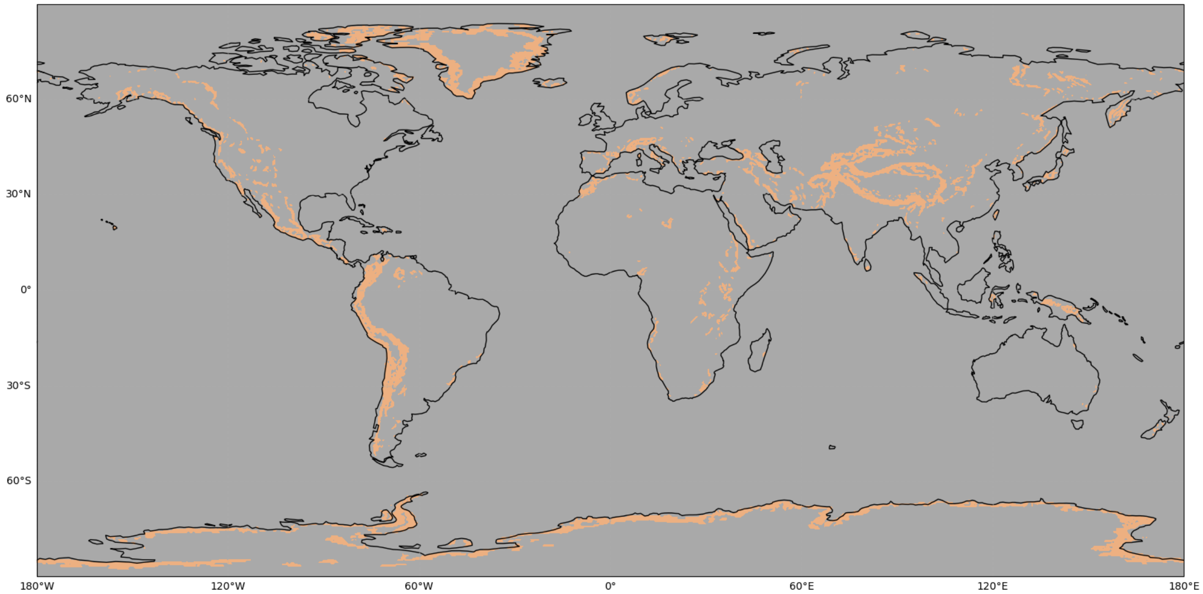

FIGURE 5.1: Areas of the globe in which our GCMs project MWT, averaged over three GCMs; HadGEM3-GC3.1-HM, MPI-ESM1.2-XR and EC-Earth-3P-HR, across all indices; MWT$_{FD}$, MWT$_{FDWS}$,MWT$_{WS}$, MWT$_{HTG}$, MWT$_{FF}$,MWT$_{DIV}$.

5.3 Results and Discussion

As discussed, terrain height and gradient are applied to CAT indices to identify MWT. The importance of terrain gradient is highlighted effectively in fig 5.1. This figure shows the regions of the globe where our indices diagnose MWT. Regions of the globe with large plateaus, such as Greenland and the Tibetan Plateau, are enclosed by areas of MWT with these steep slopes dominating. As expected, MWT is most prominent over large mountain ranges, such as the Andes, Rocky and Himalayas.

5.3.1 Two Decade Comparison

The MOG MWT decadal difference between 1950-60 and 2040-50 are displayed within fig 5.2 . Here this relative change in MWT is shown for all models domain sizes averaged across the six indices. A definitive lack of detail is evident within mid-range/coarser sub-models, clearly shown by HadGEM3-GC3.1-LL (fig 5.2i) with few MWT zones. Previous PIREP analysis suggests that there are considerable more regions where aircraft have experienced MWT, for example North America projected MWT is non-existent within this 135km grid spaced model. For MWT, a resolution dependence has arisen. Interestingly, the mid-range sub-models project similar MWT changes, when compared to their finer counterparts. This is shown effectively within subplots (5.2g) and (5.2h), which display the average across the models, regridded to 36km and 71km respectively. Both subplots have a separate steep increase or decrease over Greenland and northern South America. However, there are differences in the amount of "white" patches, which simply project "no-change" but the occurrence of MWT. The agreement across model resolutions, adds weight to the confidence in MWT projections, however, due to the increase detail in fine grid domain models, this paper progresses with the three finer models shown in fig 5.2.a, 5.2.c, 5.2.e.

Fig 5.3, 5.4 and 5.5 display the decade difference for HadGEM3-GC3.1-HM, EC-Earth-3P-HR and MPI-ESM1.2-XR individually, for each index, rather than averaged (fig 5.2). These figures also include the decade difference in daily maximum (g) and median (h) surface wind speeds. As mentioned in Section 2.0; Methodology and Data, low-level wind speed is a variable within our MWT indices. One area of investigation is to understand if a shift in MWT is linked to possible changes in surface winds. Deng et al. (2022), using different, coarser CMIP6 GCMs and observational data, found CMIP6 GCMs correctly reproduced the decreasing trends (between 1980-2010 and 2070-99) in near surface winds in North America, Europe and East Asia. They did on average simulate faster wind speeds at coastal areas than inland, and have shown seasonal variations. Please note these wind speed percentage change only displays results over regions in which MWT arises, other areas excluded for ease of comparison.

Within the HadGEM3-GC3.1-HM (25km) model, a general increase in maximum wind speed is apparent in fig 5.3.g, with a larger percentage change compared to the change in average surface wind speed (fig 5.3.h). The maximum surface winds have relatively large percentage shifts over Greenland, the Antarctic and

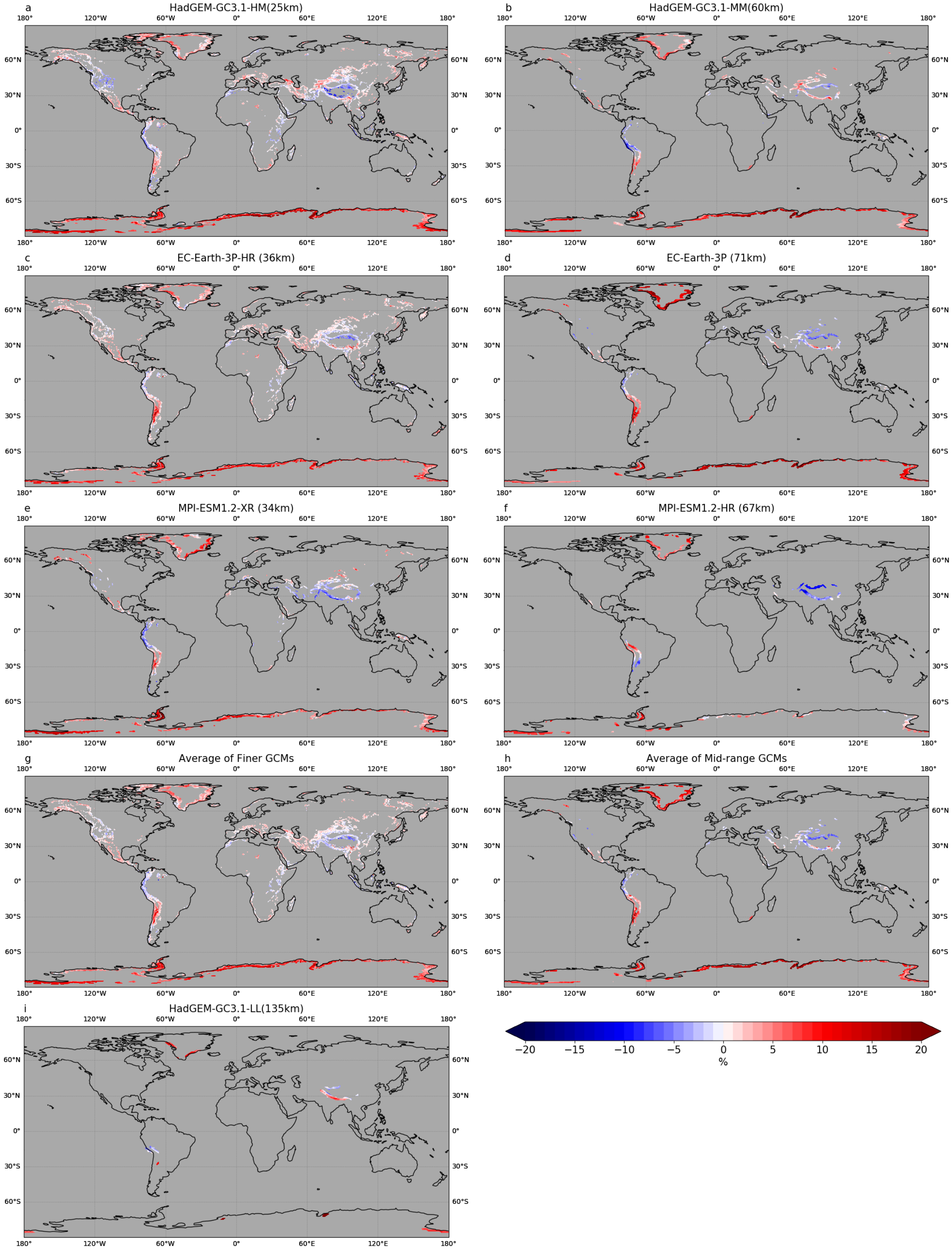

FIGURE 5.2: Decade difference in MWT between 1950-59 and 2040-49, for all seven resolutions; HadGEM3-GC3.1-HM 25km,-MM 60km (a,b),-LL 135km (i), EC-Earth-3P-HR 36km,-3P 71km (c,d)and MPI-ESM1.2-XR 34km, HR- 67km (e,f). Subplots g,h show average across finer and mid-range GCMs. Conservative regridding method, modifying data into 36km and 71km across the finer and mid-range domains.

Asia. These regional increases correlate the rise in MWT frequency in many indices within this figure. Interestingly, average wind speed has more regions that project decrease over the continents, than maximum wind speed, particularly interesting is the decline on the coastlines of the Antarctic between 60-180 °E. One could argue the changes in wind speed, in both maximum and average, correlate to projected MWT percentage differences in such indices as MWT$_{FD}$, MWT$_{FDWS}$,MWT$_{WS}$. Within this figure, the projected outcomes from these indices are relative similar within the HadGEM3-GC3.1-HM model.

Interestingly, MWT$_{DIV}$ (fig 5.3c) projects a very notable MWT decline across the globe, including southern Greenland, the North America Rocky, Central and Southern Andes and the Himalayas. A decline in maximum wind speeds arises over the Antarctic and north west Greenland, regions where MWT$_{DIV}$ projects a drop in MWT frequency between the two decades. MWT$_{HTG}$ (fig 5.3a) is an index shown to effectively represent MWT over North America, according to ROC curve analysis from Shaman and Pearson's (2017). This index projects either no change or a decline in MWT over southern Greenland, USA and Canada. Despite similarities to MWT$_{DIV}$, MWT$_{HTG}$ differs over the African and Asian contentment, with an increase in turbulence at the southern edge of the Tibetan Plateau. The most notable index within fig 5.3 is MWT$_{FF}$, with a pronounced decline projected over the northern Andes, eastern Africa, the Himalayas and Indonesia and a substantial increase projected in other regions of the globe. Except for similarities in North America, MWT_{FF} and MWT_{HTG} have almost opposite projections.

The EC-Earth-3P-HR (36km) and MPI-ESM1.2-XR (34km) too have the most notable change found within MWT_{FF}. These two models project a greater overall increase over Asia than HadGEM3-GC3.1-HM within this index. There is a notable drop in the number of regions producing MWT within MPI-ESM1.2-XR projections (fig 5.2c, fig 5.5). However, in comparison to the mid-range and coarser models, a large percentage of the globe is still incorporated. MWT_{DIV} within fig 5.5 projects a similar decrease to that evident in HadGEM3-GC3.1-HM (fig 5.3c) results, over the regions available. Interestingly, EC-Earth-3P-HR projects a decrease in some regions, using MWT_{DIV}, but a much smaller percentage change. In some cases MWT_{DIV} project a slight increase in areas which decreased in fig 5.3 (North/South America). Despite these difference, these spatial maps from fig 5.3 to 5.5 suggest a greater variation in trends in the indices than GCMs.

The change in surface wind speed marginally differs across the GCMs. Although, EC-Earth-3P-HR compared to HadGEM3-GC3.1-HM projects weaker winds inland over Asia, Greenland and North America, for change in average wind speeds. MPI-ESM1.2-XR also projects weaker winds over Asia within fig 5.5 (h).

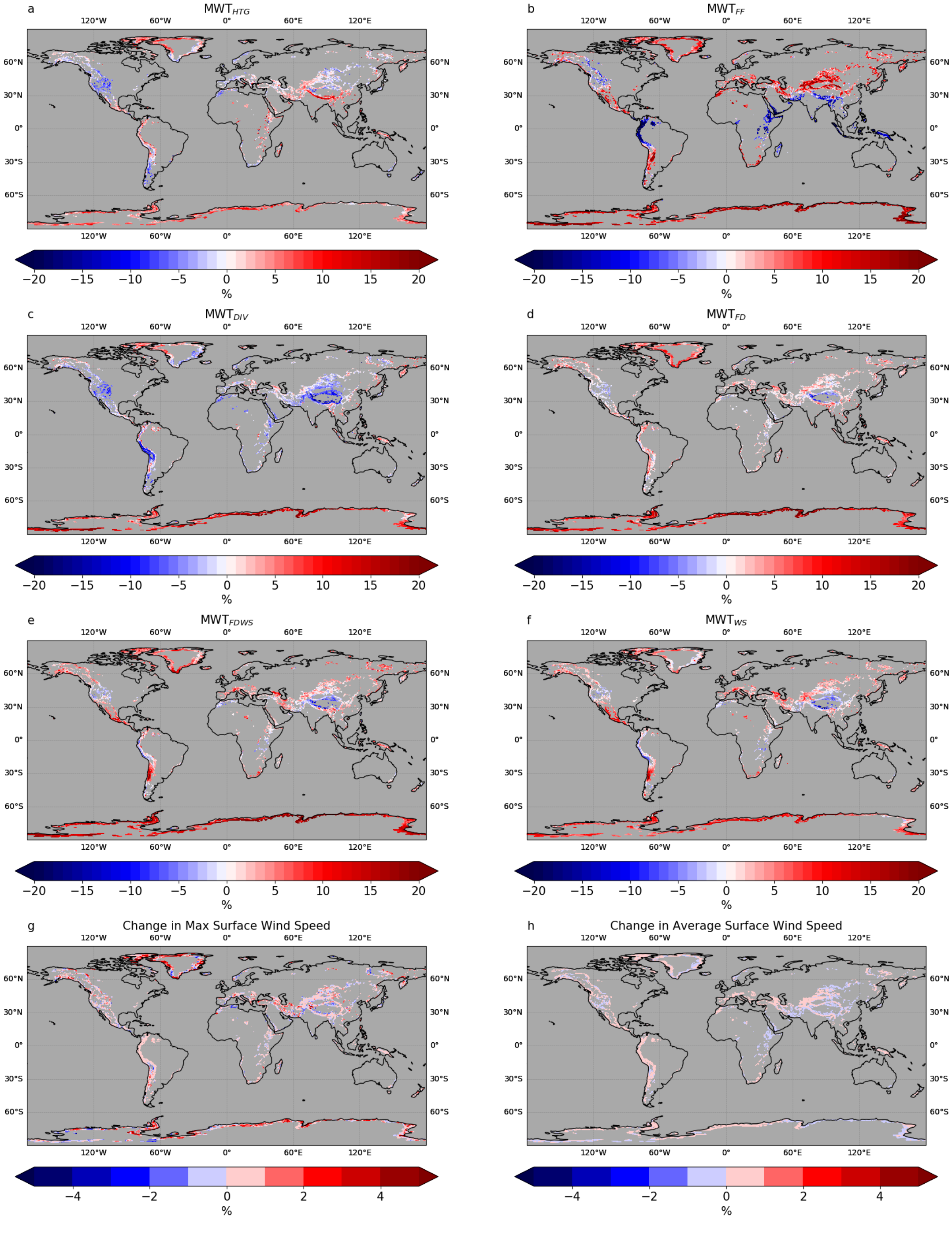

FIGURE 5.3: The decade percentage difference in MWT between 1950-59 and 2040-49, for the six MWT indices using the Met. Office Model HadGEM3-GC3.1-HM with grid spacing domain of 25km, averaged over three ensemble member runs (a-f). The change in maximum and median wind speed, between these two previous mentioned decades, within HadGEM3-GC3.1-HM is highlighted in subplots g and h respectively.

These differences highlight the impact of the average surface wind on MWT$_{FD}$, MWT$_{FDWS}$, MWT$_{WS}$ projections. These weaker winds link to negative changes in MWT, particularly over Asia. Overall, its evident surface wind changes do correlate to the projections, but not in all indices or locations. These results only address changes in two decades at the start and end of our 101 year period. To reduce decadal variability, analysis has been extended to annual results for the outlined period. Section 5.3.2 explores the yearly percentage change over the seven continents within each season.

5.3.2 Seasonality of MWT; yearly analysis

Due to the range of results from the decadal comparison, figure's 5.6-5.12 separately display indices individually. These results focus on the change each year in MWT compared to a global threshold for MOG (98 percentile) turbulence found using all years (and seasons) with the 1950-60 decade. Using a global threshold provides information on the most turbulent projected regions of the globe, most evident through analysis of the y-axis in all subplots in aforementioned figures. In order of most turbulent, Asia, South America, the Antarctic, North America, Africa, Europe and the Australian continent y-axes range from +75 to +275%, 0 to +250%, -50 to 250 %, 0 to +100%, -100 to +60%,-60 to 20% and -95 to -75% respectively. Interestingly, the larger spread highlights differences across the indices and

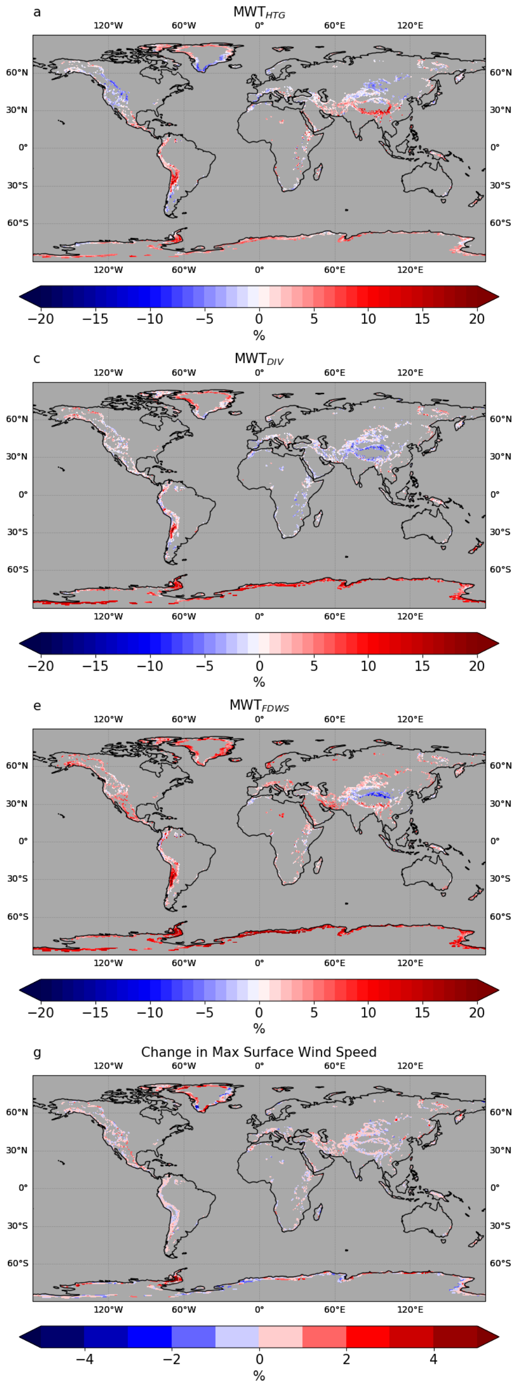

FIGURE 5.4: The decade percentage difference in MWT between 11950-59 and 2040-49, for the six MWT indices using EC-Earth-3P-HR with grid spacing domain of 36km, averaged over two ensemble member runs.

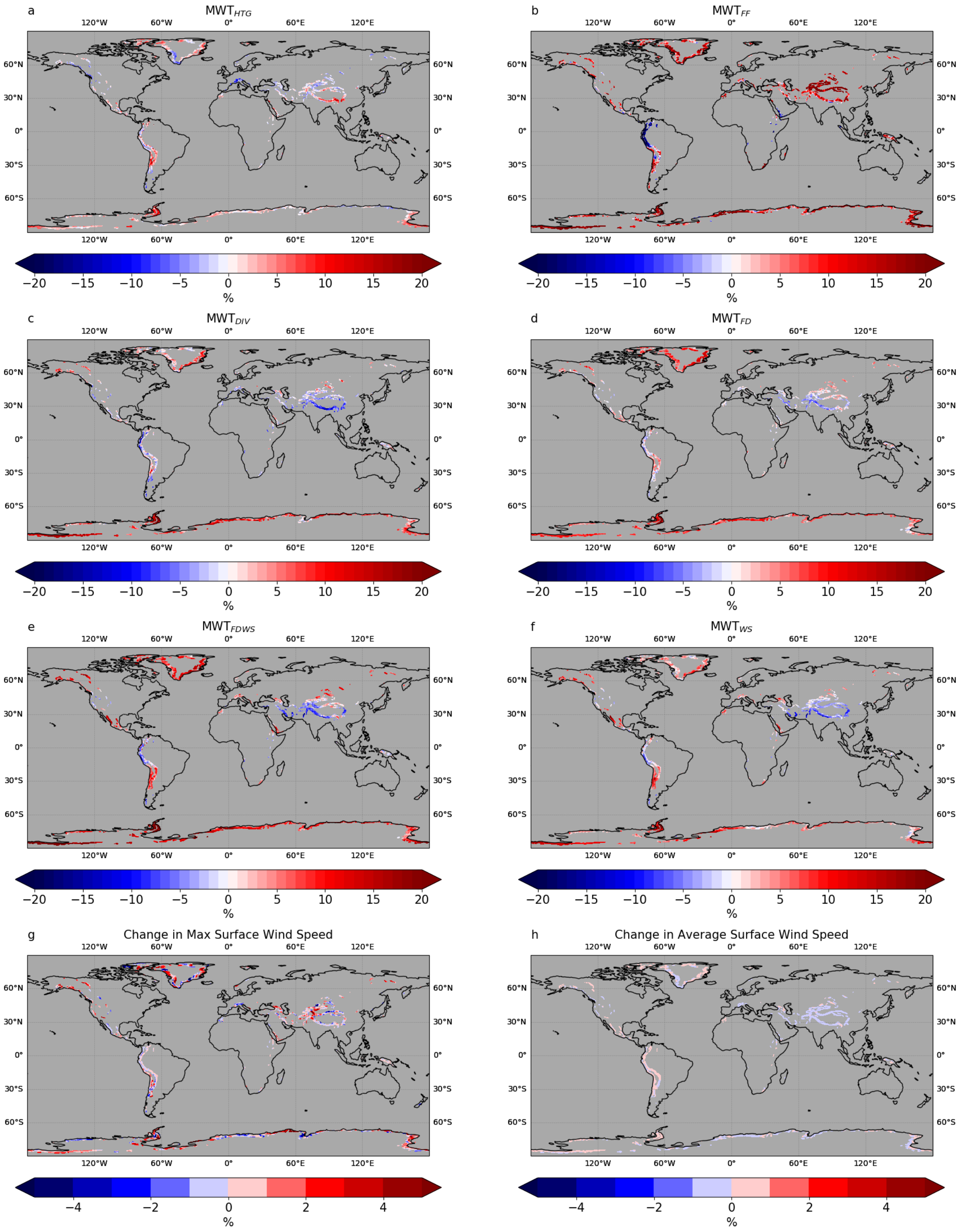

FIGURE 5.5: The decade percentage difference in MWT between 1950 and 2040-49 (2040-49-1950) for the six MWT indices using Max-Planck Institute GCM MPI-ESM1.2-XR with grid spacing domain of 34km.

the seasonality of MWT, with winters and summers in both hemispheres characterised with the maxima in MWT in majority of cases. The slopes of the linear regression lines, in fig 5.6 to 5.12 (and in section 5.3.3), are the percentage trend in time per year. However, averaging over an entire continent has lead to a wide spread of results, and in multiple cases has lead to slope errors greater than the absolute slope value. Implying, at a 95% confidence level, that time has no significant linear effect on MWT, with slopes not statistically distinguishable from zero. The percentage of significant trends in each figure is presented in Table 5.1 and 5.2, highlighting the variability within the models and lack of confidence in some GCMs. Averages within such tables only include significant slopes.

North America

This paper includes Greenland within North America. However, it should be noted that Greenland has large increases in MWT, evident in fig 5.2 to 5.5 and within Section 5.3.3 where it is discussed further. This may skew an increase in MWT within this sub section, with variability across North America previously shown. Seasonal difference in MWT amounts are evident in North America, with percentage changes in winter propagating at higher y-axis values within fig 5.6's HadGEM3-GC3.1 and EC-Earth-3P subplots. This is expected, with NH winter favourable for MWT generation over USA and Canada, with lowered tropopause heights and peak surface westerlies crossing mountain ranges perpendicularly (Guarino, et al. 2018). Fascinatingly, MPI-ESM1.2 has DJF (December, January, February) and SON (September, October, November) propagate at similar values in MWT$_{FD}$, MWT$_{FDWS}$, MWT$_{WS}$ within fig 5.6, with DJF at times below that of SON and other seasons. A double peak in maxima has been shown in some climatology MWT North America studies. Wolff and Sharman (2008), using PIREP data to find trends in MWT on the United States of America, found peaks in meteorological NH's winter and spring but not necessarily autumn.

A large number of insignificant trends arose across North America, with MWT$_{HTG}$'s annual, DJF, JJA (June, July, August) results projecting too much variability to definitive show any change in time any of the GCMs. A similar outcome for MWT$_{DIV}$, with only two slopes projecting a significant trend (EC-Earth-3P annual and HadGEM3-GC3.1-HM SON). Across this continent, only 44 lines, out of 90, project significant trend. Within Table 5. 1, the percentage of slopes, deemed to be significant, within North America are 61.11 %, 33.33 %, 22.22 %, 55.56 % and 72.22% across the entire year, DJF, MAM , JJA and SON respectively. Its evident that the overall annual value is brought up by the higher percentage of confident slopes in SON. Although within Table 5. 1, EC-Earth-3P-HR median in SON is 0.013 +/- 0.034 %/year. This large error occurs due to the range of confident trends, with MWT$_{FDWS}$ and MWT$_{HTG}$ projecting a significant decline but other indices projecting a rise in MWT frequency. Table 5. 1 further displays an overall average increase in MWT over North America, with only these two indices projecting negative slopes in NH autumn. These negatives are highlighted in the range row within Table 5. 1, with SON projecting a change of -4.3 to 16.3% over the 101 year period. Annual, DJF, MAM and JJA return similar ranges within the positive spectrum of 2.4 to 9.5 %, 3.7 to 13.0 %, 3.5 to 8.5% and 2.9% to 10.7%.

NH SON results, on average over the North America continent, have the largest high end positive increase in MWT with the greatest number of significant slopes and the greatest low end projected drop in MWT. On average, SON is projected to increase in MWT by 8.1% from 1950 to 2050. MAM, JJA, DJF and annual on average across this period project a rise by 7.2%, 7.0%, 6.4% and 3.3%, individually.

South America

The annual and seasonal percentage changes in MWT over South America are displayed in fig 5.7. The y-axis ranging from 0 to 250 %, highlights differences in diagnostics projections, with MWT$_{FF}$ projecting rates that are also found in Asia and the Antarctic (fig 5.10 & 5.12). In contracts, EC-Earth-3P-HR's MWT$_{FDWS}$ (fig 5.7.n) propagates at values are much smaller, similar to rates within Europe and Africa projections (Fig 5.8 & 5.9). Most other diagnostics propagate around

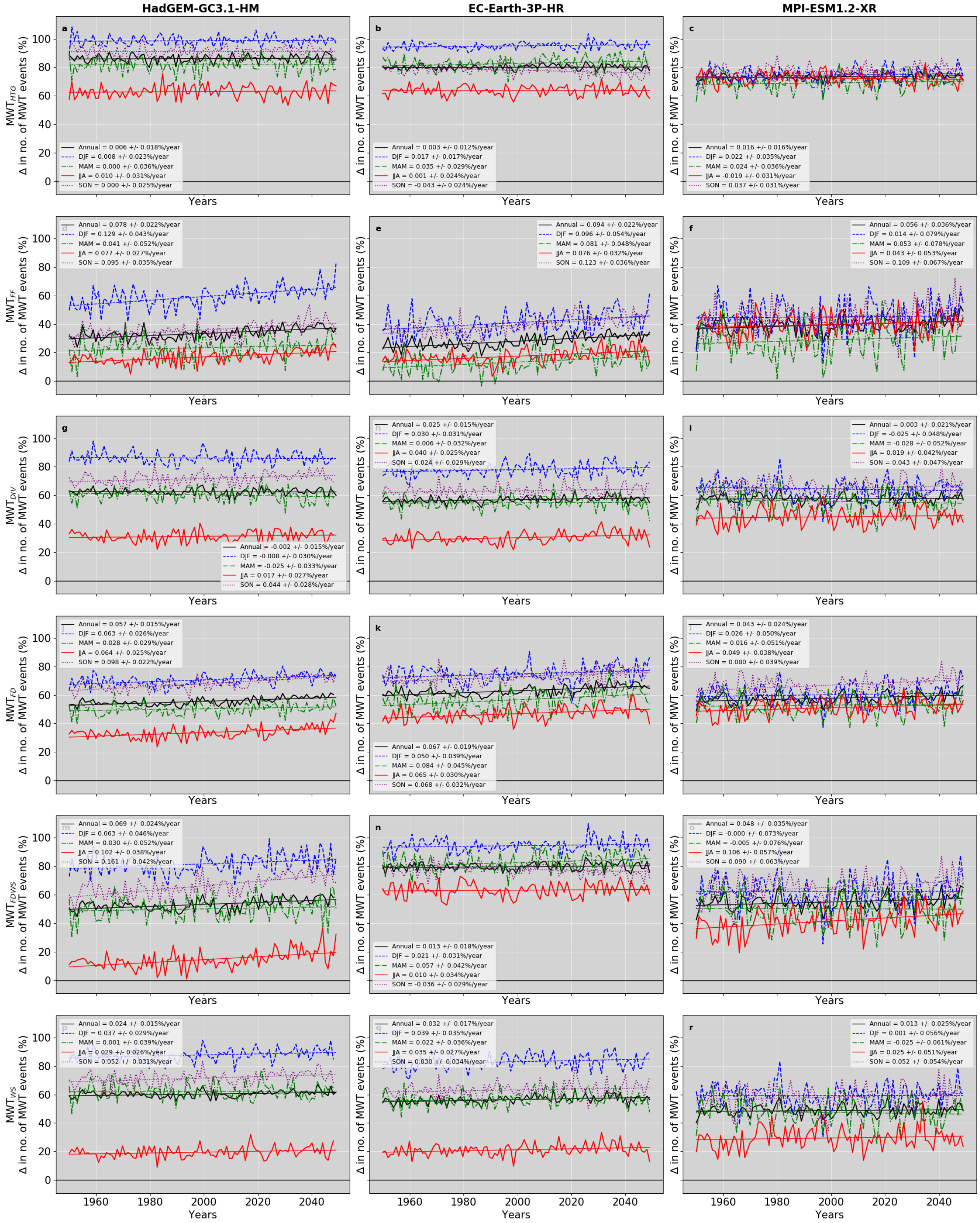

FIGURE 5.6: Line plots of relative percentage change over North America for each year and season compared to a 1950 decadal global references, for each GCM; HadGEM3-GC3.1-HM, EC-Earth-3P-HR, and MPI-ESM1.2-XR and for each individual index. Line colour and marking differ for each season, with DJF blue and dashed, MAM green and dash dotted, JJA red and soild, SON purple and dotted. Annual change, which includes all seasons is black and solid.

+100%, although there are clear seasonal variations, with SH winter the most turbulent season for all diagnostics, expect MWT$_{FF}$. In comparison to North America, South America projections have a higher number of significant slopes with 61/90 (67.7%). However, this rate is not evenly spread across the indices. Within fig 5.7, MWT$_{FD}$ only has five (out of 15) significant trends, with three in MPI-ESM1.2-XR (annual, DJF and JJA) and two in HadGEM3-GC3.1-HM (JJA and SON). Within JJA, MWT$_{FDWS}$, MWT$_{WS}$ and MWT$_{HTG}$ only have one model each projecting a significant trend. Within Table 5. 1, DJF and annual have a much higher percentage of confident slopes, with 83.3 and 88.9%.

The average over all GCMs across the South America, displayed with Table 5. 1, are interestingly dominated by negatively sloped projections. This suggests a decline in MWT over the period. However, EC-Earth-3P-HR projections often counter this with a rise in MWT frequency. If all three GCMs produced a similar trend (a) and had all indices agreeing, with a high number of significant slopes (b), theoretical weight would be added to the projected outcome. Despite several indices having two or three GCMs meeting condition b), condition a) is met less often in this continent. HadGEM3-GC3.1-HM and MPI-ESM1.2 suggests a decline in MWT in most indices over all seasons and annually in South America. Although there are four positive slopes in the Met. Office Hadley centre model (HadGEM3-GC3.1-HM), for MWT$_{FD}$'s JJA and SON and MWT$_{FF}$'s MAM and JJA projections. All indices in the EC-Earth GCM project an increase in MWT apart from MWT$_{WS}$ which displays a decline annually, in DJF and JJA. Section 3.1 determined the largest differences in results between the indices, rather than GCMs. Here a regional dependency is introduced, with South America having larger model disagreement rather than index variation.

Europe

Fig 5.8's results, which show the change in MWT compared to a global threshold over Europe, propagate below the zero-y-axis line for the majority of the period. This means that this region of the globe has less MWT within the GCMs than the global average. However, DJF values, in many indices, crosses into positive percentage changes, making it a more turbulent season. Interestingly, EC-Earth-3P-HR's MWT$_{HTG}$ and MWT$_{FDWS}$ have spring at a similar propagating level. Almost all MWT$_{HTG}$ lines are significantly sloped, but one in JJA. Overall, this index projects a decline in MWT in all seasons, at most by -0.177%/year in SON, a decrease of 18% over the period. MWT$_{DIV}$, also projects a decline but DJF or MAM cannot be included in overall analysis with considerable slope error.

However, MWT$_{FF}$, MWT$_{FD}$ and MWT$_{WS}$ all project an increase in their significant slopes. The remaining index, MWT$_{FDWS}$, has opposing signs across GCMs

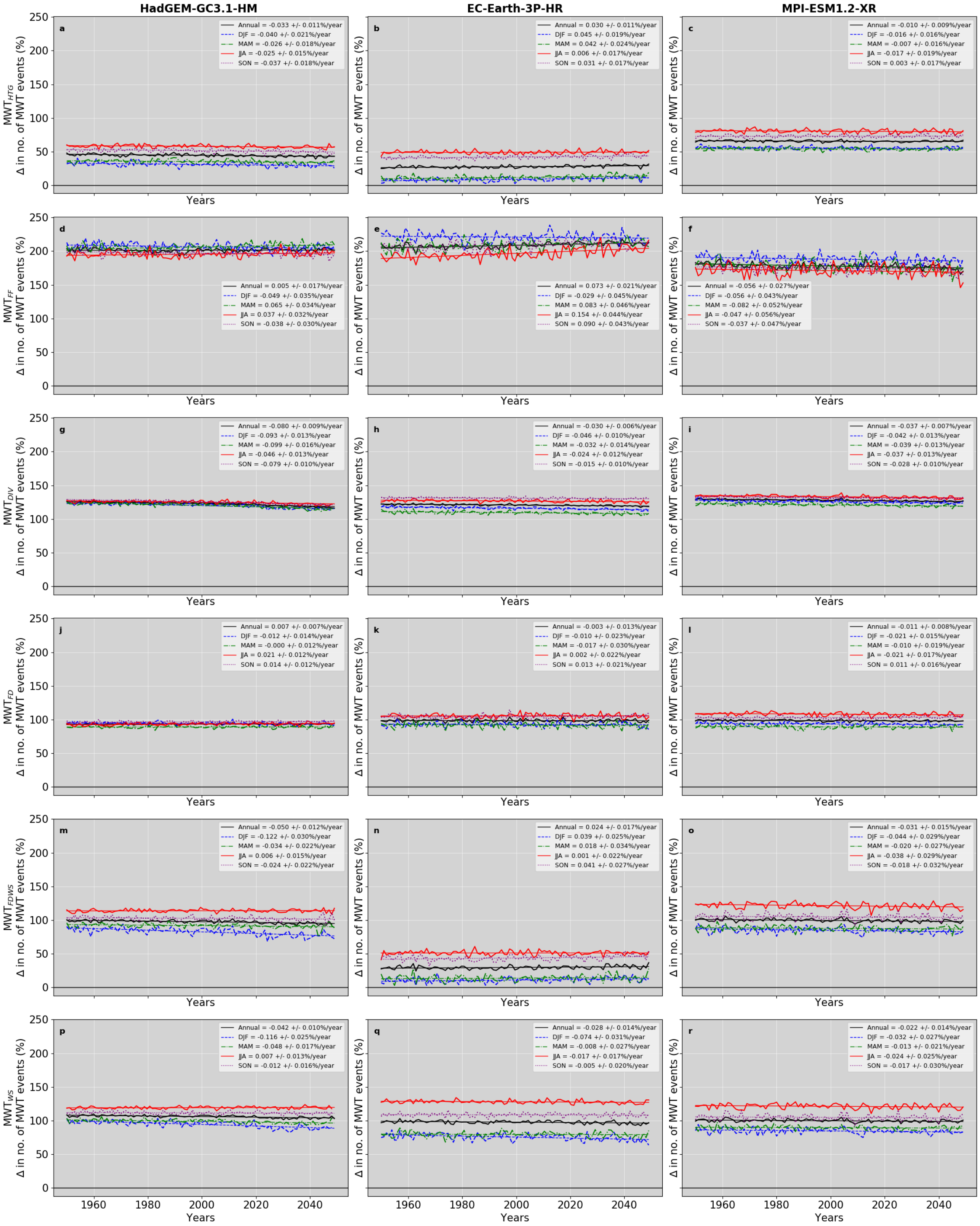

FIGURE 5.7: Line plots of relative percentage change over South America for each year and season compared to a 1950 decadal global references, for each GCM; HadGEM3-GC3.1-HM, EC-Earth-3P-HR, and MPI-ESM1.2-XR and for each individual index. Line colour and marking differ for each season, with DJF blue and dashed, MAM green and dash dotted, JJA red and soild, SON purple and dotted. Annual change, which includes all seasons is black and solid.

with HadGEM3-GC3.1 suggesting an increase with the previous three indices and EC-Earth-3P-HR projecting a reduction in MWT. MPI-ESM1.2 has no significant slopes within this index. As evident from Table 5. 1, when averaging across this figure, DJF, MAM and annual project an increase of 0.043, 0.057 and 0.039 %/year. An almost opposite response apparent in SON, with -0.045 % per year. JJA has too much variability to show any clear response. Like South America, Europe did not meet condition a) but it also did not meet condition b), with large variations across both models and indices, suggesting a less confident response.

Africa

Fig 5.9 displays the percentage change in MWT over the African continent. The most notable result within this figure is the level on the y-axis that HadGEM3-GC3.1's MWT_{FF} lines propagate at. This height on the y-axis is comparable with the amount of turbulence over North America. This index previously projected relatively large percentage changes, compared to the other five indices, in section 3.2.2 over South America. Most indices in Africa reside in the negative spectrum, with the amount of MWT turbulence similar to Europe or below. One index of interest, when considering the trend of the data, is MWT_{DIV}. All three GCMs agree, all with significant slopes, that MWT, diagnosed by MWT_{DIV}, is decreasing over Africa in all seasons. The remaining 5 indices do not have all three GCMs

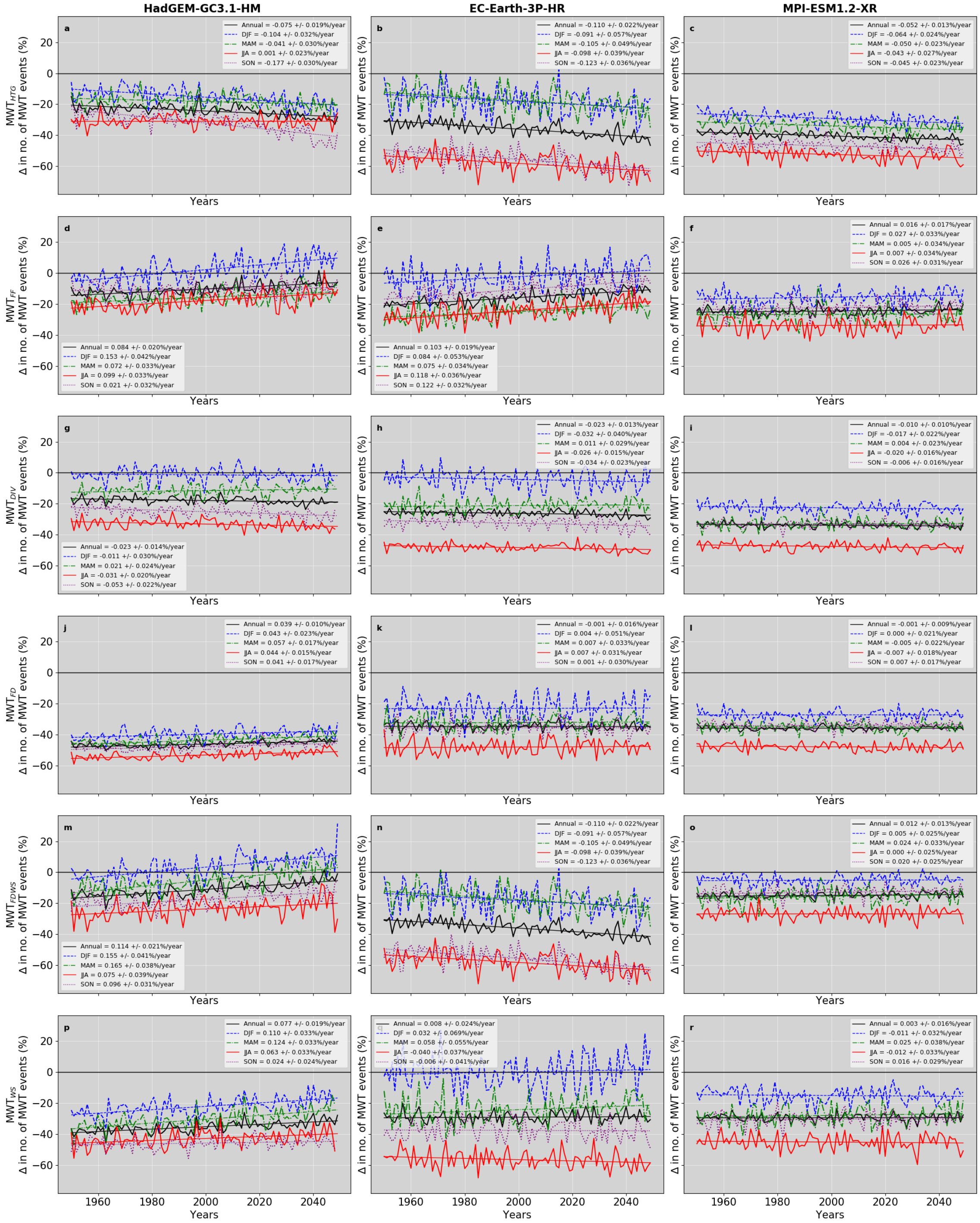

FIGURE 5.8: Line plots of relative percentage change over Europe for each year and season compared to a 1950 decadal global references, for each GCM; HadGEM3-GC3.1-HM, EC-Earth-3P-HR, and MPI-ESM1.2-XR and for each index. Line colour and marking differ for each season, with DJF blue and dashed, MAM green and dash dotted, JJA red and soild, SON purple and dotted. Annual change, which includes all seasons is black and solid.

producing significant slopes or have them agreeing on a trend. There are multiple indices that do agree with the decline in JJA, SON, DJF and annually, as seen by the overall average decrease in such seasons in Table 5.1. However, MAM has a wide range of significant slopes, and overall ends up projecting a positive trend of 1% over the 101 years.

Asia

Due to the Himalayan Mountains and many other steep mountain ranges over Asia, the MWT percentages on the y-axis in fig 5.10 are the largest compared to any other continent. The seasonality of MWT is very interesting over Asia, with different indices projecting MAM, JJA or DJF to have the maxima in MWT across their retrospective subplots. In section 3.3, regional analysis should help further understanding on the mix of seasonal maximums. Interestingly, MWT_{FF} again projects the largest percentage change ranges within fig 5.10 . In this case many other indices are propagating at a percentage value near or just below this index, adding confidence in the high amount of MWT over Asia.

As shown by slopes in fig 5.10 and Table 5.2, there is a mix in projected trends for MAM and SON. Within MAM results, MWT_{HTG} and MWT_{DIV} generally projecting a decrease, and MWT_{FF}, MWT_{FD}, MWT_{FDWS} and MWT_{WS} suggesting an increase. MWT_{FF} large slopes of +0.126, +0.193 and +0.072 shift the tug of war

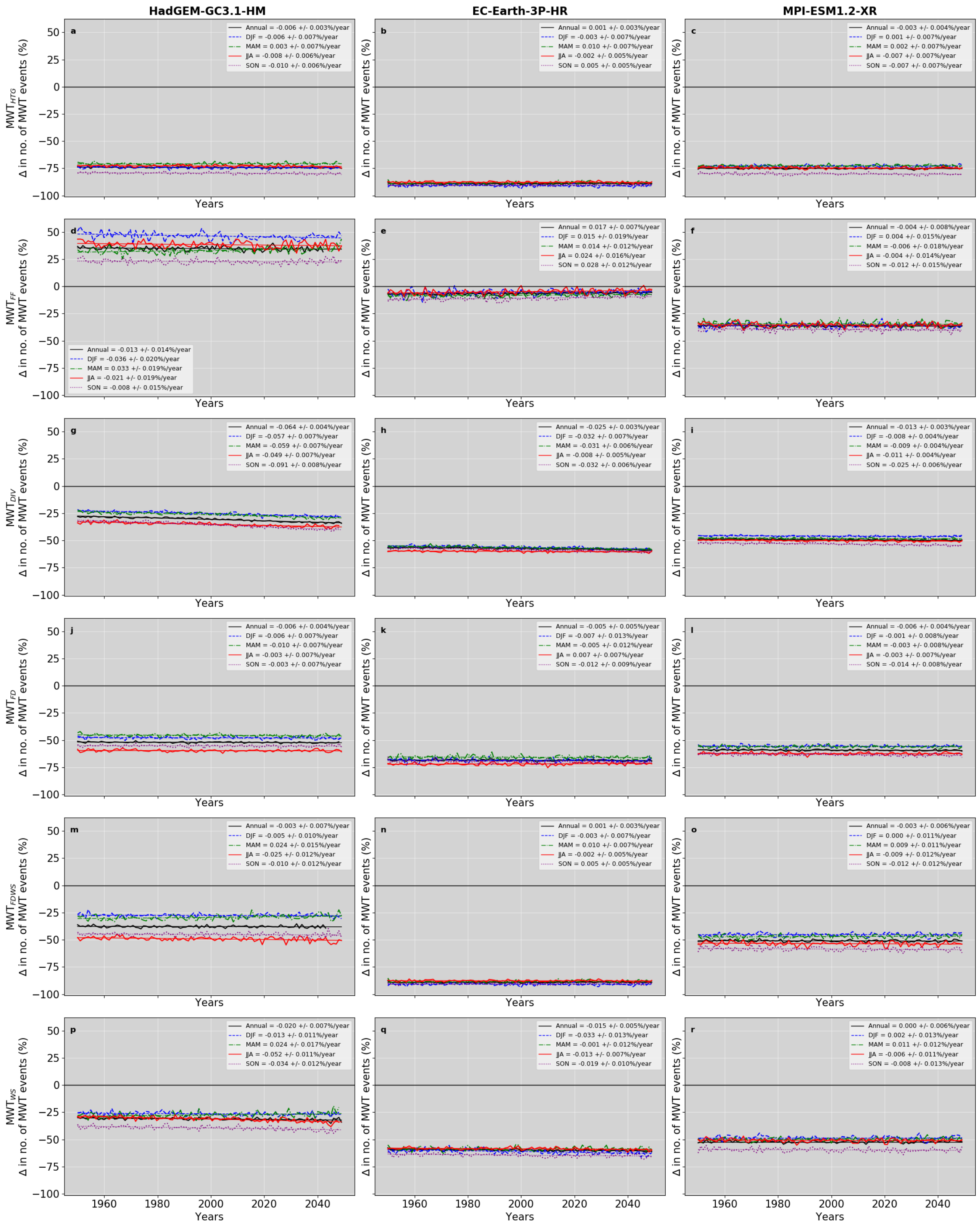

FIGURE 5.9: Line plots of relative percentage change over Africa for each year and individual season compared to a 1950 decadal global references, for each GCM; HadGEM3-GC3.1-HM, EC-Earth-3P-HR, and MPI-ESM1.2-XR and for each index. Line colour and marking differ for each season, with DJF blue and dashed, MAM green and dash dotted, JJA red and soild, SON purple and dotted. Annual change, which includes all seasons is black and solid.

		North America	South America	Europe	Africa
Yearly	Slope Median	0.033 +/- 0.019	-0.015 +/- 0.010	0.039 +/- 0.020	-0.012 +/- 0.005
	Had Median	0.063 +/- 0.018	-0.042 +/- 0.010	0.058 +/- 0.019	-0.013 +/- 0.004
	EC Median	0.050 +/- 0.018	0.024 +/- 0.014	-0.066 +/- 0.021	-0.015 +/- 0.005
	MPI Median	0.028 +/- 0.021	-0.014 +/- 0.008	0.045 +/- 0.029	-0.012 +/- 0.006
	Range	0.024 +/- 0.015	-0.080 +/- 0.009	-0.110 +/- 0.022	-0.064 +/- 0.004
		to 0.094 +/- 0.022	to 0.073 +/- 0.021	to 0.114 +/- 0.021	to 0.017 +/- 0.007
	Sig (%)	61.11	88.89	72.22	55.56
	no.pos , no. neg	11 , 0	4, 12	8, 5	1, 9
DJF	Slope Median	0.063 +/- 0.041	-0.044 +/- 0.025	0.043 +/- 0.041	-0.032 +/- 0.009
	Had Median	0.063 +/- 0.036	-0.093 +/- 0.025	0.110 +/- 0.033	-0.036 +/- 0.011
	EC Median	0.073 +/- 0.046	-0.002 +/- 0.024	-0.091 +/- 0.057	-0.032 +/- 0.010
	MPI Median	NA	-0.037 +/- 0.021	-0.064 +/- 0.024	-0.008 +/- 0.004
	Range	0.037 +/- 0.029	-0.122 +/- 0.030	-0.104 +/- 0.032	-0.057 +/- 0.007
		to 0.129 +/- 0.043	to 0.045 +/- 0.019	to 0.155 +/- 0.041	to -0.008 +/- 0.004
	Sig (%)	33.33	83.33	50.00	33.33
	no.pos, no. neg	6, 0	2, 13	5, 4	0, 6
MAM	Slope Median	0.071 +/- 0.047	-0.033 +/- 0.020	0.057 +/- 0.034	0.010 +/- 0.007
	Had Median	NA	-0.034 +/- 0.018	0.072 +/- 0.033	0.024 +/- 0.015
	EC Median	0.071 +/- 0.047	0.042 +/- 0.024	-0.024 +/- 0.049	0.010 +/- 0.007
	MPI Median	NA	-0.060 +/- 0.032	-0.050 +/- 0.023	-0.009 +/- 0.004
	Range	0.035 +/- 0.029	-0.099 +/- 0.016	-0.105 +/- 0.049	-0.059 +/- 0.007
		to 0.084 +/- 0.047	to 0.083 +/- 0.046	to 0.165 +/- 0.038	to 0.033 +/- 0.019
	Sig (%)	22.22	55.56	55.56	55.56
	no.pos, no. neg	4, 0	3, 7	6, 4	6, 4
JJA	Slope Median	0.069 +/- 0.032	-0.023 +/- 0.016	-0.023 +/- 0.033	-0.012 +/- 0.007
	Had Median	0.070 +/- 0.026	-0.002 +/- 0.014	0.063 +/- 0.033	-0.025 +/- 0.011
	EC Median	0.057 +/- 0.032	-0.019 +/- 0.018	-0.040 +/- 0.037	-0.008 +/- 0.007
	MPI Median	0.077 +/- 0.047	-0.037 +/- 0.017	-0.032 +/- 0.021	-0.009 +/- 0.006
	Range	0.029 +/- 0.026	-0.046 +/- 0.013	-0.098 +/- 0.039	-0.052 +/- 0.011
		to 0.106 +/- 0.057	to 0.154 +/- 0.044	to 0.118 +/- 0.036	t o 0.024 +/- 0.016
	Sig (%)	55.56	55.56	66.67	55.56
	no.pos, no. neg	10, 0	3, 7	5, 7	1, 9
SON	Slope Median	0.080 +/- 0.035	-0.019 +/- 0.018	-0.045 +/- 0.030	-0.016 +/- 0.008
	Had Median	0.095 +/- 0.031	-0.037 +/- 0.018	-0.006 +/- 0.026	-0.034 +/- 0.008
	EC Median	0.013 +/- 0.034	0.036 +/- 0.024	-0.078 +/- 0.034	-0.015 +/- 0.009
	MPI Median	0.085 +/- 0.051	-0.028 +/- 0.010	-0.045 +/- 0.023	-0.014 +/- 0.007
	Range	-0.043 +/- 0.033	-0.079 +/- 0.010	-0.177 +/- 0.030	-0.091 +/- 0.008
		to 0.161 +/- 0.042	to 0.090 +/- 0.043	to 0.122 +/- 0.032	to 0.028 +/- 0.012
	Sig (%)	72.22	55.56	50.00	55.56
	no.pos, no. neg	11, 2	4, 6	3, 6	1, 9

TABLE 5.1: Seasonal and annual median slope values from fig 5.6 to 5.9 across each GCM with HadGEM3-GC3.1-HM referenced as "Had", EC-Earth-3P-HR as "EC" and MPI-ESM1.2-XR as "MPI". "Range" displays the spread across all significant slopes over GCMs. "Sig" displays the percentage of slopes for each season with significant slopes. "no. pos, no. neg" values indicating the number of significant positive or negative slopes.

between the indices and suggest an overall increase in MAM. In SON, despite MWT_{FF} producing slopes of +0.23, +0.25 and +0.11%/year, MWT_{DIV} negative tilts of -0.143,0.123 and -0.043%/year, combined with negative results from other indices, produces a median within Table 5. 2 of -0.055 %/year. Within DJF and JJA, most slopes project an increase and a decrease in MWT, respectively. Over the 101-year period, DJF over Asia is projected to increase on average by +7 %, and at maximum by +30.9 % (MWT_{FF}, HadGEM3-GC3.1-HM). Interestingly, only 50% of DJF and JJA lines within fig 5.10, have significant trends. A larger percentage is evident in MAM and SON.

Australian Continent

A strong seasonal gap arose in the slopes over the Australian continent within fig 5.11, with a clear decrease in MWT over DJF and MAM (summer and autumn) and an evident increase for JJA and SON (winter and spring). The conditions of a) having all GCMs and b) all indices agreeing has been mostly met by this continent. JJA has all GCMs and indices producing significant trends, all projecting an increase. As displayed within Table 5.2, the average increase is of around +1.4 % with a maximum +4.4 % and minimum of +0.6 % over the 101 year period. SON also had a very similar agreement and trend but a lower number of significant slopes, at 72.22 % across fig 5.11. In terms of amount of turbulence, compared to

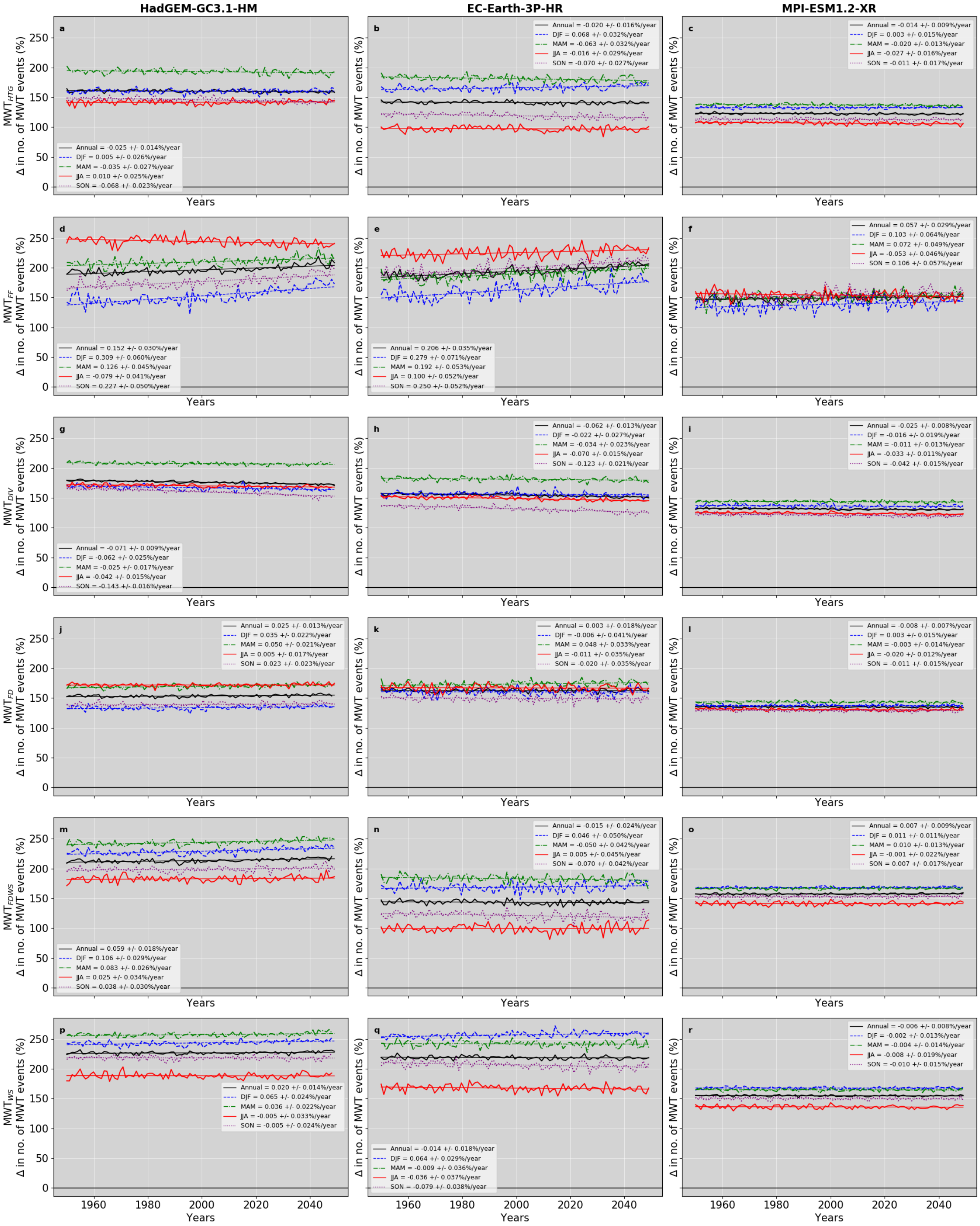

FIGURE 5.10: Line plots of relative percentage change over the Asian continent for each year and season compared to a 1950 decadal global references, for each GCM; HadGEM3-GC3.1-HM, EC-Earth-3P-HR, and MPI-ESM1.2-XR and for each individual index. Line colour and marking differ for each season, with DJF blue and dashed, MAM green and dash dotted, JJA red and soild, SON purple and dotted. Annual change, which includes all seasons is black and solid.

the other six continents, the y-axis is at its most negative on average, with a much smaller range. In terms of which season is on general most turbulent, in regards to MWT, JJA, SON and DJF are all at one point projected to have the largest amount of turbulence in at least one GCM and index.

Antarctic

There is a clear seasonality in the amount of MWT over the Antarctic, with SH winter and summer being the most and least turbulent season. The large JJA (winter) values in fig 5.12 place this continent second, after Asia, with the amount of projected MWT with the GCMs. Within this figure, only 6 projections suggest a decline in MWT within this region. There are 3 lines in JJA and 3 lines in SON across MWT_{HTG} and MWT_{FDWS} projections that show this decrease in MWT over the period. Despite this, there is quite strong model and index agreement, with all other indices, across all GCMs, projecting a significant increase in MWT. DJF on average projected a rise of +32% compared to the amount in 1950. JJA, the most turbulent season, had an increase of +8.7%. Few airlines travel over the Antarctic, but this result does put those few airlines at risk travelling, particularly in SH summer.

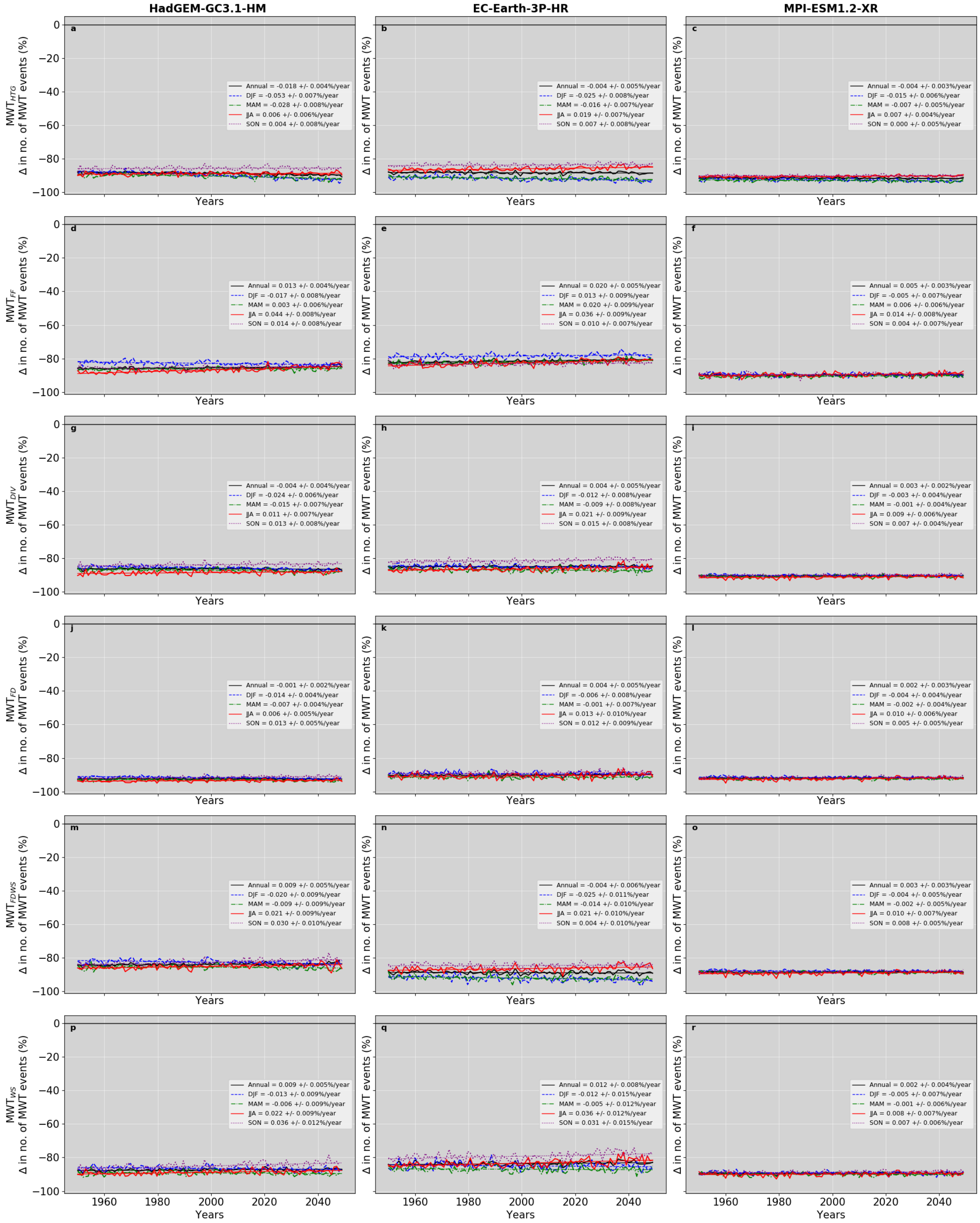

FIGURE 5.11: Line plots of relative percentage change over the Australian continent for each year and season compared to a 1950 decadal global references, for each GCM; HadGEM3-GC3.1-HM, EC-Earth-3P-HR, and MPI-ESM1.2-XR and for each individual index. Line colour and marking differ for each season, with DJF blue and dashed, MAM green and dash dotted, JJA red and solid, SON purple and dotted. Annual change, which includes all seasons is black and solid.

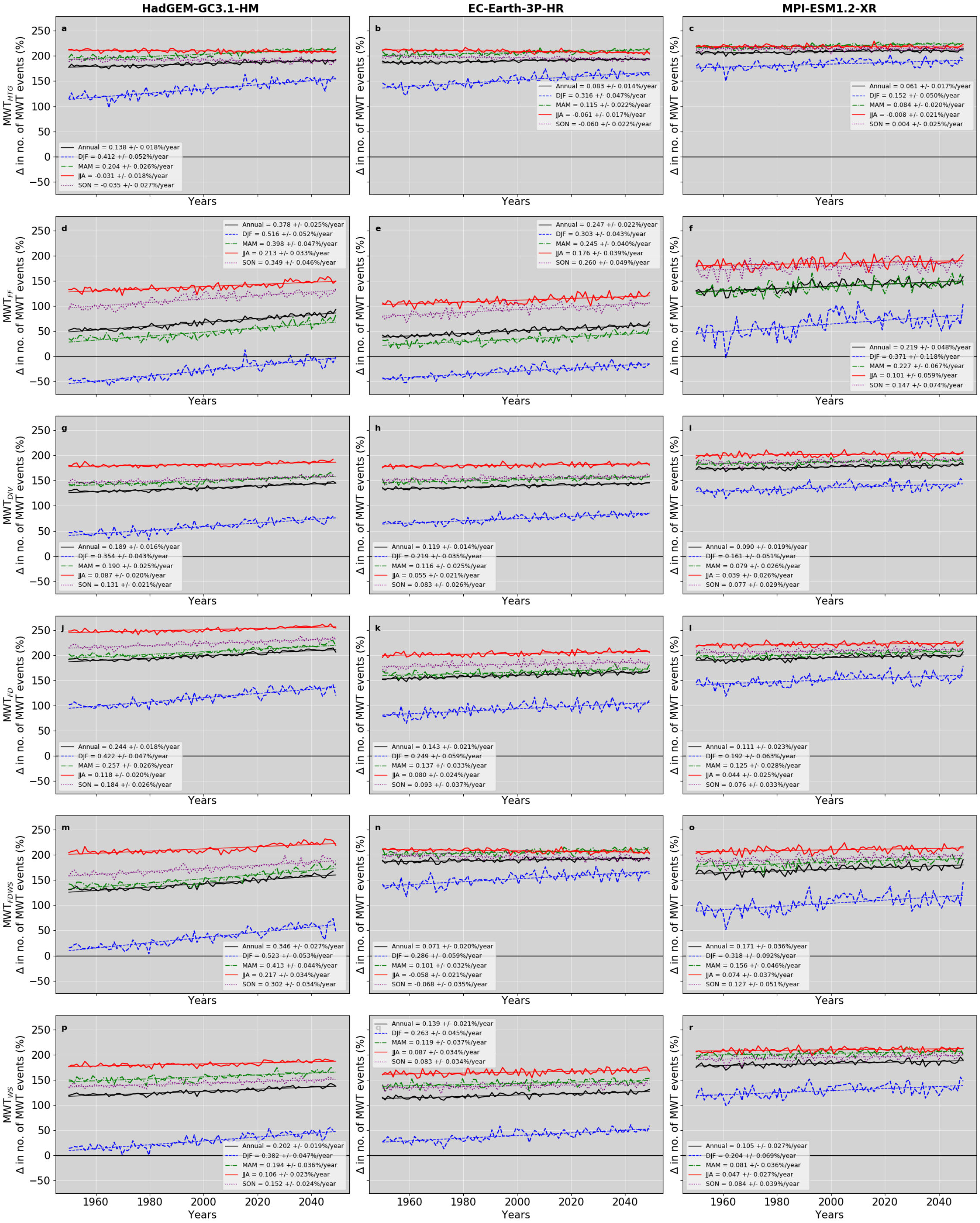

FIGURE 5.12: Line plots of relative percentage change over the Antarctic for each year and season compared to a 1950 decadal global references, for each GCM; HadGEM3-GC3.1-HM, EC-Earth-3P-HR, and MPI-ESM1.2-XR and for each individual index. Line colour and marking differ for each season, with DJF blue and dashed, MAM green and dash dotted, JJA red and soild, SON purple and dotted. Annual change, which includes all seasons is black and solid.

		Asia	Australia	Antarctic
Yearly	Slope Median	0.024 +/- 0.016	0.007 +/- 0.004	0.129 +/- 0.019
	Had Median	0.022 +/- 0.014	0.009 +/- 0.005	0.223 +/- 0.019
	EC Median	-0.020 +/- 0.016	0.016 +/- 0.006	0.129 +/- 0.021
	MPI Median	0.025 +/- 0.016	-0.002 +/- 0.002	0.084 +/- 0.019
	Range	-0.071 +/- 0.009	-0.018 +/- 0.004	0.046 +/- 0.014
		to 0.206 +/- 0.035	to 0.020 +/- 0.005	to 0.378 +/- 0.025
	Sig (%)	77.78	55.56	100.00
	no.pos, no. neg	9, 5	6, 4	18, 0
DJF	Slope Median	0.070 +/- 0.029	-0.018 +/- 0.008	0.317 +/- 0.051
	Had Median	0.065 +/- 0.025	-0.019 +/- 0.007	0.417 +/- 0.050
	EC Median	0.070 +/- 0.032	-0.018 +/- 0.009	0.289 +/- 0.046
	MPI Median	0.103 +/- 0.064	-0.015 +/- 0.006	0.198 +/- 0.066
	Range	-0.062 +/- 0.025	-0.053 +/- 0.007	0.152 +/- 0.050
		to 0.309 +/- 0.060	to 0.013 +/- 0.009	0.523 +/- 0.053
	Sig (%)	50.00	66.67	100.00
	no.pos, no. neg	8, 1	1, 11	18, 0
MAM	Slope Median	0.036 +/- 0.027	-0.009 +/- 0.008	0.149 +/- 0.032
	Had Median	0.043 +/- 0.024	-0.012 +/- 0.008	0.231 +/- 0.031
	EC Median	-0.034 +/- 0.032	-0.012 +/- 0.00	0.123 +/- 0.032
	MPI Median	0.026 +/- 0.031	-0.007 +/- 0.005	0.104 +/- 0.032
	Range	-0.063 +/- 0.032	-0.028 +/- 0.008	0.079 +/- 0.026
		to 0.192 +/- 0.053	to 0.020 +/- 0.009	to 0.413 +/- 0.044
	Sig (%)	72.22	50.00	100.00
	no.pos, no. neg	7, 6	1, 8	18, 0
JJA	Slope Median	-0.042 +/- 0.016	0.014 +/- 0.008	0.087 +/- 0.026
	Had Median	-0.061 +/- 0.028	0.016 +/- 0.008	0.112 +/- 0.022
	EC Median	-0.042 +/- 0.041	0.022 +/- 0.010	0.071 +/- 0.025
	MPI Median	-0.030 +/- 0.014	0.009 +/- 0.006	0.047 +/- 0.027
	Range	-0.079 +/- 0.041	0.006 +/- 0.005	-0.064 +/- 0.023
		to 0.100 +/- 0.052	to 0.044 +/- 0.008	to 0.217 +/- 0.034
	Sig (%)	50.00	100.00	94.44
	no.pos, no. neg	1, 8	18, 0	14, 3
SON	Slope Median	-0.055 +/- 0.029	0.013 +/- 0.008	0.104 +/- 0.034
	Had Median	0.023 +/- 0.023	0.014 +/- 0.008	0.168 +/- 0.026
	EC Median	-0.074 +/- 0.042	0.014 +/- 0.009	0.087 +/- 0.039
	MPI Median	0.032 +/- 0.036	0.007 +/- 0.005	0.084 +/- 0.039
	Range	-0.143 +/- 0.016	0.0049 +/- 0.0046	-0.074 +/- 0.040
		to 0.250 +/- 0.052	to 0.036 +/- 0.012	to 0.349 +/- 0.046
	Sig (%)	66.67	72.22	94.44
	no.pos, no. neg	5, 7	13, 0	14, 3

TABLE 5.2: Seasonal and annual median slope values from fig 5.6 to 5.9 across each GCM with HadGEM3-GC3.1-HM referenced as "Had", EC-Earth-3P-HR as "EC" and MPI-ESM1.2-XR as "MPI". The same rows as Table 5. 2, but with three final continents.

5.3.3 Further Regional Investigation

Section 5.3.1 highlighted sub-continental differences across the globe. Therefore, fig 5.13 and 5.14 focus on twenty-eight new smaller sub-continental areas of interest. Within these two figures results come from an average across indices which have a significant trend. In some cases all six indices within the GCM are projecting insignificant trends so the model is not considered or plotted. This is noticeable by the lack of scatter from some GCMs in fig 5.13 side plots and grey shaded blocks within fig 5.14. Similar to fig 5.2g, the spatial map in fig 5.13 is the 1950-59 to 2040-49 decade percentage difference averaged over the three finest GCMs, regridded on to the EC-Earth domain. However, if an index is not included in the scatter plots (insignificant) it has therefore been removed from each sub region in the spatial map, which averages across all GCMs and indices. However, when processing these figures, one should take care to note the spatial map in fig 5.13, which shows the decadal difference averaged across all seasons. If you break down the percentage change scatter in to each season (fig 5.14), differences in seasonal trends arise. Fig 5.14 breaks down the seasonal change for each region, averaged across the six MWT diagnostics.

The trends over a 101 year period are discussed below. Further analysis was done, focusing on a future 30 year period (2020-2050) but is not included within this section due to large decadal variability within findings. Interestingly in some cases significance shifted, with some trends previously showing a trend no longer applicable and vice versa. This shows that having an 101 year period more effectively encapsulates the MWT trends in time, with a 30 year periods linked to decadal variability.

North America; NA1-NA5

The North American continent is broken down into five regional areas. Region NA1 covers Greenland, Iceland and Canada north to north east of the Hudson bay. Aircraft are known to travel through this region, particularly over southern Greenland, when flying from Europe to North America and vice versa (Lane,2009). MWT formation over Greenland is often associated with the passage of a surface cyclone, due to progression of easterly or south easterly wind flow over the mountains terrain, with 40% of all significant turbulent events linked with this type of generation (Lane et al., 2009). As discussed in section 5.3.2, the percentage change is compared to a global average value of MOG MWT (dependent on index and model) and therefore percentage change on the y-axis of fig 5.13's scatter plots represents the amount of MWT in each region. NA1 is the second most turbulent region in North America. Greenland is a known turbulent region of the globe, with every fourth day having at least one MOG turbulent PIREP report (Lane et al, 2009). In terms of seasonality, literature suggest MWT frequency is similar

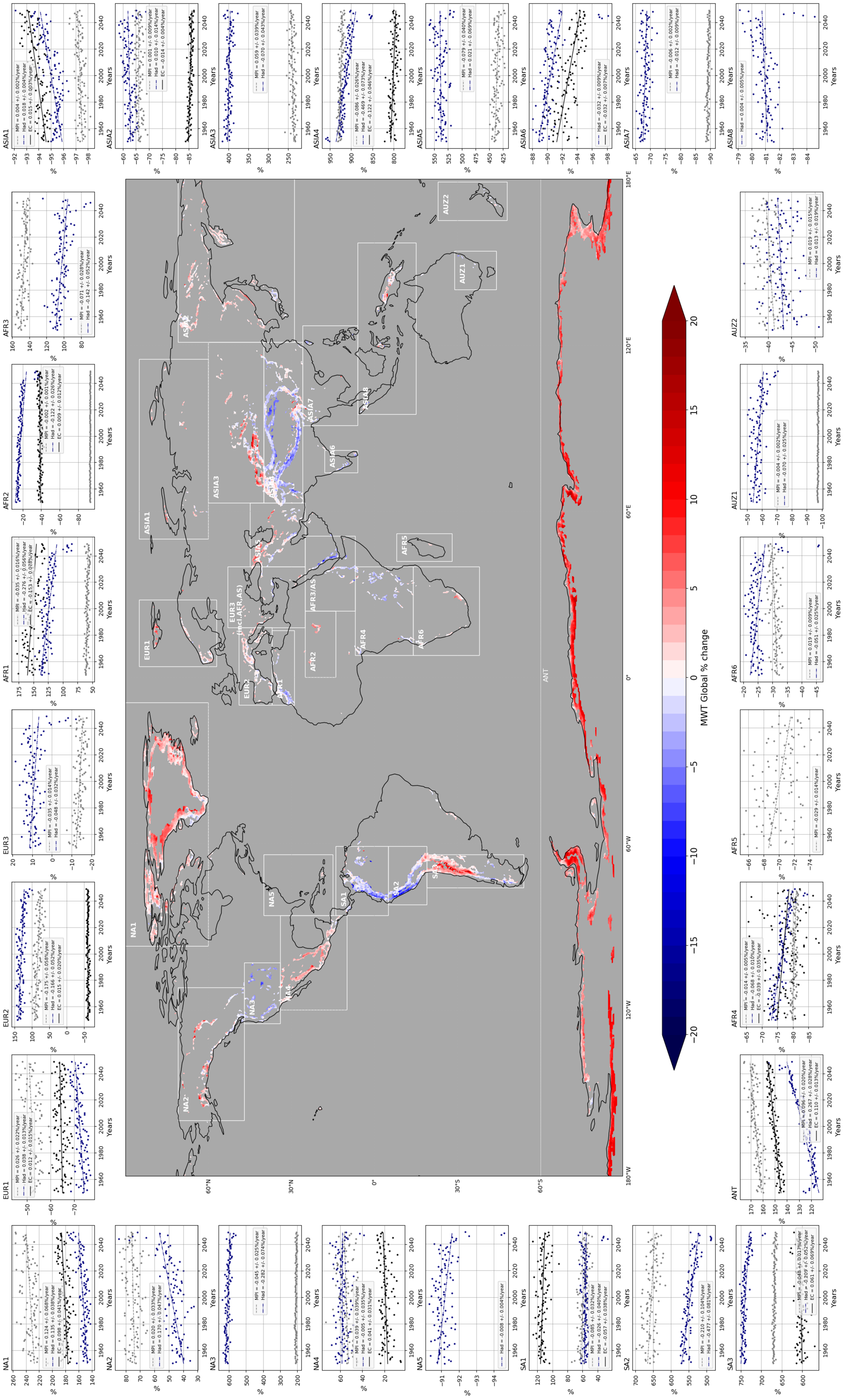
MWT Global % change
−20
−15
−10
−5
0
5
10
15
20
ASIA1
ASIA2
ASIA3
ASIA4
ASIA5
ASIA6
ASIA7
ASIA8
AFR1
AFR2
AFR3
AFR3/AS
AFR4
AFR5
AFR6
AUZ1
AUZ2
EUR1
EUR2
EUR3
(inc. AFR,AS)
NA1
NA2
NA3
NA4
NA5
SA1
SA2
SA3
ANT
60°N
30°N
0°
30°S
60°S
180°W
120°W
60°W
0°
60°E
120°E
180°E
Years
%

FIGURE 5.13: The spatial map displays the percentage difference between the 1950s and 2040s averaged across the three finer GCMs, similar to fig 5.2(g), but for each 28 regions. If indices are insignificant over a 101-year period, they are not included within area averaging. The line plots surrounding the map show the relative MWT percentage change from global threshold for each year, averaged over six MWT indices, for each new subregion shown by a white box. HadGEM3-GC3.1-HM linear regression slopes and scatter are referred to as "Had", as previously done in Table 5.1 and 2, and colored navy with a dash-dot line. MPI-ESM1.2-XR is referred to as "MPI" with a grey scatter and dashed linear regression line. EC-Earth-3P-HR is referred to as "EC" with black scatter and a solid line.

to contiguous United States (CONUS), where some winter months (January) have had rates four times the amount of MOG MWT compared to spring months (May) (Lane et al,2009, Wolff and Sharman 2008).

Interestingly, NH summer HadGEM3-GC3.1-HM projections had the greatest average increase of +58.4 % over the 101 year period within NA1 (fig 5.14). Once averaged over all GCMs that's an increase of +30.5 % between 1950 to 2050 for the summer season (JJA). NH autumn and spring project the same trend but at lower rates of +19.4 % and +18.0 % respectively. Interestingly, winter changes are more difficult to diagnose, with all indices projecting high inter-annual variability and insignificant trends , and therefore not included in fig 5.14 . Therefore, no definitive trends in MWT over NA1 in DJF. However, there are trends within surface winds speeds for NH winter between 1950 to 2050, evident in fig 5.15. Within this season, SON and MAM, an increase in median surface winds were projected, but weaker maximum wind speed. The evident increase in MWT frequency in SON and MAM could be linked to the average wind speeds, with increase evident in fig 5.15. However, the projected increase in MWT in JJA's, previously touched, within NA1 is not correlated to the surface wind speed changes, with a slight decline in median surface wind change for the HadGEM3-GC3.1-HM model. Only trends with significant slopes have been shown within fig 5.15, as done in the previous last two figures.

Within fig 5.13, regions NA2 and NA4 are clearly projected to increase over the 101 year period. Here one can also note projected insignificant sloped lines in the side scatter plots. Despite all indices projecting a confident trend, their trends range in both the negative and positive spectrum. This has led to an overall average uncertainty within the scatter. EC-Earth-3P-HR's indices did not produce significant trends to be included initially in NA2 region, but within a break down of seasonality, its clearly linked to the model projecting a drop in MWT in NH summer and increase in NH autumn. NA4 projections too have a seasonal difference, with a general increase in all seasons but SON. Over all GCMs NH winter, summer, spring and autumn MWT rates are projected to shift by +21.6 % , -1.4% , +12.4 % and +17.9 % within NA2 over 101 years and by +7.2 % , +1.6 % -10.5 % and +10.9 % within NA4, respectively. In terms of relationships to surface wind speed, within NA2, DJF and JJA median surface wind speed projections corolate to the same positive or negative shift found in MWT results. This is not the case for SON and MAM, with opposing trends. A similar outcome arose for NA4 in terms of the relationship between low-level wind speed shift and the change in seasonal MWT frequency.

NA3 encapsulates part of the Rocky Mountain range, and is the projected most turbulent (mountain generated) region of North America, with HadGEM3-GC3.1-HR data scattered at the 600% range. The Rocky Mountains are a well documented turbulent area (Wilms, Henrike 2020), with MWT the major source of turbulence over the western half of the USA (Wolff and Sharman,2008). Fig 5.13 and 5.14 show a decline for MWT over NA3 for all seasons but DJF (NH winter). EC-Earth-3P-HR DJF projections, averaged across significant indices, suggest an incredible slope of +1.64 %/year within this season. This steep slope is damped once averaged across GCMs, but overall they suggest an increase of 60.6% over the 101 years. NH summer, autumn and spring project a decrease of -58.3%, -30.9% and -41.2 % over the period within NA3. Interestingly, the median surface wind speeds in these seasons all project a decline. There is no evident trend within DJF surface winds (fig 5.15). This suggests a more turbulent future for the Rocky Mountain range within its current most turbulent season, but also a drop in the remaining three. Spring over this region, from climatology (Wolff and Sharman, 2008), can often have a peak in MWT similar to that in DJF. These results project a possible drop in this occurrence.

The last region in North America is NA5, which covers the southern states of the USA and the Caribbean. Within fig 5.1, it is evident that these southern USA states have pockets of MWT. However, once broken down into significant trends, these regions disappear. NA5 trends are therefore links purely to MWT over Haiti and the Dominican Republic. NA5 MWT rates were shown to decrease over the 101 years. These trends arose only in JJA, SON and MAM (fig 5.14) by -1.26 % , -0.59 % and -1.73 % over the entire period . This decrease is also linked to drops in median and maximum surface wind flow, but only for SON and MAM. JJA has a mix across two significant trends for median surface wind flow.

South America; SA1-SA3

There are three regions in South America shown in fig 5.13, that break down the Andes mountain range into northern (SA1), central (SA2) and southern (SA3) regions. Central and Southern Andes are projected to become considerably more turbulent, with amounts equal to and just greater than NA3. Northern and Central Andes projected MWT amounts are projected to decline within most GCMs for all seasons. The one outlier model and season in SA2 is EC-Earth-3P-HR's SON, which projects an increase within SH spring (fig 5.14.d) of +0.15 %/year.

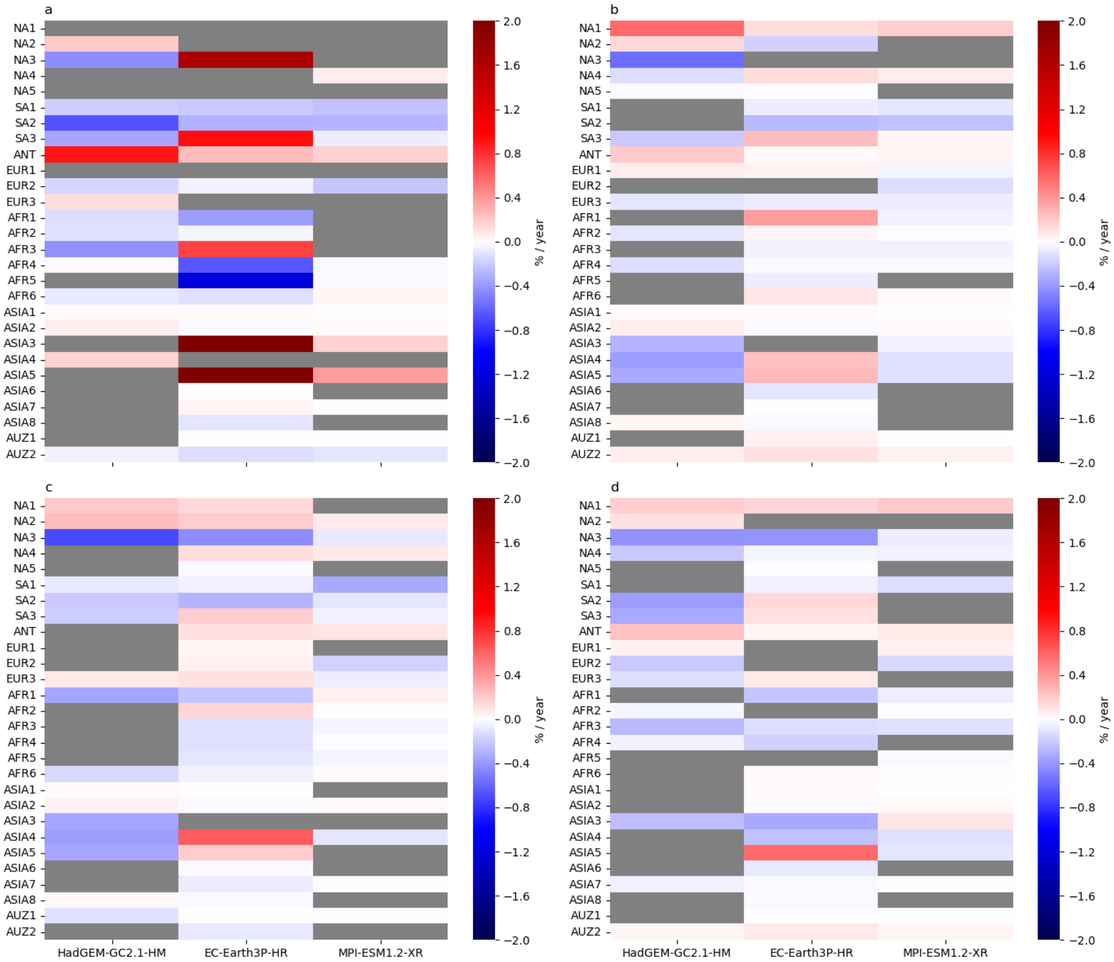

FIGURE 5.14: Seasonal trends for MWT over 28 sub-continental regions, highlighted in Figure 5.13. Over the 101 year period, shaded grey if no significant trend. The figure breaks down results into columns associated with the three GCMs, as evident by labelling on the x-axis. DJF, JJA, MAM and SON displayed in subplot 'a','b','c' and 'd'.

HadGEM3-GC3.1 projected decline is greater, and so on average projects a decline within DJF , JJA, MAM and SON by -11.6 % , -42.9 %, -25.8 % , -20.3 % and -11.6 % , respectively for SA2. There's high confidence that MWT will reduce, across all seasons, within SA1, with strong significant model agreement.

The Northern Andes MWT reduction is greatest in DJF by -22.3 %, then in MAM -16.0%, next SON -9.1% and finally JJA at -8.8% over 101 period. Interestingly, EC-Earth-3P-HR projected weaker surface median wind speed, across all seasons (if applicable). However, stronger surface maximum and median winds are evident in remaining GCMs. SA2's connection to surface wind speed is more apparent. SON's increase in EC-Earth-3P-HR could be linked to the slight stronger median surface winds. The decline in HadGEM3-GC3.1-HM, within this season, is possibly linked to stronger maximum wind speeds, but not median winds. Very similar results obtained for DJF. MAM has only one model with significant surface wind speed, it is in fact decreasing. However, surface winds in JJA are increasing, an opposite trend to how MWT is projected to shift in this area and season. This season has only one wind trend for comparison, but could suggest a seasonal dependence of MWT on low level wind speeds in this region.

There is variation in the GCM projections for the Southern Andes (SA3). Fig 5.13 projects a rise in MWT overall between the two decades, but only one GCM projects this rise (EC-Earth-3P-HR) and due to a wide range of index outcomes, has an insignificant slope. The remaining two GCMs project the opposite scenario with a decline in MWT frequency. These trends continue into the seasonal breakdown in fig 5.14 with HadGEM3-GC.1 and MPI-ESM1.2 project a drop in MWT across all seasons. A tug of war between an increase and decrease for each season arises with SON and MAM decreasing overall by -11/2% and -2.3% but DJF and JJA projections dominated by the single GCM (EC-Earth-3P-HR) with an average of +17.7% and +2.8% across all GCMs.

Over North and South America, a trend has arisen with EC-Earth-3P-HR projections differing to MPI-ESM1.2-XR and HadGEM3-GC3.1-HM, usually with an opposing warming trend. This model variation is also evident within other continents. Within fig 5.15, SA3 has one significant trend, with a drop in median surface wind speeds with MAM HadGEM3-GC3.1-HM. This season and model projects a drop in MWT, suggesting a possible decline linked to low level wind speed.

Europe; EUR1-EUR3

There are three regions over Europe analysed in fig 5.13. It should be noted that EUR3 includes some areas in Africa and Asia. Similar to NA5, EUR3 had more patches of MWT in fig 5.1.g than fig 5.13, that have disappeared when considering the trends in time. Fig 5.13 only shows the confident trends in MWT, rather than the existence of MWT. fig 5.14 encapsulates differences across the seasons within this region. There's strong model agreement on a projected decrease in the amount of MWT by -8.1% in JJA within EUR3. HadGEM3-GC3.1-HM and MPI-ESM1.2-XR projections show a decline in both median and maximum surface wind speed. A decline in low-level wind speed, in both the median and max, are evident for the remaining seasons. In terms of MWT, SON overall decreased in frequency by -2.2% over the 101 period, despite a warming trend in EC-Earth-3P-HR projections. DJF and MAM are projected to increase on average by +13.9% and +4.4% over the century within EUR3.

In contrast, EUR1 and EUR2 have all seasons, in most GCMs, projecting an agreed upon trend in time. Despite, MPI-ESM1.2 projecting a slight drop in MWT in EUR1 summer rates, this season had an overall increase in MWT by +2.7%. Larger increase found in SON and MAM, with a percentage change of +5.1% and +4.4%. JJA and MAM MWT rise are consistent with stronger median surface winds (fig 5.15). DJF had no significant trends in time, so is shaded in grey within fig 5.14.a . EUR2 has all seasons projecting a decrease in MWT. There is quite strong confidence for a decline in DJF, with all three GCMs projecting a drop of -14.7% on average over the period. SON, JJA and MAM follow suit dropping by -18.3% , -13.1% and -6.5%. Interestingly, DJF and MAM have only one model each projecting a trend in fig 5.15. A decline in median surface wind speed is evident. EUR2, which encapsulated the Alps mountain range, is the most turbulent projected region of Europe. This projected decrease in such a turbulent region, will aid future flights through this busy continent.

Africa; AFR1-AFR6

Africa is split into six regions, with AFR1 slightly cutting off the bottom of Spain and Italy but primarily covering Morocco, Algeria, Tunisia and Libya. AFR1 is technically projected most turbulent region in Africa, bur AFR3 is a close second. AFR3 includes regions in the Middle East (Asia). AFR1 and AFR3 display a clear decline in MWT over our projected period of interest within fig 5.13. There are seasonal and model disagreements, evident in fig 5.14. Within AFR1, models agree on a decline with DJF, SON and mostly within MAM projections, with two out of three projecting a decline. Within JJA, EC-Earth-3P-HR projects a moderate increase (relative to the decrease projected by MPI-ESM1.2-XR) resulting in an overall average increase in +16.3 % over the 101 years. DJF, SON and MAM too project a moderate percentage change of -26.1% ,-15.2% and -17.6%. Median surface wind were found to weaken within these seasons (fig 5.15). Results for AFR3 are very similar to those for AFR1, but with an increase found in DJF. EC-Earth-3P-HR projects a steep slope of +0.75%/year. However, HadGEM3-GC3.1 projects a smaller yet still moderate slope of -0.4%/year. On average, AFR3 increase in DJF

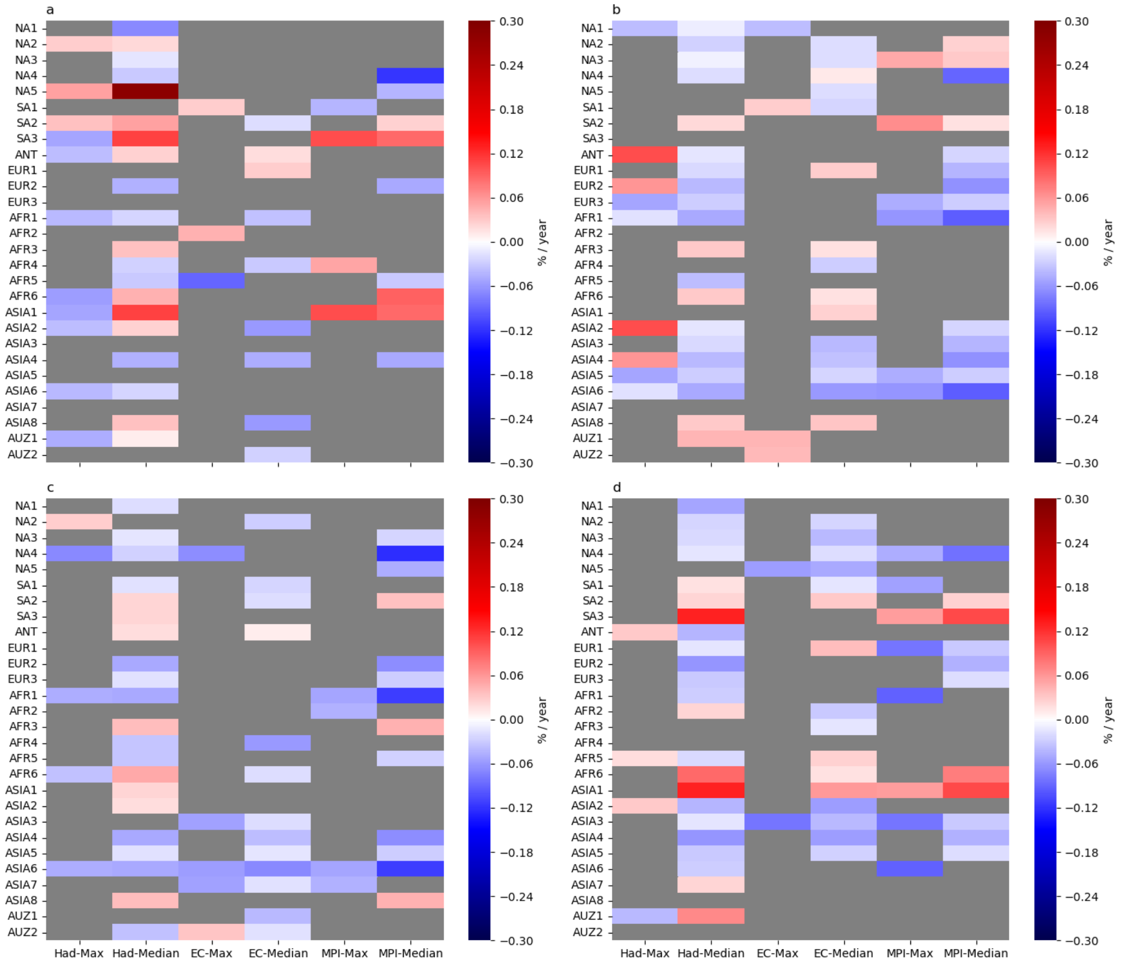

FIGURE 5.15: Trends in surface wind speed for each sub-region shown in fig 5.13. The Maximum and Median winds are discussed individually with notation 'Max' and 'Median' for all GCMs. Each model is donated similar to that in Table 5. 1 & 2 with HadGEM3-GC3.1-HM referenced as 'Had', EC-Earth-3P-HR as 'EC' and MPI-ESM1.2-XR as 'MPI'. DJF, JJA, MAM and SON displayed in subplot 'a','b','c' and 'd'. The grey zones depict insignificant GCM projections.

by +15.9% and decrease in MWT within JJA, SON and MAM by -5.8% , -16.9% and -7.9% . Interestingly, a mix of trends arose for surface wind flow in JJA. The decreases in MAM and SON MWT results are consistent with the decrease seen in low-level median wind flow.

AFR2, AFR4, AFR5 and AFR6 have a much smaller amount of MWT compared to AFR1 and AFR3, this is shown by the negative values the scatter remains in with fig 5.13. In general a decrease in MWT projected across these areas. However, EC-Earth-3P-HR project a notable increase in AFR2 and ARF6 within fig 5.14. This leads to an overall increase of +8.5% in MAM within AFR2 and +6.2% in JJA in AFR6. This summer increase is linked to stronger median surface winds in this model (fig 5.15). However, within AFR2, all surface wind speed changes are projected to get stronger in DJF yet MWT rates are dropping by -7.5%. Despite median surface wind trend often associated with the corresponding trend in MWT, there are a few exceptions with differing outcomes. JJA and SON project a slight decrease in MWT of -0. 5% and -1. 9%. AFR6 has a slight increase in SON by +1.1%, but declines in DJF and MAM by -9.2% and -4.9% over the 101 year period. The most considerable decrease in Africa are found within AFR5, with DJF MWT rates decreasing by -61.6% over the 101 year period. EC-Earth-3P-HR is the considerable driver in these large trends (fig 5.14.a). A decrease in MWT also evident in JJA, SON and MAM, with strong model agreement, but at lower rates of -6.8%,

-2.20% and -6.6% for AFR5. The change in maximum wind speed decrease in all seasons within ARF5, correlating to the MWT trend. AFR4 has its most notable decrease in MWT within SON by -12.0 %, followed by MAM by -6.4% and then similar declines in MWT within DJF and JJA on average across the GCMs at -2.4% and -2.3%.

Asia; ASIA1-ASIA8

Over Asia, eight zones were chosen for further analysis. This was done due to differing trends on initial analysis and MWT developing in many regions over this continent. The largest amount of projected MWT is found in Asia in zone ASIA4. This area includes the Himalayan mountain range and Tibetan plateau within it. As fig 5.13 clearly shows, this area is decreasing in percentage of MWT by the end of the century compared to the beginning. However, fig 5.14, shows this decline is only evident in SON, with two significant slopes in models EC-Earth-3P and MPI-ESM1.2-XR projecting a drop of -18.4% on average over the period. This is linked to weaker median surface winds this season, as evident in fig 5.15. Within ASIS4, both JJA and MAM have HadGEM3-GC3.1-HM and MPI-ESM1.2-XR models projecting a decline in MWT, with EC-Earth-3P-HR projecting a considerable increase. In the tug of war, EC-Earth-3P monopolizes MAM projections due to its steep slope of +0.64 %/year. This leaves ASIA4 increase on average of +5.0% in MAM.

The other two GCMs dominate the JJA averages, resulting in an overall decrease of -8.5% over 101 years. HadGEM3-GC3.1-HM, despite projecting a decrease in JJA, projected stronger maximum surface winds but weaker median surface wind flow. Interestingly, EC-Earth-3P-HR MAM median surface winds projected a rise over the 101-year period, a different trend to that examined above around MWT percentage shifts. Only HadGEM3-GC3.1 projects significant slopes in DJF, with a projected increase of 18.3%. One can note an almost equal shift in MWT across seasons from SON towards DJF. This level of increase within the most turbulent projected region of the globe is a noteworthy finding, considering that long-haul flights often travel through this area. The median surface wind flow projecting a decline over DJF within fig 5.15, suggests this increase is possibly linked to upper-level dynamical variation. The strengthening in upper-level jet streams in time has lead to an increase in clear air turbulence production. As projected MWT has large seasonal shifts throughout the globe, perhaps alterations in the upper-level jet with climate change is also having a direct or in-direct impact on MWT production. Further research should be done on this possible connection.

ASIA5 and ASIA3 are the 2nd and 3rd most turbulent regions in the Asia. ASIA3 interestingly, within fig 5.13, has two significant slopes both projecting different trends in time. These two opposing trends arise from averaging over a large region and seasonal variation. EC-Earth-3P-HR is not within this scatter plot but has significant trends when broken down seasonally, with a DJF trend of +2.0%/year. DJF, averaged over GCMs, has an increase of +112.3% in MOG MWT over this region. Fascinatingly, the remaining seasonal project an overall decrease in MOG MWT, by -36.1 % (MAM), -17.4% (JJA) and -16.6% (SON). A trend also evident this regions median and maximum surface winds (fig 5.15). No significant surface wind trends found for DJF in AISA3 or ASIS5. However, there are significant MOG MWT within DJF in ASIA5, with an increase of +123.4%. SON also projected an overall average change of +23.0%. A decrease was found in JJA and MAM by -5.9% and -7.9%. In relation to surface wind speeds trends, this region had JJA, MAM and SON all with projected declines in median and maximum.

The remaining regions in Asia propagate below zero in fig 5.13 scatter plots, and therefore have considerable less MWT amounts than the three aforementioned ASIA zones. Within fig 5.14, ASIA2 EC-Earth-3P-HR projects a decline in MWT over all seasons in this region, possibly associated with the slight drop over southern Japan (fig 5.13). The remaining two GCMs, if applicable, projected an increase in MWT in all seasons. This is further evident in fig 5.13 ASIA2 side plot, with MPI-ESM1.2 and HadGEM3-GC3.1 projecting an increase, but EC-Earth-3P-HR projecting a decline. Overall the maximum increase in this region arose in JJA at +2.4% in JJA and minimum in SON of +0.8% over the 101 years. ASIA1, has a slight increase across all GCMs (strong model agreement) and seasons, with the maximum percentage change over the century at +1.7% in SON and minimum of +1.4% in DJF.

The final three regions of Asia encompass Indian and Sri Lanka (ASIA6), south eastern Asia (ASIA7/8) and a few countries in the Australian continent (Papa New Guinea; ASIA8). ASIA6-8 have a general decline over the period, with a decrease in SON and MAM. Although a slight MAM increase in HadGEM3-GC3.1 in ASIA8. IN DJF, ASIA6 projects extremely small increase over the 101 years (-0.08%) , ASIA7 projects a light increase (1.86%), with ASIA8 finding a decline in MWT of -10.1% . Within the JJA projections, ASIA6 has a relatively moderate decline of -9.9% , ASIA7 projects slight increase of +0.5% and ASIA8 has two disagreeing GCMs projecting a slight increase (HadGEM3-GC3.1-HM) and decrease (EC-Earth-3P) overall resulting in a small increase of +0.76% over the century.

Australia and Antarctic; AUZ1, AUZ2 and ANT

As discussed there are technically three regions within the Australian continents. AUZ1 and AUZ2 are located south of ASI8 over Australia and New Zealand. AUZ1, which includes areas in the Australian country like New South Wales, Victoria and Tasmania, had more features within fig 5.1, but only a few scattered patches within fig 5.13's global map. The lines within AUZ1's scatter plot both project an overall slight decrease over the 101 years. Within fig 5.14, the white patches occur often in subplots a,b,c and d within the AUZ1 section. They suggest an extremely small, almost no change result. However, in MAM and JJA, there are slight shifts within HadGEM3-GC3.1 and EC-Earth-3P results with a decrease of -3.8% in MAM and increase of +1.6% in JJA over the 101 year projected period. These trends correlate to shifts in low-level surface wind speed shifts within the period. AUZ2, which covers New Zealand, looks to be increasing in time within fig 5.13 . SH winter and spring (JJA, SON) have full model agreed projected positively sloped trends in time, increasing by +8.4% and +5.9% over the period. However, DJF (SH summer) and MAM (SH autumn) are decreasing in time, with GCMs agreement, by -9.4% and -8.1% . Interestingly, the amount of MWT in this box is greater than many regions in Asia and Africa.

There are no new regions in the Antarctic, with similar projections evident across continent. However, the scatter box, titled 'ANT' do show the average over the previous line plots in fig 5.12 . The average amount of MWT over the Antarctic, across the indices, is just greater than the Alps (EUR2) and around a similar range as found in AFR1 over the Atlas Mountains. The increases here correlate to the findings in Table 5. 2, with an steep increase found in DJF, particularly in HadGEM3-GC3.1 model. This shift may partly be associated with increased low-level and upper-level wind speed over this polar region. The British Antarctic Survey found surface winds strengthen by 15% since 1980. This is a trend evident in fig 5.3 to 5.5 and within fig 5.15, with all GCMs and both median and maximum surface wind trends projecting stronger flow for the Antarctic continent.

5.4 Conclusion and future work

Through the use of three HighRes-MIP CMIP6 GCMs, this study investigates the modeled projections of global MWT turbulence over a 101-year period. Through an initial comparison between the 1950-60 and 2040-50 decade, one found coarser models were not able to detect as much detail as their finer counterparts. This was linked to improved gradient and terrain height information. This study continued only with three higher resolution models; HadGEM3-GC3.1-HM (25km), EC-Earth-3P-HR(36km) and MPI-ESM1.2-XR (34km). Each MWT index was broken down and analysed initially through two period decadal comparison (fig 5.3 to 5.5) and then continental yearly analysis (fig 5.6 to 5.12). Regional dependencies arose around model and index agreement, with seasonal components an important contributor to results. Finally a sub-regional approach was discussed, where seasonal MWT and surface wind speed trends were analysed.

On average, the North American continent had an increase in MWT since the starting decade. However, a lot of the trends in time were not deemed significant. On further sub-continental analysis, the zone encapsulating the Rocky Mountain range, was shown to be decreasing in the amount of MWT in all seasons but NH winter. Within DJF, increase of +60.6% in MOG MWT arose, with similar yet opposite rates of -58.3%, -41.2 % and -30.9% for JJA, MAM and SON. Greenland, a region used often for transatlantic travel, is increasing in the amount of MWT, with its greatest shift in JJA by +30.5%. Over South America, a decrease in MWT was evident from initial analysis. There is strong model agreement that the North and Central regions of the Andes will have a large decreases in MOG MWT within SH summer (DJF), with drops of -22.3% and -49.2%, retrospectively. Southern Andes have a shift across seasons, with DJF and JJA projecting increases in MWT, at most in DJF at +17.7%. Although SON and MAM, project a decline, at most at -11.2% in SON.

Over Europe and Africa, a decline in MWT is evident over the Alps and Atlas Mountain ranges. NH autumn over the Alps has the largest decline of -18.3%, followed quickly after by DJF at -14.7%. DJF had a decline of -26.1% over parts of the Atlas mountains, with a decline in MWT evident across the entire African continent. However, large increases arose over Asia, with two regions projected an increase above +100% (ASIA3/5) in DJF. Interestingly, over the Tibetan plateau and Himalayas, MWT rates increased within DJF and MAM by +18.3% and +5.0%, but a similar yet opposite increase for SON and JJA of -18.4% and -8.5%. The last region of significant change occurred over the Antarctica peninsular, with DJF and

JJA increasing by +32% and +8.7%. Further regions were explored, with many areas having a close trend related to median surface wind speed and it change over the century. However, several regions and seasons were less dependent on the low-level wind speeds. In terms of significance to forecasting operations in the aviation sector, results over Asia, Europe, North and South America are key, considering the high density of flights that travel over these regions.

Overall, a mixture of MWT changes arose across the globe. The aviation sector should be aware of the future projections in MWT, particularly for those were large increase over the 101 year period were evident, such as Asia, Greenland and the Antarctic. Future work should focus on differing warming scenarios, other to SSP5-8.5, to get a full picture of possible future MWT outcomes.

5.4.1 Limitations

This paper acknowledges that modelled atmospheric and ocean data is used, all projections are based on a future scenario of the globe.SSP5-8.5 is the extreme climate warming scenario with no action, with little mitigation or adaptation (Deng 2022). One limitation within previous work (Sharman and Pearsons (2017), Kim et al. (2023), that continues within this paper is that MWT often occurs downstream from mountain ranges (Wilms,Henrike,20220). Our region should encapsulate source of the downstream MWT due to our inclusion of slope gradient, but may miss MWT which travels far distances due to certain meteorological conditions (Lane et. al, 2009).

Chapter 6

Summary and impact of results

Chapter 1 explored previous studies around clear air and mountain wave turbulence, and concluded that there were three key areas of research lacking in current turbulence literature. To address these gaps in research, three aims of this thesis were developed and are listed below.

1. Quantify change in CAT within a range of CMIP6 GCMs, with the initial focus over the North Atlantic. Within this aim, evaluating the systematic relations between climate model resolution and projected turbulence will also be addressed.
2. Understand if patches of CAT may vary in a future scenario due to a change in frequency or size, across a range of GCMs, over the NH and SH latitudes where CAT is most prominent.

3. Globally quantify shifts in MWT within a range of CMIP6 GCMs and address the shifts in MWT prior to 2056. Understand if TS is having an impact on MWT within these GCMs.

This chapter initially discusses the main findings concluded in each investigation (aim) of the thesis. Next, we discuss the overlap between results across the chapters. The last section of this chapter explores the limitations of our research and future work for the turbulence research community.

6.1 Trend in clear-air turbulence over the North Atlantic

Here, we aim to quantify the changes to CAT, using a multi-model approach, with the most UpToDate CMIP GCMs, and explore the dependence of model resolution on CAT results. Using three GCMs, with seven horizontal resolutions, this aim is addressed. Our region of interest is an area within North Atlantic basin (50–75°N, 300–350°E), which was used previously in Williams (2017) and Williams and Joshi (2013), due to the high density of international flights travelling through the area. The atmospheric pressure level 200 hPa is our height used within this investigation, and throughout our thesis, due to it being a typical cruising altitude and due to the availability of data from our GCMs.

Previous work found an increase in CAT, in all seasons over the North Atlantic. Using a high-end warming scenario, we conclude that this trend continues within CMIP6 GCMs analysis, after taking an average across the models and 21 different indices used to represent CAT. As shown in Chapter 2, all GCMs are developed with the same initial conditions and span a 101-year period. Despite comparison with time an effective way of showing the change in CAT with global tropospheric warming, one can also use a metric to compare across the GCMs. Using near-surface warming, we conclude that moderate CAT will increase by 8.94 ± 1.54%/°C, 8.81 ± 1.90%/°C, 13.69 ± 1.28%/°C and 13.82 ± 1.27%/°C for northern hemisphere winter, spring, summer and autumn. Interestingly, SON (September, October, November) produced the greatest overall increase, with high model agreement. The Max-Planck institute GCMs produced several insignificant trends in time, but agreed with high confidence that the North Atlantic autumn CAT production is increasing over the 101 period and with near surface warming.

In terms of model dependency, within our initial breakdown of indices, three indices used to diagnose CAT (relative vorticity advection; negative absolute vorticity advection; Brown index) projected their greatest increase in CAT in models with horizontal grid spacing greater than 60km. However, the remaining eighteen indices do not show this difference. Within our SON projections, we do conclude that coarser sub-models generally produce greater increases in time and with near-surface warming. However, for the remaining seasons, there seems to be little variations across GCMs, with the model resolution projecting similar ranges in their projections.

6.2 Evaluation of clear air turbulence patches in high-resolution global climate models

Our key aim of this investigation was to break down the change in CAT into the physical response, rather than working in a percentage change. This approach was applied to understand how the number of patches, the average size of a patch and the total area of CAT could change in a future warming scenario, across several GCMs. This aim was met through analysis of moderate CAT over two bands in the NH and SH (30-75 N/S) at a 200 hPa atmospheric pressure level.

In both hemispheres, winter, autumn and spring's multi-model median results were projecting an increase in the total area of CAT per year. The largest increase is projected in winter, with NH and SH projecting an average change of +360.16 +/- 48.10 km^2 and +474.13 +/- 43.72 km^2 per year. This increase occurred due to an increase in both the average patch size and the number of patches, with an increase of +1.32 +/- 0.42 km^2 and 0.05+/- 0.007 patches per year and 0.89 +/- 0.31 km^2 and 0.07 +/- 0.007 patches per year, respectively.

An increase in moderate CAT area was found for NH spring and SH autumn due to an increase in the just the number of CAT patches. For NH autumn and SH spring an increase in both size and frequency was evident. There is large model disagreement on the result for summer-time CAT, with an average decrease in the area, with the SH basin reducing by -105.35 +/- 35.33 km^2 per year. Within the NH basin, summer-time CAT projections had too much variation between GCMs to determine a significant trend in time.

Throughout this investigation, an increase in the number of patches remained a consistent trend in most seasons. With, the average patch of CAT size having a greater seasonal and model variation.

6.3 Global change in mountain wave turbulence within high resolution climate models

Due to the limited number of studies quantifying MWT in a changing climate, the final aim of this thesis was to understand how this type of turbulence was projected to change across several CMIP6 GCMs. Previous literature focused on MWT between 1970-2014 and 2056-2101. (Kim et al., 2023), therefore our analysis focused between 1950-2050 has implications for MWT over the next 26 years. This thesis met this aim through a global analysis of moderate or greater (MOG) MWT projections, using six indices and the finest three GCMs within HighResMIP; HadGEM3-GC3.1-HH/HM, EC-Earth-3P-HR and MPI-ESM1.2-XR. Through an initial comparison between the 1950-60 and 2040-50 decade it was found that coarser models were not able to represent as much detail as their finer counterparts. This is linked to finer and improved gradient and terrain height information within the higher resolution models.

An average increase in CAT was found for the North American continent (including Greenland). However, several trends were not significant. On further analysis, MWT in the Rockies Mountain Range, was shown to be decreasing in all seasons but NH winter (DJF). Within DJF, an increase of +60.6% in MOG MWT was found, with a decrease in JJA, MAM and SON by -58.3 %, -41.2 % and -30.9 %. Greenland, a country travelled over often by transatlantic travel, is increasing, with its greatest change in JJA by +30.5%. Over South America, a decrease in MWT was evident from initial analysis. There is strong model agreement that MOG MWT in the north and central regions of the Andes will have a large decrease within SH summer (DJF) by -22.3% and -49.2%, retrospectively. MWT percentage trends in the southern Andes differ across seasons, with DJF and JJA projecting increases in MWT (most in DJF at +17.7 %) and decreasing in MAM and SON (at most in SON -11.2%).

Over Europe and Africa, a decrease in MWT was found over the Alp and the

Atlas Mountain ranges. The largest decline of -18.3% was found for the Alps in SON, followed closely by DJF at -14.7%. A decline in MWT was found across the African continent was a decrease of -26.1% in SON.

Interestingly, in Asia over the Tibetan plateau and Himalayas, MWT increased within DJF and MAM by +18.3% and +5.0%, but a decrease of similar magnitude was found for SON and JJA at -18.4% and -8.5%. One region which a significant change was the Antarctica peninsula, with DJF and JJA increases of +32% and +8.7%. Further regions were explored, with many areas having a MWT trend associated to median surface wind speed. The global response was closely linked to how the median surface winds varied.

6.4 Comparison across Chapters

Chapter 3 and 4 explore the change in CAT area through different methods, with the first associating the change in terms of a percentage from a decade reference and the second evaluating the total CAT area change in km^2. Chapter 4 shows that the increase in spring (+8.81%) over the North Atlantic is likely related to an increase in the number of patches per year. Whereas winter and autumn, for which there is less spread in model projections in chapter 3, both show an increase in CAT due to a rise in the number of patches and the average size of the patches.

The multi-model median summer-time projections for CAT over the NH basin in Chapter 4 were not significant. Within chapter 3, the MPI-ESM1.2-XR and MPI-ESM1.2-HR projections for moderate CAT are also not significant (fig 3.4) in time in summer (JJA). EC-Earth-3P and EC-Earth-3P-HR projections showed steep increases in summer-time CAT over the North Atlantic in chapter 3, with values ranging between 15.70 to 22.53%/C. A consistent increase in summer-time moderate CAT in the NH band is seen for these models in chapter 4. These differences highlight the important of applying a multi-model approach to CAT projections. Within Chapter 3, the frequency of summer-time North Atlantic CAT projections suggested summer could be as turbulent as winter and autumn in the 1950s. Chapter 4 results suggest this finding is only specific to the North Atlantic and cannot be assumed for the remaining areas within chapter 4's NH or SH band, with a decrease in CAT total area over summer in the SH band.

In summary, this multi-model analysis found that CAT is projected to increase in future over the North Atlantic, for all seasons. It determined that globally in the mid to high latitudes the number and size of an average patch of moderate CAT were increasing as the frequency rose in NH and SH winter. It finally determined that MWT may increase in some regions of the globe, as well as decrease in others depending on the change in low-level wind speed. These results will have consequences for to the aviation industry, with more flights possibly disrupted, leading to increasing damages and costs, as well as impact on passengers and crew.

6.5 Future work

Due to limitations in our modeled data and time constraints of this thesis, there are unfortunately areas not addressed within our analyses. For example, all results within this thesis focus on one atmospheric pressure level (200 hPa). Future work could explore different altitudes, using CMIP6 or CMIP7 (soon to be released) GCMs. Understanding CAT could change in a future warming scenario was addressed within this thesis. However, all results use the same warming metric of SSP5-8.5. Future investigations should explore how CAT could change in different climate change scenarios. This should also be done for MWT, with a limited number of studies on the change in MWT with global warming. Further work into the connection between shifts in the upper-level jet stream and MWT is also an area that should be tackled further.

Chapter four of this thesis explored how the patches of turbulent air were varying within the projected modeled data. Despite interesting analysis found on the number of patches increasing, on average, rather than the overall width, further work could be done to determine where the number of patches increased most.

This section explored averages over the northern and southern hemisphere, regional and sub-continental future experimentation would be key for operational planning.

Chapter 7

References

Atrill J, Sushama L, Teufel B (2021) Clear-air turbulence in a changing climate and its impact on polar aviation. Saf Extreme Environ 3(2):103–124. https://doi.org/10.1007/s42797-021-00036-y

Bock L, Lauer A, Schlund M, Barreiro M, Bellouin N, Jones C, Meehl G, Predoi V, Roberts M, Eyring V (2020) Quantifying progress across different CMIP phases with the ESMValTool. J Geophys Res Atmos. https://doi.org/10.1029/2019JD032321

Colson D, Panofsky H (1965) An index of clear air turbulence. Q J R Meteorol Soc 91(390):507–513. https://doi.org/10.1002/qj.49709139010

Chun H., Kim Y., (2008) Secondary waves generated by breaking of convective gravity waves in the mesosphere and their influence in the wave momentum flux. Journal of Geophysical Research: Atmospheres, Volume 113, Issue D23. https://doi.org/10.1029/2008JD009792

Deng, K., Liu, W., Azorin-Molina, C., Yang, S., Li, H., Zhang, G., et al. (2022). Terrestrial stilling projected to continue in the Northern Hemisphere mid-latitudes. *Earth's Future*, 10, e2021EF002448. https://doi.org/10.1029/2021EF002448

EASE; European Union Aviation Safety Agency, European Aviation Environmental Report 2022. https://www.easa.europa.eu/eco/sites/default/files/2023-02/230217$_{E}ASA\%20EAER\%202022.pdf$ Accessed March, 2024.

EC-Earth https://ec-earth.org. Accessed July, 2024.

ECMWF, European Centre for Medium-Range Weather Forecasts Website; Reanalysis v5 (ERA5). https://www.ecmwf.int/en/forecasts/dataset/ecmwf-reanalysis-v5 Accessed July, 2024.

Ellrod G, Knapp D (1992) An objective clear-air turbulence forecasting technique: verification and operational use. Weather Forecast 7(1):150–165. https://doi.org/10.1175/1520-0434(1992)007%3c0150:AOCATF%3e2.0.CO;2

Ellrod G., Knox J., Lester P., Ehernberger L. (2015): Aviation Meteorology: Clear

Air Turbulence. Encyclopedia of Atmospheric Sciences: Second Edition. p177-186. https://doi.org/10.1016/B978-0-12-382225-3.00104-3

Eick, D. (2014) Turbulence related accidents and incidents. Presentation at NCAR turbulence impact mitigation workshop 2, 3–4 September 2014. https://ral.ucar.edu/sites/default/files/docs/eick-turbulencerelatedaccidents.pdf

Eyring V., Bony S., Meehl G., Senior C., Stevens B., Stouffer R., Taylor K., (2016), Overview of the Coupled Model Intercomparison Project Phase 6 (CMIP6) experimental design and organization. Geoscientific Model Development. 9(5), 1937-1958. http://doi.org/10.5194/gmd-9-1937-2016

Federal Aviation Administration (FAA), Air Traffic By The Numbers. FAA_link, Accessed April, 2024.

Federal Aviation Administration (FAA), Aircraft Wake Turbulence, Wake Vortex Encounter - Mitigation. FAA_link, Accessed April, 2024.

Federal Aviation Administration (FAA), Aeronautical Information Manual (AIM), Section 4. Wake Turbulence. FAA_link, Accessed April, 2024.

Gill, P. G., Stirling, A. J. (2013). Including convection in global turbulence forecasts. *Meteorol. Appl.*, 20(1), 107–114. https://doi.org/10.1002/met.1315

Gill, P. (2014) Objective verification of World Area Forecast Centre clear air turbulence forecasts. Meteorological Applications, 21(1), 3–11. https://doi.org/10.1002/met.1288

Gill P., Buchanan P., (2014) An ensemble based turbulence forecasting system. Meteorological Applications. 21(1) 12-18. https://doi.org/10.1002/met.1373

Gutjahr O., Putrasahan D., Lohmann K., Jungclaus J., Von Storch J., Brüggemann N., Haak H., Stössel A., (2019): Max Planck Institute Earth System Model (MPI-ESM1.2) for the High-Resolution Model Intercomparison Project (HighResMIP) Geoscientific Model Development, 3241-3281, 12(7). https://doi.org/10.5194/gmd-12-3241-2019

Golding W., (2002). Turbulence and Its Impact on Commercial Aviation., Journal of Aviation/Aerospace Education & Research, 11(2). https://doi.org/10.15394/jaaer.2002.1301

Gerz T., Holzapfel F., Darracq D., (2002). Commercial Aircraft Wake Vortices. Progress in Aerospace Sciences 38(2002):181-208. https://doi.org/10.1016/S0376-0421(02)00004-0

Haarsma, R., Roberts, M., Vidale, P., Senior, C., Bellucci, A., Bao, Q., Chang, P., Corti, S., Fučkar, N., Guemas, V., von Hardenberg, J., Hazeleger, W., Kodama, C., Koenigk, T., Leung, L. R., Lu, J., Luo, J.-J., Mao, J., Mizielinski, M.,. . . von Storch, J.-S. (2016). High Resolution Model Intercomparison Project (HighResMIP v1.0) for CMIP6. Geosci. Model Dev., 9(11), 4185–4208. https://doi.org/10.5194/gmd-9-4185-2016

Haarsma, R. (2017). HighResMIP- High Resolution Model Intercomparison Project, Version 1.0. https://doi.org/10.5194/gmd-9-4185-2016

IATA, 2024, International Air Transport Association, Forecast Data Statistics. https://www.iata.org/en/iata-repository/publications/economic-reports/airline-industry-economic-performance-june-2023-data-update/, Accessed April 2024.

Hawkins, E., and R. Sutton, (2009): The Potential to Narrow Uncertainty in Regional Climate Predictions. Bull. Amer. Meteor. Soc., 90, 1095–1108, https://doi.org/10.1175/2009BAMS2607.1.

Holton J. R., Hakim G. J., (2012).An Introduction to Dynamic Meteorology ,Academic Press, Elsevier Inc, Fifth edition. https://doi.org/10.1016/C2009-0-63394-8

Hu B, Tang J, Ding J, Liu G (2021) Regional downscaled future change of clear-air turbulence over East Asia under RCP8.5 scenario within the CORDEX-EA-II project. Int J Climatol. https://doi.org/10.1002/joc.7114

Intergovermental Panel on Climate Change (IPCC) Sixth Assessment Report (2023). The Physical Science Basis, Weather and Climate Extreme Events in a Changing Climate. Chapter 11. 1514-1765 https://www.ipcc.ch/report/ar6/wg1/downloads/report/IPCC$_{A}R6_{W}GI_{C}hapter11.pdf$

Jaeger E, Sprenger M (2007) A Northern Hemispheric climatology of indices for clear air turbulence in the tropopause region derived from ERA40 reanalysis data. J Geophys Res 112(D20):1–13. https://doi.org/10.1029/2006JD008189

Kaplan M, Huffman A, Lux K, Cetola J, Charney J, Riordan A, Lin Y, Waight K (2004) Characterizing the severe turbulence environments associated with commercial aviation accidents. Part 2: Hydrostatic mesoscale numerical simulations of supergradient wind flow and streamwise ageostrophic frontogenesis. Meteorol Atmos Phys 88(3–4):153–173. https://doi.org/10.1007/s00703-004-0079-6

Kauffmann P., (2002). The business case for turbulence sensing systems in the US air transport sector. Journal of Air Transport . 99-107, 8(2), 10pt

Kim, J., Sharman, R., Strahan, M., Scheck, J., Bartholomew, C., Cheung, J., Gait, N. (2018). Improvements in Nonconvective Aviation Turbulence Prediction for the World Area Forecast System. *Bulletin of the American Meteorological Society*, 99(11), 2295–2311. `https://doi.org/10.1175/bams-d-17-0117.1`

Kim, S., Kim, J., Chun, H., Sharman, R. D. (2023). Global response of upper-level aviation turbulence from various sources to climate change. *npj Climate and Atmospheric Science*, 6(1), 92. `https://doi.org/10.1038/s41612-023-00421-3`

Knox J (1997) Possible mechanisms of clear-air turbulence in strongly anticyclonic flows. Mon Weather Rev 125(6):1251–1259. https://doi.org/10.1175/1520-0493(1997)125%3C1251:PMOCAT%3E2.0.CO;2

Koch SE et al (2005) Turbulence and gravity waves within an upper-level front. J Atmos Sci 62(11):3885–3908. https://doi.org/10.1175/JAS3574.1

Lamb S. H.,(1945) Hydrodynamics, 6th edn, Dover publications, New York, NY

Lane T., Sharman R.D, Clark T.L, Hsu H., An investigation of turbulence generated mechanisms above deep convection. J. Atmos. Sci. 60(10),1297-1321; https://doi.org/10.1175/1520-0469(2003)60<1297:AIOTGM>2.0.CO;2

Lane, T., Doyle, J., Sharman, R. D., Shapiro, M. A., Watson, C. D. (2009). Statistics and dynamics of aircraft encounters of turbulence over Greenland. *Monthly Weather Review*, 137(8), 2687–2702. `https://doi.org/10.1175/2009MWR2878.1`

Lane, T.P., Sharman, R., Frehlich, R.G., Brown, J.M. (2006) Numerical simulations of the wake of Kauai with implications for the Helios flights. J. Appl. Meteorol. Climatol. 45(9), 1313–1331

Lee L (2013) A climatological study of Clear Air Turbulence over the North Atlantic. Dissertation. Uppsala University, Department of Geosciences

Lee S, Williams P, Frame T (2019) Increased shear in the North Atlantic upper-level jet stream over the past four decades. Nature 572(7771):639–642. https://doi.org/10.1038/s41586-019-1465-z

Lee J., Kim J., Sharman R., Kim J., Son S., (2023):Climatology of Clear-Air Turbulence in Upper Troposphere and Lower Stratosphere in the Northern Hemisphere Using ERA5 Reanalysis Data. Journal of Geophysical Research: Atmospheres. 128(1), https://doi.org/10.1029/2022JD037679

Lester, P. F. (1993). Turbulence: A New Perspective for Pilots. Jappesen Sanderson, Englewood, CO.

Lv Y et al (2021) Increased turbulence in the Eurasian upper-level jet stream in winter: past and future. Earth Space Sci. https://doi.org/10.1029/2020EA001556

MacCready PB (1964) Standardization of gustiness values from aircraft. J Appl Meteorol 3(4):439–449

MacGorman D. R., Rust W.D.,(1998); The Electrical Nature of Storms. Oxford University Press, 422

Madonna E.,Li C.,Grams C.,Woollings T.,(2017): The link between eddy-driven jet variability and weather regimes in the North Atlantic-European sector. Quarterly Journal of the Royal Meteorological Society, 2960-2972, 143(708)https://doi.org/10.1002/qj.3155

Mauritsen T et al (2019) Developments in the MPI-M earth system model version 1.2 (MPI-ESM1.2) and its response to increasing CO 2. J Adv Model Earth Syst 11(4):998–1038. https://doi.org/10.1029/2018MS001400

Met Office; Worlds Area Forecast Centre. `https://www.metoffice.gov.uk/services/transport/aviation/regulated/international-aviation/wafc/index` Accessed June, 2024.

National Air Traffic Services, Annual Safety Report (2023)https://www.nats.aero/wp-content/uploads/2024/05/SafetyReport2023-May.pdf Acessed June, 2024.

Nappo C. J., Gravity Wave Instability and Turbulence (2012), International Geophysics, 102, 117-157https://doi.org/10.1016/B978-0-12-385223-6.00005-7

Oakes M., Bor R.,(2010); The psychology of fear of flying (part II): A critical evaluation of current perspectives on approaches to treatment.Travel Medicine and Infectious Disease. 8(6), 327-338 https://doi.org/10.1016/10.1016/j.tmaid.2010.10.001

Overeem A (2002) Verification of clear-air turbulence forecasts. Technisch rapport, KNMI (Royal Netherlands Meteorological Institute), pp 1–63

Pao Y.,, Goldberg A., (1969).Clear Air Turbulence and Its Detection Plenum Press, New York, NY

Prosser, M. C., Williams, P. D., Marlton, G. J., Harrison, R. G. (2023). Evidence for large increases in clear-air turbulence over the past four decades. *Geophysical Research Letters*, 50, e2023GL103814. `https://doi.org/10.1029/2023GL103814`

Puempel H, Williams PD (2016) The impacts of climate change on aviation: scientific challenges and adaptation pathways. ICAO Environmental Report: On Board a Sustainable Future, pp 205–207

Qin Z., He Y.,Zhao X.,Feng Y.,Yi X., (2022). A case analysis of turbulence characteristics and ozone perturbations over eastern China.Frontiers in Environmental Science. 10, https://doi.org/10.3389/fenvs.2022.970935

Roberts M., Baker A., Blockley E., Calvert D., Coward A., Hewitt H., Jackson L., Kuhlbrodt T., Mathiot P., Roberts C., Schiemann R., Seddon J., Vannière B., Luigi Vidale P., (2019), Description of the resolution hierarchy of the global coupled HadGEM3-GC3.1 model as used in

CMIP6 HighResMIP experiments.Geoscientific Model Development, 4999-5028, 12(12),https://doi.org/10.5194/gmd-12-4999-2019

Ramaswamy V., Chanin M., Angell J., Barnett J., Gaffen D., Gelman M.,Keckhut P., Koshelkov Y., Labitzke K., Lin J.,O'Neill A., Nash J., Randel W., Rood R., Shine K., Shiotani M., Swinbank R.,(2001), Stratospheric Temperature Trends: Observations and Model Simulations,Reviews of Geophysics,71-122, 39(1),https://doi.org/10.1029/1999RG000065

Riahi K., van Vuuren D. ,Kriegler E., Edmonds J., O'Neill B., Fujimori S., Bauer N., Calvin K., Dellink R., Fricko O., Lutz W., Popp A. ,Cuaresma J., KC S., Leimbach M., Jiang L., Kram T., Rao S.,Emmerling J., Ebi K., Hasegawa T., Havlik P., Humpenöder F., Da Silva L.,Smith S., Stehfest E., Bosetti V. ,Eom J., Gernaat D.,Masui T., Rogelj J., Strefler J., Drouet L., Krey V., Luderer G., Harmsen M., Takahashi K., Baumstark L., Doelman J., Kainuma M., Klimont Z., Marangoni G., Lotze-Campen H., Obersteiner M., Tabeau A., Tavoni M.(2017);The Shared Socioeconomic Pathways and their energy, land use, and greenhouse gas emissions implications: An overview, Global Environmental Change,153-168, 42 https://doi.org/10.1016/j.gloenvcha.2016.05.009

Schiemann R, Athanasiadis P, Barriopedro D, Doblas-Reyes F, Lohmann K, Roberts MJ, Sein DV, Roberts CD, Terray L, Vidale PL (2020) Northern Hemisphere blocking simulation in current climate models: evaluating progress from the climate model intercomparison project phase 5 to 6 and sensitivity to resolution. Weather Clim Dynam 1(1):277–292. https://doi.org/10.5194/wcd-1-277-2020

Search Technology (2000) A pilot-centered turbulence assessment and monitoring system, TAMS, Phase II Final Report. Norcross, GA

Sharman, R., Tebaldi, C., Wiener, G., Wolff, J. (2006). An integrated approach to mid- and upper-level turbulence forecasting. *Weather and Forecasting*, 21, 268–287. https://doi.org/10.1175/WAF924.1

Sharman, R. D., et al. (2014). Description and derived climatologies of automated in situ eddy-dissipation-rate reports of atmospheric turbulence. *J Appl Meteorol Climatol*, 53(6), 1416–1432. https://doi.org/10.1175/JAMC-D-13-0329.1

Sharman, R., Lane, T. (2016). Aviation Turbulence: Processes, Detection, Prediction. Springer International Publishing. https://doi.org/10.1007/978-3-319-23630-8

Sharman, R., Pearsons, J. M. (2017). Prediction of energy dissipation rates for aviation turbulence. Part I: Forecasting nonconvective turbulence. *Journal of Applied Meteorology and Climatology*, 56(2), 317–337. https://doi.org/10.1175/JAMC-D-16-0205.1

Sharman R., Lane T., (2016) Aviation Turbulence, Processes, Detection,Predicition, Springer, 10.1007/978-3-319-23630-8

Smith, R.B. (1989) Mountain Induced Stagnation Points in Hydrostatic Flow. Tellus, 41A, 270-274.http://dx.doi.org/10.1111/j.1600-0870.1989.tb00381.x

Smith, I. H., Williams, P. D., Schiemann, R. (2023). Clear-air turbulence trends over the North Atlantic in high-resolution climate models. *Clim Dyn*. https://doi.org/10.1007/s00382-023-06694-x

Steiner, R., 1966: A review of NASA high-altitude clear air turbulence sampling programs. J. Aircr., 3, 48–52, https://doi.org/10.2514/3.43706

Storer, L. N., Williams, P. D., Joshi, M. M. (2017). Global response of clear-air turbulence to climate change. *Geophys Res Lett*, 44(19), 9976–9984. https://doi.org/10.1002/2017GL074618

Tebaldi C.,Nychka D.,Brown B.,Sharman R.,(2002); Flexible discriminant techniques for forecasting clear-air turbulence.Environmetrics, 859-878, 13(8) https://doi.org/10.1002/env.562

Turner, J. (1999). Development of a mountain wave turbulence prediction scheme for civil aviation. Met Office Forecasting Research Technical Report, p. 265.

Vrancken P et al (2016) Airborne forward-pointing UV Rayleigh lidar for remote clear air turbulence detection: system design and performance. Appl Opt 55(32):9314. https://doi.org/10.1364/AO.55.009314

Watterson IG, Bathols J, Heady C (2014) What influences the skill of climate models over the continents? Bull Am Meteor Soc 95(5):689–700. https://doi.org/10.1175/BAMS-D-12-00136.1

Whiteway, J. A., Pavelin, E. G., Busen, R., Hacker, J., Vosper, S. (2003). Airborne measurements of gravity wave breaking at the tropopause. *Geophysical Research Letters*, 30(20). `https://doi.org/10.1029/2003GL018207`

Williams PD, Joshi MM (2013) Intensification of winter transatlantic aviation turbulence in response to climate change. Nat Clim Chang 3(7):644–648. https://doi.org/10.1038/nclimate1866

Williams JK (2014) Using random forests to diagnose aviation turbulence. Mach Learn 95:51–70. https://doi.org/10.1007/s10994-013-5346-7

Williams PD (2016) Transatlantic flight times and climate change. Environ Res Lett 11(2):024008

Williams, P. D. (2017). Increased light, moderate, and severe clear-air turbulence in response to climate change. *Adv Atmos Sci*, 34(5), 576–586.

`https://doi.org/10.1007/s00376-017-6268-2`

Williams KD et al (2018) The Met Office global coupled model 3.0 and 3.1 (GC3.0 and GC3.1) configurations. J Adv Model Earth Syst 10(2):357–380. https://doi.org/10.1002/2017MS001115

Williams, P. D., Storer, L. N. (2022). Can a climate model successfully diagnose clear-air turbulence and its response to climate change? *Q J R Meteorol Soc*, 148(744), 1424–1438. `https://doi.org/10.1002/qj.4270`

Wolff, J., Sharman, R. D. (2008). Climatology of upper-level turbulence over the contiguous United States. *Journal of Applied Meteorology and Climatology*, 47(8), 2198–2214. `https://doi.org/10.1175/2008JAMC1799.1`

WMO; Worls Meteorological Organization, Classifying clouds,

Zeng, Z., Ziegler, A., Searchinger, T., Yang, L., Chen, A., Ju, K., Piao, S., Li, L., Ciais, P., Chen, D., Liu, J., Azorin-Molina, C., Chappell, A., Medvigy, D., Wood, E. (2019). A reversal in global terrestrial stilling and its implications for wind energy production. *Nature Climate Change*, 9(12), 979–985. `https://doi.org/10.1038/s41558-019-0622-6`

Appendix A

A.1 Clear Air Turbulence indices

Magnitude of vertical wind shear of horizontal wind

$$\frac{\sqrt{du^2 + dv^2}}{dz}$$

Wind speed

$$\sqrt{u^2 + v^2}$$

Magnitude of horizontal temperature gradient

$$\sqrt{\left(\frac{dT}{dx}\right)^2 + \left(\frac{dT}{dy}\right)^2}$$

Magnitude of horizontal divergence

$$\left|\frac{du}{dx}+\frac{dv}{dy}\right|$$

Magnitude of relative vertical vorticity squared

$$\left(\frac{dv}{dx}-\frac{du}{dy}\right)^2$$

Flow deformation

$$\sqrt{\left(\frac{dv}{dx}+\frac{du}{dy}\right)^2+\left(\frac{du}{dx}-\frac{dv}{dy}\right)^2}$$

Flow deformation times wind speed

$$\sqrt{\left(\frac{dv}{dx}+\frac{du}{dy}\right)^2+\left(\frac{du}{dx}-\frac{dv}{dy}\right)^2}\cdot\sqrt{u^2+v^2}$$

Magnitude of potential vorticity

$$-\delta\zeta_a\frac{d\theta}{dp}$$

Colson–Panofsky index

$$\left(\frac{3600}{1852}\right)^2\left((du)^2+(dv)^2\right)\left(\frac{1-Ri}{0.5}\right)$$

Brown index

$$\sqrt{0.3\zeta_a^2 + \left(\frac{dv}{dx} + \frac{du}{dy}\right)^2 + \left(\frac{du}{dx} - \frac{dv}{dy}\right)^2}$$

Brown energy dissipation rate

$$\frac{1}{24}\sqrt{0.3\zeta_a^2 + \left(\frac{dv}{dx} + \frac{du}{dy}\right)^2 + \left(\frac{du}{dx} - \frac{dv}{dy}\right)^2}\,(du^2 + dv^2)$$

Variant 1 Ellrod index

$$\frac{\sqrt{du^2 + dv^2}}{dz}\sqrt{\left(\frac{dv}{dx} + \frac{du}{dy}\right)^2 + \left(\frac{du}{dx} - \frac{dv}{dy}\right)^2}$$

Variant 2 Ellrod index

$$\frac{\sqrt{du^2 + dv^2}}{dz}\left(\sqrt{\left(\frac{dv}{dx} + \frac{du}{dy}\right)^2 + \left(\frac{du}{dx} - \frac{dv}{dy}\right)^2} - \frac{du}{dx} - \frac{dv}{dy}\right)$$

Wind speed times directional shear

$$\sqrt{u^2 + v^2}\left|\frac{\arctan\left(\frac{V_u}{V_l}\right) - \arctan\left(\frac{V_l}{V_u}\right)}{dz}\right|$$

Negative Richardson number

$$-R_s T_m \left(\frac{\frac{T_l}{p^{0.286}} - \frac{T_u}{p^{0.286}}}{\frac{T_m}{p^{0.286}}} \right) \left(\frac{\frac{dp}{p}}{du^2 + dv^2} \right)$$

Flow deformation times vertical temperature gradient

$$\frac{dT}{dz} \sqrt{\left(\frac{dv}{dx} + \frac{du}{dy} \right)^2 + \left(\frac{du}{dx} - \frac{dv}{dy} \right)^2}$$

Frontogenesis function

$$\frac{du}{d\theta} \left(\frac{dv}{d\theta} \frac{du}{dx} + \frac{dv}{d\theta} \frac{du}{dy} \right) + \frac{dv}{d\theta} \left(\frac{du}{d\theta} \frac{dv}{dx} + \frac{du}{d\theta} \frac{dv}{dy} \right)$$

Magnitude of residual non-linear balance equation

$$2 \left| \frac{du}{dx} \frac{dv}{dy} - \frac{du}{dy} \frac{dv}{dx} \right|$$

Magnitude of relative vorticity advection

$$\left| u \frac{dQ}{dx} + v \frac{dQ}{dy} \right|$$

Negative absolute vorticity advection

$$-u\frac{dQ}{dx} - v\left(\beta + \frac{dQ}{dy}\right)$$

Version 1 of North Carolina State University index

$$\frac{u\frac{du}{dx} + v\frac{dv}{dy}}{Ri\sqrt{\left(\frac{dQ}{dx}\right)^2 + \left(\frac{dQ}{dy}\right)^2}}$$

A.2 Data availability statement

To access the Coupled Model Inter-comparison Project phase 6 (CMIP6) global climate model data, via the same routes as the authors, please contact PRIAMVERA partners from https://www.primavera-h2020.eu/. The PRIMAVERA project is led by the Met Office and the University of Reading.

A.3 Funding

The results and findings here are part of the IS-ENES3 project that has received funding from the European Union's Horizon 2020 research and innovation programme under grant agreement No. 824084 (https://www.primavera-h2020.eu/). The author declare that other no funds, grants, or other support were received during the preparation of this thesis.